# A Higher-Order Flamelet Model for Turbulent Combustion Simulations

by

Wai Lee Chan

A dissertation submitted in partial fulfillment
of the requirements for the degree of
Doctor of Philosophy
(Aerospace Engineering)
in the University of Michigan
2016

Doctoral Committee:

       Assistant Professor Matthias Ihme, Stanford University, Co-Chair
       Professor James F. Driscoll, Co-Chair
       Associate Professor Venkat Raman
       Professor Volker Sick

2016

To Mom, Dad, and Meng, who love me so unconditionally.

# ACKNOWLEDGMENTS

It still feels surreal that I am actually writing this passage, the part of my thesis that I have intentionally kept to the last. Though not harsh, life has not been a bed of roses either, so I would like to think that I have been through some tough times. But nothing so far compares to completing this work, which has really demanded all my possible efforts. Fortunately, this is where my interest lies, so the process was more fun than painful. Still, I could not have made it without the support from all those who care and love me.

The very first person whom I will like to acknowledge is my advisor, Professor Matthias Ihme, whose guidance and support have made this work possible. His knowledge and ideas in turbulent combustion have motivated my passion in the field of combustion research and inspired my career aspiration in academia. I will always be thankful for Professor Ihme's confidence in me when he accepted me as his doctoral student five years ago, a time when I knew nothing about combustion. I regret those moments that I have disappointed him, but hope that overall I have done him proud. I will strive to keep doing so.

I am also indebted to Professor James Driscoll, Professor Volker Sick, and Professor Venkat Raman for taking their precious time to serve as my dissertation committee members; much of the presented work has benefitted from their constructive criticisms and insights. Their kind words have been most encouraging, and their opinions have shaped my expectations and values in moving on to be an independent researcher.

Next, I will like to express my gratitude to my collaborators, Dr. Jacqueline Chen, Dr. Hemanth Kolla, Professor Christian Hasse, and Arne Scholtissek, whom I had the privilege to work with during my research. It was truly my honor to have the opportunity to work with these experts, and I thank them for sharing with me their knowledge and reciprocating the mutual trust during our collaborations.

As for my friends, I was plain lucky to have them in my life. The everlasting DHS gang, Chei Ren, Chong Yang & YiiYin, Fang Hao, Robin, and Yee Jie, has been and always will be the closest to what I can have as siblings. They have shaped my personality and reminded me that there will always be a fallback for me. My endearing little 2J group, Daphne, Wilfred, and Yi Qing, not so little now with the addition of Aloysius and Jon, has

showered me with concerns that gave me warmth when time got difficult or when snow got heavy. My first academic mentor, Mrs Loo Lai Leng, trusted me enough to recommend me to study overseas. My graduation should prove that her trust was well-placed.

I used to think that meeting new friends in college is a myth, but was glad to be proven wrong by the FXB 2211 band of brothers, Chang-kwon, Kentaro & Sayaka & Alisa, Yee Chee, and Yuntao, who taught me so much about both my research and life. I am especially touched by Ken, Yee Chee, and Yuntao for making the effort and spending the money to fly or drive over for my defense from New York, Wiscosin, and Florida. Not to forget an even more recent friend, Matthew Bjurman, owner of the Milan Coffee Works, who went all the way beyond his duty to supply my defense presentation with excellent coffee. The best way that I could think of to express my thanks to Matt is this product placement, although I am certain that his business will prosper because the customers will always be drawn in by his hospitality, besides the excellent coffee of course.

Brad & Sara belong to the 2211 group too, but they are two friends that are worthy of a special mentioning. If the rest of the gang overturned my naive disbelief in making new friends, Brad is the one friend who has redefined me. I was recently told that my affection in (good!) coffee has made me a different man, one who finally has a definite preference an everyday matter. Brad should know that this is because of him. Brad also played a vital role in helping me fulfill a critical part of this work, so I will share the credit for this work with him. Sara has grown from Brad's spouse to a dear friend close to my heart, always showing genuine care and cooking up scrumptious meals during the festivals. Here alone, Brad & Sara were my family, and I have nothing but thanks for them.

My fifth aunt, Kwong Wa, sixth aunt & uncle, Kwong Man and Wa Shing, cousins, Chi Ho and Chi Man, have played critical parts in lifting the burden of my family issue off my shoulders. I will never be able to express to them how important that was for me to be able to complete my study. Also, my grandfather, Qin Yuan Jun, an impressively healthy centenarian most definitely deserves a place in this acknowledgment. I thank him for being kicking alive and keeping the family together.

My beloved mother, Kwong Ling, and my dear father, Kwun Ming, have given me so much love and patience that my achievements now are just like "installment payments". I can only repay them with my love and respect for as long as they live.

Last, but not least, my Love, Meng, whom should now be used to waiting for me. Meng has seen through my goods and bads, but still chose to stick around; I believe that only true love will make one do so. Now that this big chapter of my life is coming to its end, I cannot wait to open the new one with Meng, and everybody who is important in her life.

# TABLE OF CONTENTS

# LIST OF FIGURES

# LIST OF TABLES

# LIST OF ABBREVIATIONS

**AIDW**    Adaptive Inverse-Distance Weighting

**BTU**    British Thermal Unit

**CFD**    Computational Fluid Dynamics

**CMC**    Conditional-Moment Closure

**CSE**    Conditional-Source term Estimation

**DNS**    Direct Numerical Simulation

**DQMOM**  Direct Quadrature Method of Moments

**EPFM**    Eulerian Particle Flamelet Model

**FPV**    Flamelet/Progress-Variable

**FDF**    Filter-Density Function

**HIT**    Homogeneous Isotropic Turbulence

**HOFM**    Higher-Order Flamelet Model

**HOT**    Higher-Order Terms

**HPC**    High-Performance Computing

**IDW**    Inverse-Distance Weighting

**JICF**    Jet-In-CrossFlow

**LEM**    Linear Edddy Model

**LES**    Large-Eddy Simulation

**MPG**    Miles Per Gallon

**ODT**    One-Dimensional Turbulence

**PDF**    Probability-Density Function

**RANS**     Reynolds-Averaged Navier-Stokes

**RHS**      Right-Hand-Side

**RIF**      Representative Interactive Flamelets

**SGS**      SubGrid-Scale

**SLFM**     Steady Laminar Flamelet Model

**TCDF**     Turbulent Counterflow Diffusion Flame

# LIST OF SYMBOLS

**Latin Symbols**

| | |
|---|---|
| $a$ | Strain rate, Beta-distribution parameter (fuel-lean) |
| $A$ | Generic matrix of a linear system |
| $b$ | Generic RHS of a linear system, Beta-distribution parameter (fuel-rich) |
| $c_p$ | Specific heat capacity ($p = $ const.) for species with $(\ )_\alpha$; for mixture otherwise |
| $C$ | Progress-variable |
| $\mathcal{C}$ | Generic constant |
| $D$ | Diffusivity |
| $e$ | Total specific energy |
| $E$ | Turbulent energy spectrum |
| $f$ | Body force |
| $\mathcal{F}$ | Lower-order dimension manifold |
| $h$ | Specific enthalpy for species with $(\ )_\alpha$; total value otherwise |
| $I$ | Identity matrix/tensor $= \delta_{ij}$ |
| $k$ | Reaction-rate coefficient, Specific kinetic energy $= 0.5\widetilde{u_k u_k}$ |
| $l$ | Generic length-scale |
| $\mathcal{L}$ | Germano identity matrix (RHS) |
| $\mathcal{M}$ | Germano identity matrix (System) |
| $n$ | Mole number of element-$\beta$ of species-$\alpha$ with $(\ )_{\alpha\beta}$, Normalized vector |
| $N$ | Generic maximum count of a dataset |
| $P(\ )$ | PDF (Unweighted) |

| | |
|---|---|
| $\widetilde{P}(\ ;\psi)$ | FDF (Density-weighted) given condition $\psi$; unconditioned otherwise |
| $\overline{P}(\ ;\psi)$ | FDF (Unweighted) given condition $\psi$; unconditioned otherwise |
| $q$ | Heat flux, Heat source |
| $r$ | Nearest-neighbor statistic |
| $R$ | Specific gas constant; universal value $= 8.314 \mathrm{J/mol} \cdot \mathrm{K}$ with $\widetilde{(\ )}$ |
| $s$ | Strain-rate tensor |
| $\mathcal{S}$ | SGS turbulent flux at test-filter level, $\widehat{\Delta}$ |
| $t$ | Physical time |
| $u$ | Velocity |
| $v$ | Diffusion velocity |
| $V$ | Volume |
| $w$ | Generic interpolation weight |
| $W$ | Molecular weight for species with $(\ )_\alpha$; for mixture otherwise |
| $x$ | Generic variable (solution) of a linear system, Position |
| $\boldsymbol{x}$ | Position vector $= [x_1,\ x_2,\ x_3]^{\mathrm{T}}$ |
| $X$ | Species mole-fraction |
| $Y$ | Species mass-fraction |
| $\boldsymbol{z}$ | Local mixture-fraction coordinate $= [Z,\ Z_2,\ Z_3]^{\mathrm{T}}$ |
| $Z$ | Mixture-fraction |
| $\mathcal{Z}$ | Unnormalized coupling function for $Z$ |

## Greek Symbols

| | |
|---|---|
| $\beta$ | Beta-distribution |
| $\chi_Z$ | Scalar-dissipation rate of $Z$ |
| $\delta$ | Dirac delta function, Fine-grained PDF |
| $\Delta$ | Generic coordinate spacing, Spatial-filter width |
| $\epsilon$ | Small parameter |

| | |
|---|---|
| $\varepsilon$ | Differential-diffusion parameter with $(\ )_i$, Reaction-zone thickness parameter otherwise |
| $\eta$ | Kolmogorov length-scale, $Z_{\mathrm{st}}$-isosurface streamwise parameter |
| $\gamma$ | Weighting factor for $\mathcal{Z}$, Beta-distribution parameter (variance) |
| $\Gamma$ | Gamma function |
| $\kappa$ | Heat conductivity, Local curvature |
| $\lambda$ | Eigenvalue of a tensor, Tikhonov's regularization parameter |
| $\Lambda$ | Reaction progress parameter |
| $\dot{\omega}$ | Reaction rate |
| $\Omega$ | Rotation-rate tensor |
| $\mu$ | Dynamic viscosity |
| $\nu$ | Flame curvature parameter, Kinematic viscosity |
| $\phi$ | Generic variable |
| $\psi$ | Flamelet regime-diagram parameter, Generic variable |
| $\rho$ | Density, Number density with $(\ )_N$ |
| $\sigma$ | Viscous stress tensor |
| $\tau$ | Flamelet time |
| $\xi$ | Azimuthal location of JICF, Spatial-interpolation exponent for AIDW |
| $\zeta$ | Flame-length, Independent variable of $Z$ |

## Mathematical Operators

| | |
|---|---|
| $\nabla$ | Gradient |
| $\overline{(\ )}$ | Filtered quantity (Spatial) |
| $\widetilde{(\ )}$ | Filtered quantity (Favre) |
| $\widehat{(\ )}$ | Filtered quantity (Test) |
| $\|(\ )\|$ | L2-norm of vector |
| $(\ )|\zeta$ | Mixture-fraction conditioned quantity |
| $\langle(\ )\rangle$ | Reynolds averaged quantity (Spatial) |

| | |
|---|---|
| $\mathcal{G}$ | Spatial-filter function |
| $\mathrm{Tr}\,[\,]$ | Trace of a matrix; sum over diagonal components |
| $(\;)^T$ | Transpose of a matrix/vector |

**Non-Dimensional Terms**

| | |
|---|---|
| Da | Damköhler number |
| Ka | Karlowitz number |
| Le | Lewis number |
| Ma | Mach number |
| Re | Reynolds number |

**Subscripts**

| | |
|---|---|
| $b$ | Index of coordinate bin; no summation over indices |
| $B$ | Bilger-type mixture-fraction, Bulk quantity |
| $C$ | Compressive strain, Correction quantity |
| $E$ | Extensive strain |
| $f$ | Heat of formation, Index of flamelet path; no summation over indices |
| **Fl** | Flame quantity |
| $F, O$ | Fuel/oxidizer side of a two-stream, diffusion flame configuration |
| $g$ | Global quantity |
| $G$ | Gibson's velocity |
| $i, j, k$ | Index of Cartesian space; summation applies |
| $K$ | Kolmogorov scale quantity |
| $m, n$ | Index of matrix/vector; summation applies |
| $\min, \max$ | Minimum/maximum of a variable |
| $p$ | Index of spatial point; no summation over indices |
| $r$ | Reaction-zone related |
| $R$ | Radiation |
| $s$ | Sensible quantity |

| | |
|---|---|
| st | Stoichiometric quantity |
| $S$ | Smagorinsky model quantity |
| $t$ | Turbulence model quantity |
| $th$ | Thermal quantity |
| $Z$ | In direction of $\nabla Z$ |
| $\alpha$ | Index of species; no summation over indices |
| $\beta$ | Index of species element; no summation over indices |
| $\Lambda$ | Turbulence quantity relative to integral scale |
| $\perp$ | In direction orthogonal to $\nabla Z$ |

## Superscripts

| | |
|---|---|
| Chem | Characteristic of chemical reaction |
| Flow | Characteristic of flow |
| Guess | Estimate of solution of a linear system |
| Ign | Flame-ignition point of S-shaped curve |
| Qch | Flame-quenching point of S-shaped curve |
| Ref | Reference quantity |
| Res | LES resolved quantity |
| SGS | LES subgrid-scale quantity |
| $\perp$ | Mixture-fraction orthogonal direction |
| $'$ | Subgrid-scale variance (Spatial) |
| $''$ | Subgrid-scale variance (Favre) |
| $\pm$ | Upper/Lower bound of an interval |

## Accents

| | |
|---|---|
| $\widehat{(\ )}$ | Mole specific quantity, Normalized operand |
| $\dot{(\ )}$ | Rate of change of operand |

# ABSTRACT

**A Higher-Order Flamelet Model for Turbulent Combustion Simulations**

**by**

**Wai Lee Chan**

**Co-Chairs: Matthias Ihme, James F. Driscoll**

Current projection of energy consumption trends has shown that combustion of fossil fuel will continue to play an important role in industrial thermal processes, power generation, and transportation for a substantial period. In order for these sectors to sustain under the finite fossil fuel reserves, improvements in existing devices and development of novel concepts that emphasize on energy efficiency are necessary. Numerical simulations can be used to address this need, in particular by complementing experiments with extensive and quick parametric studies. However, this is only viable if numerical predictions of the combustion processes are accurate, which requires adequate modeling of the multi-physics phenomena in turbulent reacting flows.

   In this work, the flamelet-type combustion model, one of the most widely used approaches for turbulent reacting flow simulations, is thoroughly analyzed in terms of the validity of its underlying assumptions and limitations in its description of different combustion regimes. Diagnostic tools that account for the flamelet formulation are developed and applied to two different direct numerical simulation (DNS) results. These analyses show that the omission of the higher-order and unsteady flamelet effects by most conventional

flamelet models is not valid in realistic configurations that are characterized by complex vortical structures, flame extinction and reignition, and turbulence-chemistry interactions.

Following these findings, a higher-order flamelet model that describes the conventionally omitted flamelet effects is developed for large-eddy simulations (LES) applications. This model is based on the physical interpretation of flamelets as quasi one-dimensional structures in the turbulent flow, and the consideration of the effects that the spatial-filtering in LES methodology has on these structures. The model is applied in LES of a turbulent counterflow diffusion flame configuration, demonstrating improved agreement with the reference DNS solutions of the same case than the steady flamelet/progress variable (FPV) and laminar approximation models.

# CHAPTER 1

# Introduction

## 1.1   Motivation

Examining the forecast of the energy outlooks by the U.S. Energy Information Adminstration, one observation that can consistently be made is that the primary energy consumption level has mostly been climbing since the year 1980. The latest projection [1], as shown in Fig. 1.1, indicates that the total consumption level is expected to grow from 97 quadrillion British thermal units (BTU) in 2013 to 105 quadrillion BTU in 2040, almost an increase of 9% over that timeframe. Among this increase, the main contributors appear to be the consumption of natural gas and renewable energy (including biomass, geothermal, solar, and wind energy sources), while coal and petroleum plateau at a collective amount of approximately 50% of the total consumption. Therefore, the importance of combustion in power generation is apparent, and will possibly be unchallenged for a substantial period.

The combustion of fuel sources is, however, not without adverse effects. Specifically, pollutants, such as unburned hydrocarbons, carbon mono- and dioxides, nitrogen oxides, and soot, will be released into the atmosphere during the combustion processes and have detrimental effects on the environment. For instance, the emission of nitrogen oxides has led to the issue of acid rain, whereas the formation of carbon dioxide increases the presence of greenhouse gases, which are widely considered as the causes of global warming. The latter problem is prominently addressed during the recent 21st Conference of the Parties to the United Nations Framework Convention on Climate Change [2] , which attributed approximately 70% of global greenhouse gas emissions to the sector of transportation, power generation, and industrial thermal processes.

Considering the limited fossil fuel reserves, as well as the need to preserve the environment, the critical step so that our ever-growing need of energy can be fulfilled is then to develop combustion devices that are characterized by high combustion efficiency, low pollutant emissions, and flexibility to fuel sources. This dire need to enhance the perfor-
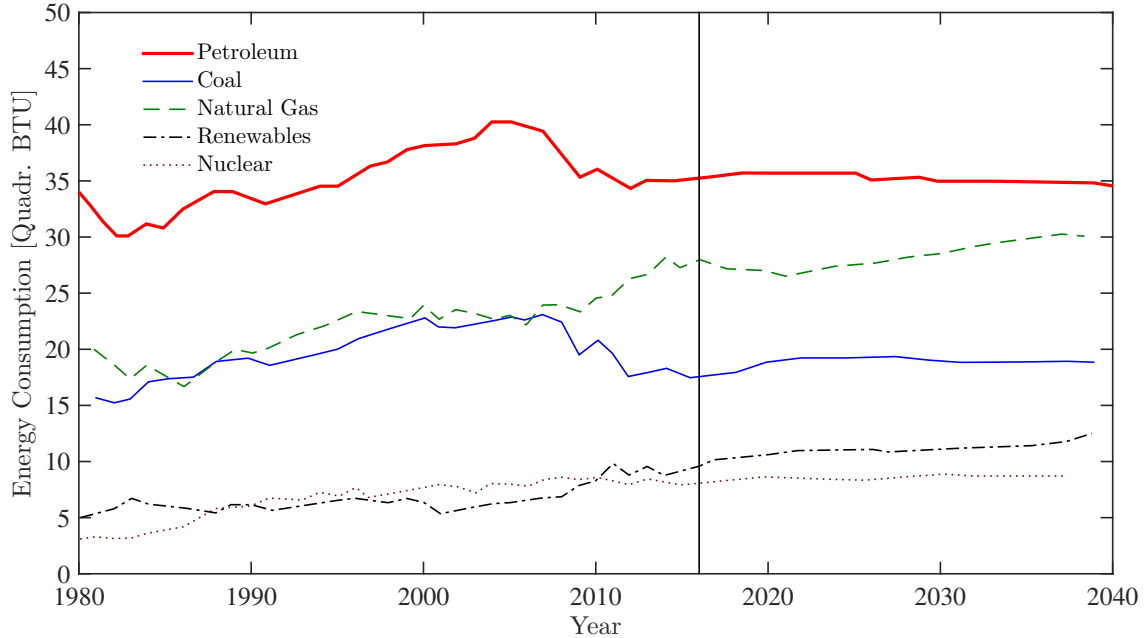
Figure 1.1: U.S. energy consumption in Quadrillion BTU by primary fuel from year 1980 to 2040. The vertical line denotes the current year and separates historical records from projections [1].

mance of combustion devices has particularly been recognized by the transportation sector, wherein many successful cases can be found. For example, the fuel economy of light-duty vehicles, which contributes to approximately 60% of energy consumption for transportation in 2013, is currently at a level higher than 30 miles per gallon (MPG) and improving so favorably that the energy consumption is projected to deviate from the historical trend and falls through 2030 [1]. In the aviation sector, there have been innovative designs, such as the low-emission combustor and geared turbofan engine, which reduce fuel consumption, noise, and pollutant emission up to 10%.

To keep up with this improvement trend, the design phase of combustion devices, especially for novel concepts, requires short turnaround time and reasonable development cost. In this regard, the incorporation of numerical methods will be particularly suitable, allowing for quick and extensive parametric studies that provide valuable insights to complement physical experiments, as in the case of Reynolds-averaged Navier-Stokes (RANS) methodology. Furthermore, the vast interest and rapid growth in high-performance computers guarantee that the rate of numerical calculations be constantly increasing. If the time factor can be relaxed, high-fidelity simulations using the direct numerical simulation (DNS) technique can offer information at such fine spatial-scales that they are inaccessible to any state-of-the-art emperical measurements [3].

However, the utilization of numerical techniques can be challenging due to computational and physical complications. For the initial, the key challenge comes from the need for effective data-management schemes during the calculation and post-processing stages. This difficulty is especially relevant for high-fidelity simulations, wherein all spatial and temporal scales that are relevant to the flow are to be resolved. As a result, the data can have overwhelmingly large sizes (currently at the order of tens of $\mathcal{O}(10^{12})$ bytes, or terabytes (Tb), and moving towards the order of $\mathcal{O}(10^{15})$ bytes for DNS) and be processed only by $\mathcal{O}(10^4)$ of processors that work in parallel for weeks [3].

Clearly, these outstanding figures are not compatible with the practical combustion device design procedure, which places a large emphasis on the turnaround time. Therefore, DNS to date are generally performed for the sake of academic interests and used to garner insights into the interactions of chemistry and turbulence that occur at the smallest continuum scales of flame and turbulence. In turn, these important findings will be used to develop and validate predictive closure models required by more time-effective methods to accurately represent the reacting flows without having to resolve all relevant scales. Two established techniques for this purpose are RANS, where the solutions are averaged over time and usually applicable to statistically-steady configurations, and large-eddy simulations (LES), where the solutions are filtered over space.

The reason for RANS and LES to require closure models is due to the physical complications that affect the numerical simulations of combustion devices. In essence, the dynamic conditions within a combustor, including flame quenching and reignition, and flow separation and swirl, have to be accurately captured in the simulations for the numerical results to be representative, of the actual device. However, combustion-related phenomena, such as chemical reactions, species diffusion, and turbulence-chemistry interactions, pertain to the smallest continuum scale, hence constituting a closure problem in methods like RANS and LES where the resolution is inadequate for the finest scales of combustion.

The closure problem can be illustrated by considering the scalar-dissipation rate:

$$\chi_Z = 2D_Z \frac{\partial Z}{\partial x_i} \frac{\partial Z}{\partial x_i} \, , \tag{1.1}$$

where $D_Z$ is the molecular diffusivity of the mixture-fraction, $Z$, a quantity that indicates the composition mixedness within a flow. Bilger [4] has pointed out that the heat-release in non-premixed combustion is almost entirely determined by the mixing rate, which is intrinsically related to the scalar-dissipation rate. A flame can be locally quenched and extinguished when the scalar-dissipation rate fluctuates beyond a critical value that is determined by the instantaneous composition and environment, even if the scalar-dissipation

rate is on average lower than the mean critical value [5]. Consequently, the RANS approach is, by design, unsuitable to capture such transient behaviors. On the other hand, an LES that is performed without an adequate model of the scalar-dissipation rate will not fare well either, because the mixing dynamics of the flow will then not be accurately represented since the scalar-dissipation rate has dissipative effect over the mixture-fraction that is analogous to the turbulence dissipation term on the turbulence kinetic energy [6].

In the present work, a flamelet-based combustion model is developed for the prediction of turbulent combustion within non-premixed configurations. This model is derived from the fundamental concept of the flamelet formulation, in which a turbulent diffusion flame is treated as an ensemble of laminar structures, or so-called flamelets, that are embedded within the turbulent flow [7]. On these flamelets, all thermochemical species can be described by a reduced set of scalars, such as mixture-fraction, scalar-dissipation rate, or reaction progress variable. Therefore, a flamelet model is, in practice, similar to a lower-dimensional manifold representation of the chemistry [8]. In order to provide closure to the source terms of filtered thermochemical quantities in LES, the model considers similar approaches of conventional flamelet-type models [9,10], including the tabulation technique and presumed scalar-distribution profile, but implemented in a dynamic manner. In doing so, the transient and higher-order flamelet effects can be retained, extending the model's applicable range to beyond classic flamelet regimes [11].

The objective of this work is to develop a flamelet model that relaxes the asymptotic thin reaction-zone assumption of the current flamelet-type models, so that the commonly neglected secondary flamelet effects, such as unsteadiness and flamelet-orthogonal diffusion, can be accommodated. As a result, the model will account for the interactions between flamelets, which have been found to be significant in the presence of flame extinguishing and reignition [5, 12]. The model does so by extracting the thermochemical information along multiple coordinate-invariant flamelets [13], which are given by the gradient trajectories of the mixture-fraction field. Therefore, these flamelet-conditional information will retain their multi-dimensional advective and diffusive fluxes, which are equivalent to the terms in a flamelet equation upon a coordinate-transformation of the corresponding transport equation onto the flamelet space. This approach thus constitutes a higher-order flamelet model, which does not rely on any explicit modeling of the higher-order effects, for the prediction of turbulent combustion.

An important part of the model development pertains to the validation of the individual model components, which ideally should be performed against highly accurate experimental measurements of well-characterized configurations. However, even with today's state-of-the-art diagnostics, accurate measurements within a combustion device can still be

difficult to perform due to hostile environment, multi-dimensionality and unsteadiness of flow, and limited access for non-intrusive measurement techniques. For these reasons, the various model components are mostly assessed using results of high-fidelity DNS, which have been carefully performed and extensively studied over recent years.

## 1.2 Large-Eddy Simulation

The LES methodology is a simulation approach that numerically resolves only the energy-containing and geometry-dependent scales of turbulent motions, but models the effects of the unresolved scales on the large scales. Such an approach is based on the separation of scales due to turbulent energy cascade theory, and can be interpreted as the application of a low-pass spatial filter (i.e. small wavelength cutoff) over the numerical simulation [14]. In general, the residual scales will extract energy from the large scale turbulence and dissipate the turbulent energy into heat via viscous effects.

Leveraging the rapid improvement in high-performance computing, the LES has been gaining traction as the complementary numerical technique to physical testings. The main reason for this growth in the popularity of LES is its unique offering of a balance between fidelity and practicality, which are the lacking aspects of RANS and DNS, respectively. By design, RANS omits all transient phenomena, thus limiting its relevance to combustion devices, in which a steady-state may not be present at off-design conditions. On the other hand, DNS resolves all combustion scales (spatial and temporal), but at the expense of prohibitive costs that restrict the application of DNS to date to mostly laboratory-scale flames [3, 15]. Therefore, the accuracy and efficiency that LES offers with its consideration of temporal variations and modeling, instead of resolving, of fine spatial scales, respectively, are especially attractive. Of course, it is worthnoting that the time-dependent solutions of LES can come with computational costs that are comparable to DNS. Hence, RANS calculations are still frequently used in studies that emphasize on the turnaround time instead of result accuracy, such as the case of parametric studies where only qualitative, steady trends are required.

In turbulent non-premixed combustion, the flame dynamics is largely controlled by the molecular mixing of fuel and oxidizer, which is only facilitated by molecular diffusion. Therefore, the chemical reactions will occur at the small turbulent scales, so the concept of LES is fundamentally unsuitable for combustion applications, posing a closure problem that is analogous to that of RANS due to its time-averaging procedure. However, with adequate modeling, the interactions between the small and large turbulent scales can be reasonably captured in an LES, resulting in the general observation of an improved accu-

racy over RANS in terms of the prediction of turbulent reactive flows. This improvement is attributed to the ability of LES to predict the unsteady scalar mixing and dissipation processes, particularly in complex flow geometries [16].

Based on the likelihood that LES will become a routine high-fidelity numerical tool, the current work focuses on the applications of the combustion model in the context of LES. The essential objective is to develop a flamelet-type closure model for the source term of the filtered thermochemical quantities that considers all flamelet effects, including unsteadiness and flamelet-to-flamelet interactions. The development is theorized, assessed, and applied over both *a-priori* and *a-posteriori* cases that are carefully selected based on their physical complexities and the corresponding compatibility with the task objectives.

## 1.3   Turbulent Combustion Models

Different classes of combustion models have been proposed for the prediction of non-premixed turbulent combustion processes. The general categories of these models are conditional moment closure (CMC) [17] method, flamelet models [7], one-dimensional turbulence (ODT) [18] model, and transported probability-density function (PDF) [19] method. Comprehensive reviews of turbulent combustion models can be found in Refs. [9,20], while an overview on the model applications in LES is given by Pitsch [16].

The CMC method is originally proposed for application in RANS, where all reactive scalars are solved by their corresponding mixture-fraction conditioned transport equations [17, 21, 22]. Extension of the CMC model for LES was formulated and applied by Kim & Pitsch [23, 24]. In this model, the mixture-fraction, which is solved by a conserved scalar transport equation, is considered as an independent variable in addition to the spatial and temporal coordinates. The CMC approach is suitable for conditions of slow to moderate reaction rates and moderate turbulent intensities, which can be quantified by Damköhler number of $\mathrm{Da} < \mathcal{O}(10^4)$ and Reynolds number of $\mathrm{Re} < \mathcal{O}(10^5)$, respectively.

Using the CMC hypothesis, Bushe & Steiner [25] developed the conditional-source term estimation technique, in which the mixture-fraction conditioned composition vector and temperature are obtained by deconvolving the LES filtered scalar with a presumed shape of the mixture-fraction distribution within a LES filter-cell. The model capability has been demonstrated in LES of two Delft-jet-in-hot-coflow configurations [26] using a detailed methane/air chemistry mechanism [27].

Variants of the flamelet model for LES applications have been developed over recent years, with the steady laminar flamelet model being investigated in *a-priori* studies [28, 29] and simulations of jet flames and bluff-body stabilized flames [30–32]. Pierce

& Moin [10, 33] introduced a flamelet/progress-variable (FPV) that is based on the steady laminar flamelet concept, but uses the mixture-fraction and a reaction progress variable, instead of the scalar-dissipation rate, to parameterize all thermochemical quantities. In order to capture transient combustion effects, an unsteady version of the laminar flamelet model was investigated and successfully applied in LES of a piloted methane/air diffusion flame [34]. An unsteady FPV model was developed and applied [35, 36] in LES of the Cabra flame [37] for prediction of the autoignition phenomenon. In his overview of nonpremixed turbulent combustion [11], Williams mentioned that the flamelet model is applicable in a flamelet regime, covering a comparable range of low to high Damköhler and Reynolds numbers ($\mathcal{O}(10^0)$–$\mathcal{O}(10^8)$), and even in a so-called broken flamelet regime, wherein the assumption of fast chemistry is invalid, with the recent developments.

ODT, similar to the linear eddy model (LEM) [38, 39], is a combustion model that does not rely on the turbulence scale-separation. Instead, the turbulence evolves on individual ODT elements that constitute multiple one-dimensional domains with sufficient resolution to describe all relevant scales of the reacting flow. The ODT is coupled with LES by treating reaction-diffusion, resolved advection, and SGS transport in sub-LES time steps and returning these information to the LES, which in turn will advance the solutions of the mass and momentum transport equations that will be interpolated on the ODT elements [40]. Cao & Echekki [41] have applied the ODT model in LES of non-homogeneous ignition phenomenon in isotropic turbulence with a pseudo single-step, irreversible reaction.

Due to its high computational costs and numerical instabilities from the implementation of the Monte-Carlo method [42], the transported PDF method was initially applied in reacting RANS [19, 43] and LES with simple geometries [44]. More practical LES applications were demonstrated only recently in the context of jet flame configurations by Raman *et al.* [45] and Raman & Pitsch [46]. The model is distinctive in its formulation, in which the chemical source term appears in closed form. However, the model is not free from the closure problem because the molecular mixing requires multi-point information and thus needs to be modeled. Williams pointed out that the transported PDF model is ideal for the combination of low Damköhler number ($\mathcal{O}(10^0)$) and high Reynolds number [11] flows.

## 1.4   Accomplishments

The important contributions of this work is summarized in the following list:

- Development of diagnostic tools that allow for formal assessment of the flamelet formulation, in which the consideration of unsteady and higher-order flamelet effects have been identified as potential areas for the improvement of current flamelet-type combustion models. These tools were applied in the *a-priori* analyses of DNS of a reacting jet-in-crossflow and turbulent lifted jet flame configurations.

- Development of a flamelet regime diagram that accounts for the numerical fidelity, allowing for direct assessment of the applicability of the flamelet formulation in different reacting flow simulations.

- Development of a constrained LES method that utilizes solutions from a simultaneous DNS for the turbulence closure, thus isolating the combustion model as the only source of simulation errors. This method was demonstrated to be robust and useful in validation studies that compare the performance of different combustion models, and can be extended for comparison of turbulence SGS models.

- Development of a higher-order flamelet model that accounts for the unsteady and higher-order flamelet effects by the dynamic extraction of flamelet information from the transported LES fields and reaction prediction with the combined theories of flamelet, PDF, and CMC; demonstration of the model applicability in both constrained LES and *a-posteriori* LES of a turbulent counterflow diffusion flame.

# CHAPTER 2

# Mathematical Model

In this chapter, the detailed set of governing equations that are relevant to the spatial and temporal evolution of reacting flows are presented. Under specific conditions, these equations can be simplified to a working set of equations, which will be employed in subsequent chapters of this work.

Since the purpose of a combustion model is largely derived from the application of the LES methodology, Sec. 2.3 will be dedicated to the LES filtering concept and the resulting filtered flow equations. Thereafter, the modeling approach that provides closure for the LES residual stress contributions will be provided.

## 2.1 Governing Equations

In conservative form, the equations that govern the transport of mass, momentum, total specific energy, and species mass-fraction can be written as:

$$\frac{\partial \rho}{\partial t} + \frac{\partial \rho u_i}{\partial x_i} = 0 \, , \tag{2.1a}$$

$$\frac{\partial \rho u_i}{\partial t} + \frac{\partial \rho u_i u_j}{\partial x_j} = -\frac{\partial p}{\partial x_i} + \frac{\partial \sigma_{ij}}{\partial x_j} + \rho \sum_\alpha Y_\alpha f_{\alpha,i} \, , \tag{2.1b}$$

$$\frac{\partial \rho e}{\partial t} + \frac{\partial \rho e u_i}{\partial x_i} = -\frac{\partial p u_i}{\partial x_i} + \frac{\partial \sigma_{ij} u_i}{\partial x_j} + \rho \sum_\alpha Y_\alpha f_{\alpha,i} \left( u_i + v_{\alpha,i} \right) - \frac{\partial q_i}{\partial x_i} - \dot{q}_R \, , \tag{2.1c}$$

$$\frac{\partial \rho Y_\alpha}{\partial t} + \frac{\partial \rho Y_\alpha u_i}{\partial x_i} = -\frac{\partial \rho Y_\alpha v_{\alpha,i}}{\partial x_i} + \rho \dot{\omega}_\alpha \, . \tag{2.1d}$$

The viscous stress tensor, $\sigma_{ij}$, in Eq. (2.1b) can be expanded to:

$$\sigma_{ij} = 2\mu s_{ij} + \mu_B \frac{\partial u_k}{\partial x_k} I_{ij} \, , \quad s_{ij} = \frac{1}{2} \left( \frac{\partial u_i}{\partial x_j} + \frac{\partial u_j}{\partial x_i} \right) \tag{2.2}$$

where $s_{ij}$ is the strain-rate tensor and $\mu_B$ is the bulk viscosity.

The heat flux vector, $q_i$, in Eq. (2.1c) can be written as:

$$q_i = -\kappa \frac{\partial T}{\partial x_i} + \rho \sum_\alpha Y_\alpha h_\alpha v_{\alpha,i} + \widehat{R} T \sum_\alpha \sum_{\alpha'} \frac{X_{\alpha'} D_{T,\alpha}}{W_\alpha D_{\alpha\alpha'}} \left( v_{\alpha,i} - v_{\alpha',i} \right) , \qquad (2.3)$$

where the terms on the RHS describe, respectively, the heat conduction by Fourier's law, heat flux due to diffusion of species with different enthalpies, and Dufour effect (i.e. heat flux due to density gradient).

The diffusion velocities, $v_{\alpha,i}$, in Eq. (2.1d) may be obtained from an implicit expression that is derived from kinetic theory [6]:

$$\frac{\partial X_\alpha}{\partial x_i} = -\sum_{\alpha'} \frac{X_\alpha X_{\alpha'}}{D_{\alpha\alpha'}} \left( v_{\alpha,i} - v_{\alpha',i} \right) + \left( Y_\alpha - X_\alpha \right) \frac{1}{p} \frac{\partial p}{\partial x_i}$$

$$+ \frac{\rho}{p} \sum_{\alpha'} Y_\alpha Y_{\alpha'} \left( f_{\alpha,i} - f_{\alpha',i} \right) - \sum_{\alpha'} \frac{X_\alpha X_{\alpha'}}{\rho D_{\alpha\alpha'}} \left( \frac{D_{T,\alpha}}{Y_\alpha} - \frac{D_{T,\alpha'}}{Y_{\alpha'}} \right) \frac{1}{T} \frac{\partial T}{\partial x_i} , \qquad (2.4)$$

where $D_{\alpha\alpha'}$ denotes the binary mass diffusion coefficient matrix of species-$\alpha$ relative to the other relevant species-$\alpha'$. Respectively, the terms on the right-hand-side (RHS) of Eq. (2.4) correspond to the Stefan-Maxwell diffusion, diffusion due to pressure gradient, body-force driven diffusion, and Soret effect (i.e. diffusion due to temperature gradient). Due to its high computational cost, in particular for a large species system, Eq. (2.4) is typically replaced by simplified expressions such as Fick's law:

$$v_{\alpha,i} = -\frac{D_\alpha}{X_\alpha} \frac{\partial X_\alpha}{\partial x_i} = -D_\alpha \left( \frac{\partial Y_\alpha}{\partial x_i} + \frac{Y_\alpha}{W} \frac{\partial W}{\partial x_i} \right) , \quad Y_\alpha = \frac{X_\alpha W_\alpha}{W} ,$$

$$W = \sum_\alpha X_\alpha W_\alpha = \left( \sum_\alpha \frac{Y_\alpha}{W_\alpha} \right)^{-1} , \qquad (2.5)$$

or Hirschfelder and Curtiss approximation [47]:

$$v_{\alpha,i} = -\frac{D_\alpha}{X_\alpha} \frac{\partial X_\alpha}{\partial x_i} + v_{C,i} , \quad v_{C,i} = \sum_\alpha \frac{Y_\alpha D_\alpha}{X_\alpha} \frac{\partial X_\alpha}{\partial x_i} , \qquad (2.6)$$

where the correction velocity, $v_{C,i}$ enforces the necessary conditions:

$$\sum_\alpha Y_\alpha = 1 , \quad \sum_\alpha \dot{\omega}_\alpha = 0 , \quad \sum_\alpha Y_\alpha v_{\alpha,i} = 0 , \qquad (2.7)$$

so that the total mass is conserved. As a result, the transport equation of mass, Eq. (2.1a), will be recovered by summing the species equation (2.1d) over all species-$\alpha$.

## 2.2 Simplifying Assumptions

The computational cost associated with the equation set (2.1), as described in Sec. 2.1, is usually prohibitive, hence impractical for simulation purposes. In order for tractable numerical simulations, simplifying assumptions have to be applied on the equations. Such implementations are reasonable because the assumptions generally neglect only physical phenomena that are irrelevant to the combustion problems of this work. The individual assumptions that constitute the working equation set (2.14) are listed below.

1. **Body forces:** Body forces, also referred to as volume forces, usually comprise of only gravitational force (buoyancy effect), unless the reacting flow is subjected to acceleration or electromagnetic fields. Even though buoyancy may increase the jet entrainment rate, it has insignificant effect on the axial decay of velocity and scalars [48]. Since mixing of reactants is more dominant to combustion within the current configurations of interest, body forces are deemed secondary and neglected.

2. **Diffusive fluxes:** As a compromise between the intractable Eq. (2.4) and simplified Eq. (2.5), the Hirschfelder and Curtiss approximation [47], given by Eq. (2.6), is applied in most of the simulations of this study.

3. **Equal species diffusivity:** For turbulent flows, particularly in high Reynolds number ($\mathrm{Re}$), non-premixed cases, the Lewis number:

$$\mathrm{Le}_\alpha = \frac{\kappa}{\rho c_p D_\alpha} = \frac{D_{\mathrm{th}}}{D_\alpha} \, , \tag{2.8}$$

is typically assumed to be unity. This so-called "unity Lewis number" approximation is reasonable because turbulent advection, which affects species and temperature indiscriminately, is usually the dominant transport mechanism of the flow. This dominance of turbulent transport is attributed to the observation that the molecular diffusion and reaction layers of a diffusion flame, where differential diffusion effects are prominent, are typically thin compared to the turbulent length-scale.

However, non-unity Lewis number phenomena in turbulent diffusion hydrocarbon flames have been observed experimentally [49, 50] and numerically [51, 52], and are expected to be more pronounced in hydrogen/air systems due to larger variability in species diffusivities. In addition, the temperature dependence of diffusivity and heat-release will tend to laminarize the nozzle-near region of diffusion flame configurations, in which case the differential diffusion effect may no longer be negligible. In this regard, Pierce [33] has suggested to include the non-unity Lewis number effect with turbulence closure models, by virtue of scale-separation in turbulent flows.

In the present work, the consideration of differential diffusion effects is not pursued, in light of the general decrease in the importance of such effects with axial distance from the nozzle [50]. Furthermore, numerical simulations performed by Pitsch [53] indicate that the incorporation of non-unity Lewis number effect in the nozzle-near region only marginally improves the agreement between experimental and simulation results of hydrocarbon flames.

4. **Ideal gas law:** Using kinetic theory in conjunction with Dalton's law of partial pressures, the ideal gas law for multi-component gases is given by:

$$p = \rho \widehat{R} \sum_{\alpha} \frac{Y_\alpha}{W_\alpha} T = \rho R T \ . \tag{2.9}$$

Under the condition where pressure and temperature are sufficiently far from their corresponding critical values, which is generally true for practical combustion devices, Eq. (2.9) is an accurate representation for real gases [54] and therefore invoked as the equation of state throughout the current work.

5. **Pressure effects:** Dimensional analysis shows that the pressure term in the total specific energy equation (2.1c) scales with the square of the Mach number and can therefore be separated from the other terms. This separation applies also to the total specific enthalpy equation, which can be derived from Eq. (2.1c) with:

$$e = h + \frac{p}{\rho} \ , \quad \frac{\partial \rho e}{\partial t} + \frac{\partial \rho e u_i}{\partial x_i} = \left( \frac{\partial \rho h}{\partial t} + \frac{\partial \rho h u_i}{\partial x_i} \right) + \left( \frac{\partial p}{\partial t} + \frac{\partial p u_i}{\partial x_i} \right) \ . \tag{2.10}$$

In essence, the decoupling with the pressure term indicates that the variations in the thermochemical composition due to small pressure changes are negligible:

$$\phi \left( Y_\alpha, \ e, \ p + \Delta p \right) = \phi \left( Y_\alpha, \ e, \ p \right) + \Delta p \cancel{\frac{\partial \phi}{\partial p}} + \cancelto{0}{\text{HOT}}, \quad \frac{\Delta p}{p} \ll 1 \ . \tag{2.11}$$

For low Mach number, open systems, which this study generally considers, this approximation is reasonable since the deviations from the thermodynamic (background) pressure are typically small.

On the contrary, in high Mach number scenarios, pressure effect may become relevant, affecting the reaction-rate by a factor that is approximately proportional to the turbulence intensity [55]. Consequently, supersonic combustion models should include compressibility effects, as has been attempted by Saghafian *et al.* [56].

6. **Soret and Dufour effects:** Empirical findings suggest that the ratio of thermal dif-

fusion to species diffusion in the last RHS term of Eq. (2.4) is usually small for all pairs of species-$\alpha$ and $\alpha'$ [6], hence the Soret effect is effectively negligible. As a result, the suitability of the Hirschfelder and Curtiss approximation for diffusive fluxes is further substantiated. Being the reciprocal process of the Soret effect due to irreversible thermodynamics [57], the Dufour effect (last term of Eq. (2.3)) will therefore be unimportant as well. Accordingly, these effects are omitted.

7. **Stokes' hypothesis:** General deformation of a Newtonian viscous fluid requires that the trace of the viscous stress tensor sums up to zero (i.e. $\text{Tr}[\sigma] = 0$), so that the mechanical pressure, defined as the negative one-third of the first viscous tensor invariant, is equal to the thermodynamic pressure [58]. Per Stokes' hypothesis [59], the bulk viscosity is assumed to be related to the flow viscosity by:

$$\mu_B + \frac{2}{3}\mu = 0 \ . \tag{2.12}$$

8. **Thermal radiation:** Thermal radiation is a heat transfer mechanism that can influence flame quenching processes, which in turn modify the combustion regime [60]. The effects of radiation can be modeled by optically-thin approximation or Monte-Carlo method, which have been extensively reviewed by Coelho [61]. However, given that radiation does not exhibit a significant feedback, especially in diluted hydrocarbon flame configurations considered by the present work, it is simply neglected in this study.

9. **Thermally perfect gas:** In general, the environment within practical combustion devices will not be so stringent that the pressure affects the specific heat capacities significantly. As a result, the thermally perfect gas model, in which $c_p$ and $c_v$ are functions of temperature only, is usually adequate, thus allowing the species specific enthalpy to be written as:

$$h_\alpha = \int_{T^{\text{Ref}}}^{T} c_{p,\alpha}\left(T'\right)\mathrm{d}T' + \Delta h_{f,\alpha}^{\text{Ref}} = h_{s,\alpha} + \Delta h_{f,\alpha}^{\text{Ref}} \ , \tag{2.13}$$

where the first term on the RHS is the sensible enthalpy, $h_{s,\alpha}$, the second term, commonly known as the chemical enthalpy, represents the heat-release due to mass formation, and the superscript Ref indicates that the quantity is taken with respect to reference conditions, which are typically $T^{\text{Ref}} = 298.15 \text{ K}$ and $p^{\text{Ref}} = 1 \text{ bar}$.

10. **Viscous heating:** Using dimensional arguments, the viscous heating effect in the energy equation (2.1c) is shown to scale with the ratio of the square of the Mach num-

ber to the Reynolds number, $\mathcal{O}(\mathrm{Ma}^2\mathrm{Re}^{-1})$. Since the current work focuses mainly on cases that are characterized by low Mach number and moderate Reynolds number, the viscous dissipation effect is appropriately neglected. In high Mach number flows, however, viscous heating will require consideration and may be estimated by compressible, high Mach number combustion models such as that developed in Ref. [56].

Applying these simplifying assumptions to Eqs. (2.1), the resulting working equation set is given by:

$$\frac{\partial \rho}{\partial t} + \frac{\partial \rho u_i}{\partial x_i} = 0 \; , \tag{2.14a}$$

$$\frac{\partial \rho u_i}{\partial t} + \frac{\partial \rho u_i u_j}{\partial x_j} = -\frac{\partial p}{\partial x_i} + \frac{\partial}{\partial x_j}\left[ 2\mu \left( s_{ij} - \frac{1}{3}\frac{\partial u_k}{\partial x_k}I_{ij} \right) \right] \; , \tag{2.14b}$$

$$\frac{\partial \rho T}{\partial t} + \frac{\partial \rho T u_i}{\partial x_i} = \frac{1}{c_p}\frac{\partial}{\partial x_i}\left[ \kappa \frac{\partial T}{\partial x_i} \right] - \sum_{\alpha} \frac{\rho}{c_p} c_{p,\alpha}\frac{\partial T}{\partial x_i}Y_\alpha v_{\alpha,i} - \sum_{\alpha} \frac{\rho}{c_p}\left( h_\alpha \dot{\omega}_\alpha \right) \; , \tag{2.14c}$$

$$\frac{\partial \rho Y_\alpha}{\partial t} + \frac{\partial \rho Y_\alpha u_i}{\partial x_i} = -\frac{\partial \rho Y_\alpha v_{\alpha,i}}{\partial x_i} + \rho \dot{\omega}_\alpha \; , \tag{2.14d}$$

with $v_{\alpha,i}$, equation of state, and $h_\alpha$ described by Eqs. (2.6), (2.9), and (2.13), respectively.

Note that we have replaced the total specific energy equation (2.1c) with the temperature equation (2.14c) for the reason that the latter is more physically relatable, but the two equations are essentially equivalent. In fact, Eq. (2.14c) can be derived from the simplified form of Eq. (2.1c) [62] by considering the kinetic energy equation (total specific energy is the sum of internal and kinetic energies), energy-enthalpy relation (2.10), and assumption of a thermally perfect gas. However, the use of the temperature equation will not be suitable in high Mach number condition, in which the total specific energy or enthalpy equation should be employed instead.

## 2.3   LES Filtering Technique

In this work, the numerical simulations are performed in the context of the LES methodology, which essentially solves the governing equations (2.14) on a computational grid that is too coarse to represent the smallest spatial scales. However, turbulence theory dictates that all relevant scales be coupled, thus necessitating turbulence models that accommodate the interactions between the resolved- and subgrid-scales (SGS). The derivation of such models is most intuitively demonstrated by considering the omission of small scales by LES as a *high-pass filtering* (i.e. low-pass in frequency space) procedure on the governing

equations. This filtering process can be defined as a convolution [14]:

$$\overline{\phi}\left(x_i\right) = \int \phi\left(x_i'\right) \mathcal{G}\left(x_i - x_i';\ \Delta_i\right) \mathrm{d}x_i' \, , \tag{2.15a}$$

$$\widetilde{\phi}\left(x_i\right) = \frac{1}{\overline{\rho}\left(x_i\right)} \int \rho\left(x_i'\right) \phi\left(x_i'\right) \mathcal{G}\left(x_i - x_i';\ \Delta_i\right) \mathrm{d}x_i' \, , \tag{2.15b}$$

where $\overline{(\ )}$ and $\widetilde{(\ )}$ denote the spatial-filter and Favre-filter (i.e. density-weighted), respectively, and $\mathcal{G}(\ ;\ \Delta_i)$ is the spatial-filter operator for a given filter width of $\Delta_i$. Note that the integration will formally be a function of time, $t$, as well, which we have neglected in Eqs. (2.15) for ease of discussion. The filter kernel $\mathcal{G}$ has to conserve constants, so:

$$\int \mathcal{G}(x_i - x_i';\ \Delta_i) \mathrm{d}x_i' = 1 \, . \tag{2.16}$$

The Favre-filtered quantities are related to the spatial-filtered quantities by:

$$\overline{\rho}\widetilde{\phi} = \overline{\rho\phi} = \overline{\rho}\overline{\phi} + \overline{(\rho\phi)'} \, , \tag{2.17}$$

where $\overline{(\phi\psi)'} = \overline{\phi\psi} - \overline{\phi}\overline{\psi}$ is the SGS variance of the spatial-filtered scalar product $(\phi\psi)$.

The use of Eq. (2.15), however, is strictly for illustrative purposes, and is not explicitly implemented in the present study. Instead, this work applies the method of implicit filtering, in which the filter is defined by the computational grid. Therefore, the definition of $\mathcal{G}(\ ;\ \Delta_i)$ is ambiguous and grid-dependent.

## 2.3.1 Governing Equations

Using the convolution equation (2.15), the Favre-filtered working equations are given by:

$$\frac{\partial \overline{\rho}}{\partial t} + \frac{\partial \overline{\rho}\widetilde{u}_i}{\partial x_i} = 0 \, , \tag{2.18a}$$

$$\frac{\partial \overline{\rho}\widetilde{u}_i}{\partial t} + \frac{\partial \overline{\rho}\widetilde{u}_i\widetilde{u}_j}{\partial x_j} = -\frac{\partial \overline{p}}{\partial x_i} + \frac{\partial}{\partial x_j}\left[2\overline{\rho}\widetilde{\nu}\left(\widetilde{s}_{ij} - \frac{1}{3}\frac{\partial \widetilde{u}_k}{\partial x_k}I_{ij}\right)\right] + \frac{\partial(\overline{\sigma_{ij}})^{\mathrm{SGS}}}{\partial x_j} \, , \tag{2.18b}$$

$$\frac{\partial \overline{\rho}\widetilde{T}}{\partial t} + \frac{\partial \overline{\rho}\widetilde{T}\widetilde{u}_i}{\partial x_i} = \frac{1}{\widetilde{c}_p}\frac{\partial}{\partial x_i}\left[\overline{\rho\left(\frac{\kappa}{\rho}\right)}\frac{\partial \widetilde{T}}{\partial x_i}\right] - \sum_\alpha \frac{\overline{\rho}}{\widetilde{c}_p}\widetilde{c_{p,\alpha}\frac{\partial T}{\partial x_i}Y_\alpha \widetilde{v}_{\alpha,i}}$$

$$- \sum_\alpha \frac{\overline{\rho}}{\widetilde{c}_p}\widetilde{\left(h_\alpha \omega_\alpha\right)} + \frac{1}{\widetilde{c}_p}\frac{\partial(\overline{\sigma_{T,i}})^{\mathrm{SGS}}}{\partial x_i} - \frac{\overline{\rho}}{\widetilde{c}_p}\widetilde{\left(u_i T\right)''}\frac{\partial \widetilde{c}_p}{\partial x_i} \, , \tag{2.18c}$$

$$\frac{\partial \overline{\rho}\widetilde{Y}_\alpha}{\partial t} + \frac{\partial \overline{\rho}\widetilde{Y}_\alpha\widetilde{u}_i}{\partial x_i} = -\frac{\partial \overline{\rho}\widetilde{Y_\alpha v_{\alpha,i}}}{\partial x_i} + \overline{\rho}\widetilde{\omega}_\alpha + \frac{\partial(\overline{\sigma_{\alpha,i}})^{\mathrm{SGS}}}{\partial x_i} \, . \tag{2.18d}$$

15

The SGS turbulent fluxes of Eqs. (2.18b)–(2.18d) can be expanded as:

$$(\overline{\sigma_{ij}})^{\text{SGS}} = -\bar{\rho}\widetilde{(u_i u_j)}'' + \overline{\bar{\rho}\left(\nu\left(s_{ij} - \frac{1}{3}\frac{\partial u_k}{\partial x_k}I_{ij}\right)\right)}'' , \tag{2.19}$$

$$(\overline{\sigma_{T,i}})^{\text{SGS}} = -\bar{\rho}\tilde{c}_p\widetilde{(u_i T)}'' + \overline{\bar{\rho}\left(\frac{\kappa}{\rho}\frac{\partial T}{\partial x_i}\right)}'' - \bar{\rho}\sum_\alpha \overline{\left(c_{p,\alpha}\frac{\partial T}{\partial x_i}Y_\alpha v_{\alpha,i}\right)}'' , \tag{2.20}$$

$$(\overline{\sigma_{\alpha,i}})^{\text{SGS}} = -\bar{\rho}\widetilde{(u_i Y_\alpha)}'' - \bar{\rho}\widetilde{(v_{\alpha,i}Y_\alpha)}'' , \tag{2.21}$$

where $\widetilde{(\phi\psi)}'' = \widetilde{\phi\psi} - \tilde{\phi}\tilde{\psi}$ is the SGS variance of the Favre-filtered $\phi\psi$. Based on observations [62] that the first term on the RHS of the Eqs. (2.19)–(2.21) is usually dominating, all the other contributions are neglected in the present work. Dynamic models for the remaining residual contributions are described in the following section.

Wherever applicable, a gradient assumption will be implemented, for instance:

$$\widetilde{D_\alpha\frac{\partial Y_\alpha}{\partial x_i}} = \widetilde{D}_\alpha\frac{\partial \widetilde{Y}_\alpha}{\partial x_i} , \quad \overline{c_p\frac{\partial \overline{\rho T}}{\partial t}} = \tilde{c}_p\frac{\partial \overline{\rho T}}{\partial t} , \quad \widetilde{c_{p,\alpha}\frac{\partial T}{\partial x_i}Y_\alpha} = \widetilde{c_{p,\alpha}}\frac{\partial \widetilde{T}}{\partial x_i}\widetilde{Y}_\alpha , \tag{2.22}$$

while the filtered form of the Hirschfelder and Curtiss approximation and equation of state are, respectively, evaluated as:

$$\widetilde{v_{C,i}} = \sum_\alpha \widetilde{Y}_\alpha \widetilde{D}_\alpha\left(\frac{\partial \widetilde{Y}_\alpha}{\partial x_i} + \frac{1}{\widetilde{W}}\frac{\partial \widetilde{W}}{\partial x_i}\right) , \quad \bar{p} = \bar{\rho}\widetilde{R}\widetilde{T} . \tag{2.23}$$

Note that, in the derivation of Eqs. (2.18), the filter operator has been assumed to satisfy the commutation property [14]:

$$\int \mathcal{G}(x_i - x_i';\ \Delta_i)\frac{\partial \phi(x_i')}{\partial x_i}\mathrm{d}x_i' = \frac{\partial}{\partial x_i}\left[\int \mathcal{G}(x_i - x_i';\ \Delta_i)\phi(x_i')\mathrm{d}x_i'\right] . \tag{2.24}$$

In principle, this property is only true for homogeneous filters. However, the error incurred by non-homogeneous filters, which has been studied in Ref. [63], is commonly neglected.

### 2.3.2 SGS Closure Models

The turbulent SGS fluxes of Eqs. (2.19)–(2.21) are modeled by a dynamic approach [64–66], which essentially improves on the Smagorinsky model [67] by dynamically determining the model parameter, $\mathcal{C}_S$. As a result, the model parameter becomes a function of space and time, instead of a constant of $0.1 \lesssim \sqrt{\mathcal{C}_S} \lesssim 0.2$, as suggested by several preceding studies [68–70].

The basis of the dynamic approach is given by the eddy-viscosity assumption:

$$(\overline{\sigma_{ij}})^{\text{SGS}} = -\overline{\rho}\widetilde{(u_i u_j)}'' = 2\overline{\rho}\widetilde{\nu}_t \widetilde{s}_{ij} - \frac{2}{3}\overline{\rho}\widetilde{(k)}'' I_{ij} \,, \qquad (2.25)$$

where the SGS kinetic energy, $\widetilde{(k)}'' = 0.5\widetilde{(u_k u_k)}''$, is usually small and therefore neglected, and the eddy viscosity, $\widetilde{\nu}_t$, is given by the Smagorinsky model [67]:

$$\widetilde{\nu}_t = \mathcal{C}_S \|\Delta_i\|^2 \|\widetilde{s_{ij}}\| \,, \quad \|\widetilde{s_{ij}}\| = \sqrt{2\widetilde{s_{ij}}\widetilde{s_{ij}}} \,. \qquad (2.26)$$

In order to extract information for the SGS dissipation from the smallest resolved scales, a test-filter, $\widehat{\Delta}$, which has a larger filter-width than the LES grid-spacing (i.e. $\widehat{\Delta} > \|\Delta_i\|$), is introduced and applied over the SGS turbulent flux:

$$\widehat{(\overline{\sigma_{ij}})}^{\text{SGS}} = -\left(\widehat{\overline{\rho}\widetilde{u_i}\widetilde{u_j}} - \widehat{\overline{\rho}\widetilde{u_i}\widetilde{u_j}}\right) = 2\widehat{\overline{\rho}\mathcal{C}_S \|\Delta_i\|^2 \|\widetilde{s_{ij}}\| \widetilde{s_{ij}}} - \frac{2}{3}\widehat{\overline{\rho}\widetilde{(k)}''} I_{ij} \,. \qquad (2.27)$$

Assuming that a similarity exists between the turbulent scales [71], the corresponding unresolved turbulent flux at the test-filter level is given by:

$$\widehat{\mathcal{S}}_{ij} = -\left(\widehat{\overline{\rho}\widetilde{u_i}\widetilde{u_j}} - \widehat{\overline{\rho}}\widehat{\widetilde{u}}_i\widehat{\widetilde{u}}_j\right) = 2\widehat{\overline{\rho}}\mathcal{C}_S\widehat{\Delta}^2\|\widehat{\widetilde{s_{ij}}}\|\widehat{\widetilde{s_{ij}}} - \frac{2}{3}\widehat{\overline{\rho}\widetilde{(k)}''} I_{ij} \,. \qquad (2.28)$$

The Germano identity is then given by subtracting Eq. (2.28) from Eq. (2.27) :

$$\widehat{\mathcal{L}}_{ij} = \widehat{\overline{\rho}}\widehat{\widetilde{u}}_i\widehat{\widetilde{u}}_j - \widehat{\overline{\rho}\widetilde{u_i}\widetilde{u_j}} = 2\widehat{\overline{\rho}}\mathcal{C}_S\widehat{\Delta}^2\left\|\widehat{\widetilde{s_{ij}}}\right\|\widehat{\widetilde{s_{ij}}} - 2\widehat{\overline{\rho}\mathcal{C}_S \|\Delta_i\|^2 \|\widetilde{s_{ij}}\| \widetilde{s_{ij}}} \,, \qquad (2.29)$$

from which the Smagorinsky model parameter, $\mathcal{C}_S$, can be determined. However, this system of equations is over-determined, and is thus solved with a least-square method [65] under the assumption that $\mathcal{C}_S$ has small spatial and temporal variabilities:

$$\mathcal{C}_S = \frac{1}{2}\frac{\langle\widehat{\mathcal{L}}_{ij}\widehat{\mathcal{M}}_{ij}\rangle}{\langle\widehat{\mathcal{M}}_{ij}\widehat{\mathcal{M}}_{ij}\rangle} \,, \quad \widehat{\mathcal{M}}_{ij} = \widehat{\overline{\rho}}\widehat{\Delta}^2\left\|\widehat{\widetilde{s_{ij}}}\right\|\widehat{\widetilde{s_{ij}}} - \widehat{\overline{\rho} \|\Delta_i\|^2 \|\widetilde{s_{ij}}\| \widetilde{s_{ij}}} \,, \qquad (2.30)$$

where $\langle\,\rangle$ indicates averaging along the spatially homogeneous directions.

Similar to the SGS turbulent flux, the residual scalar fluxes are modeled as:

$$(\overline{\sigma_{\phi,i}})^{\text{SGS}} = -\overline{\rho}\widetilde{(u_i\phi)}'' = \overline{\rho}\widetilde{D}_t\frac{\partial\widetilde{\phi}}{\partial x_i} \,, \quad \widetilde{D}_t = \mathcal{C}_\phi \|\Delta_i\|^2 \|\widetilde{s_{ij}}\| \,, \quad \mathcal{C}_\phi = \frac{1}{2}\frac{\langle\widehat{\mathcal{L}}_\phi\widehat{\mathcal{M}}_\phi\rangle}{\langle\widehat{\mathcal{M}}_\phi\widehat{\mathcal{M}}_\phi\rangle} \,,$$

$$\widehat{\mathcal{L}}_\phi = \widehat{\overline{\rho}}\widehat{\widetilde{u}}_i\widehat{\widetilde{\phi}} - \widehat{\overline{\rho}\widetilde{u_i}\widetilde{\phi}} \,, \quad \widehat{\mathcal{M}}_\phi = \widehat{\overline{\rho}}\widehat{\Delta}^2\left\|\widehat{\widetilde{s_{ij}}}\right\|\frac{\partial\widehat{\widetilde{\phi}}}{\partial x_i} - \widehat{\overline{\rho} \|\Delta_i\|^2 \|\widetilde{s_{ij}}\| \frac{\partial\widetilde{\phi}}{\partial x_i}} \,. \qquad (2.31)$$

# CHAPTER 3

# Classical Flamelet Models

Building on Williams' concept of laminar flamelets in a turbulent diffusion flame [72], Peters [7,73] developed the class of flamelet models for turbulent combustion. These flamelet-type models share a common view that the turbulent diffusion flame can be considered as an ensemble of laminar flamelets, which is embedded in and interacts with the surrounding turbulent flow. At sufficiently high activation energy, chemical reactions and heat transfer are confined to a thin reaction-diffusion layer. The order of the activation energy in a reacting flow can be characterized by the Damköhler number, $\mathrm{Da}$:

$$\mathrm{Da} = \frac{t^{\mathrm{Flow}}}{t^{\mathrm{Chem}}} \, , \tag{3.1}$$

which indicates the ratio of the characteristic convection time to the characteristic reaction time, respectively. Hence, a large $\mathrm{Da}$ will correspond to a high activation energy, and vice versa.

A flamelet regime exists if the characteristic length-scale of the reaction-diffusion layer is smaller than the smallest turbulent scale [9], in which case the turbulent structures are unable to penetrate or destroy the reaction zone of the flame. Consequently, the effect of turbulence will result only in a deformation and stretching of the flame-structure, a causality that can be described by the flamelet equations, which will be derived in Sec. 3.1. Note that, in strongly turbulent flows, the characteristic convection time may be comparable to the characteristic chemical time, so non-equilibrium effects may require consideration.

## 3.1 Mixture-Fraction

The transport of energy and species in a turbulent diffusion flame is governed by a competition between advection, diffusion, and reaction. Since the turbulent transport typically controls mixing, the flame-structure, which is characterized by a reaction-diffusion layer,

can be solved separately from the turbulent flow dynamics [74] by an implicit consideration of the mixing phenomena, analogous to the Lagrangian particle-tracking method. For this consideration, the mixture-fraction, a conserved scalar that quantifies the mixedness of a flow, is evidently the logical candidate.

The mixture-fraction, $Z$, can be defined by a coupling function that is derived from elemental mass fractions [75]:

$$Z = \frac{\mathcal{Z} - \mathcal{Z}_O}{\mathcal{Z}_F - \mathcal{Z}_O} \ , \quad \mathcal{Z} = \sum_\beta \sum_\alpha \left[ \gamma_\beta \frac{n_{\alpha\beta} W_\beta}{W_\alpha} Y_\alpha \right] \ , \tag{3.2}$$

where the subscripts $(\ )_F$ and $(\ )_O$ refer to conditions in the fuel and oxidizer streams, respectively. With this definition, a transport equation for mixture-fraction can be derived from a linear combination of the species conservation equation (2.14d):

$$\frac{\partial \rho Z}{\partial t} + \frac{\partial \rho Z u_i}{\partial x_i} = \frac{\partial}{\partial x_i} \left[ \rho D_Z \frac{\partial Z}{\partial x_i} \right] + \frac{\partial \rho \varepsilon_i}{\partial x_i} \ , \quad D_Z = D_{\text{th}} = \frac{\kappa}{\rho c_p} \ , \tag{3.3}$$

where $\varepsilon_i$ is a variable that represents the differential diffusion effect [76] and is given by:

$$\varepsilon_i = \frac{-1}{\mathcal{Z}_F - \mathcal{Z}_O} \sum_\beta \sum_\alpha \left[ \gamma_\beta \frac{n_{\alpha\beta} W_\beta}{W_\alpha} Y_\alpha v_{\alpha,i} \right] - D_Z \frac{\partial Z}{\partial x_i} \ . \tag{3.4}$$

For unity Lewis number cases, $\varepsilon_i$ will reduce to $0$, and the mixture-fraction definition by Eq. (3.3) will be identical to that of Pitsch and Peters [77].

The flamelet equations can be derived by considering a local coordinate system that attaches to the mixture-fraction iso-surface:

$$\boldsymbol{z} = [Z(x_j, t), \ Z_2(x_j, t), \ Z_3(x_j, t)]^T \ ,$$

where $Z_2$ and $Z_3$ denote any two orthogonal directions that span the local tangent plane of the iso-surface. The coordinate transformation of partial-differential operators is then given by a Crocco-type transformation [78]:

$$(\boldsymbol{x}, t) \to (\boldsymbol{z}, \tau) \ ,$$

$$\frac{\partial}{\partial t} \to \frac{\partial}{\partial \tau} + \frac{\partial Z}{\partial t} \frac{\partial}{\partial Z} - (u_i - (u_k \widehat{n}_{Z,k}) \widehat{n}_{Z,i}) \frac{\partial}{\partial x_i} \ , \quad \frac{\partial}{\partial x_i} \to \frac{\partial Z}{\partial x_i} \frac{\partial}{\partial Z} + \frac{\partial Z_k}{\partial x_i} \frac{\partial}{\partial Z_k} \ , \tag{3.5}$$

where $\widehat{n}_{Z,i} = \nabla Z / \|\nabla Z\|$ denotes the normalized gradient of mixture-fraction. Note that the advection term in the temporal transformation of Eq. (3.5) arises from the consideration of a local mixture-fraction coordinate system and accounts for the motion of the iso-surface.

19

Applying the transformation to the temperature and species equations (2.14c)–(2.14d) and using the mixture-fraction transport equation (3.3):

$$\frac{\partial T}{\partial \tau} = \frac{\chi_Z}{2} \frac{\partial^2 T}{\partial Z^2} - \sum_\alpha \frac{1}{c_p} h_\alpha \dot{\omega}_\alpha$$

$$+ \frac{\chi_Z}{2c_p} \left( \frac{\partial c_p}{\partial Z} + \sum_\alpha \left[ \frac{c_{p,\alpha}}{\mathrm{Le}_\alpha} \left( \frac{\partial Y_\alpha}{\partial Z} + \frac{Y_\alpha}{W} \frac{\partial W}{\partial Z} \right) \right] \right) \frac{\partial T}{\partial Z}$$

$$- \frac{\partial Z}{\partial x_i} \left( \frac{\partial v_{C,i}}{\partial Z} + \frac{\partial \rho \varepsilon_i}{\partial Z} \right) \frac{\partial T}{\partial Z} + \mathrm{HOT}_T , \tag{3.6a}$$

$$\frac{\partial Y_\alpha}{\partial \tau} = \frac{\chi_Z}{2\mathrm{Le}_\alpha} \left( \frac{\partial^2 Y_\alpha}{\partial Z^2} + \frac{Y_\alpha}{W} \frac{\partial^2 W}{\partial Z^2} \right) + \dot{\omega}_\alpha$$

$$+ \frac{1 - \mathrm{Le}_\alpha}{4\rho \mathrm{Le}_\alpha} \left( \frac{\partial \rho \chi_Z}{\partial Z} + \frac{\chi_Z}{D_Z} \frac{\partial \rho D_Z}{\partial Z} - \frac{2\rho \chi_Z}{\mathrm{Le}_\alpha (1 - \mathrm{Le}_\alpha)} \frac{\partial \mathrm{Le}_\alpha}{\partial Z} \right) \frac{\partial Y_\alpha}{\partial Z}$$

$$+ \frac{1}{4\rho \mathrm{Le}_\alpha} \left( \frac{\partial}{\partial Z} \left[ \frac{\rho \chi_Z Y_\alpha}{W} \right] + \frac{\chi_Z}{D_Z} \frac{\partial}{\partial Z} \left[ \frac{\rho D_Z Y_\alpha}{W} \right] - \frac{2\rho \chi_Z Y_\alpha}{\mathrm{Le}_\alpha W} \frac{\partial \mathrm{Le}_\alpha}{\partial Z} \right) \frac{\partial W}{\partial Z}$$

$$- \frac{1}{\rho} \frac{\partial Z}{\partial x_i} \left( \frac{\partial \rho Y_\alpha v_{C,i}}{\partial Z} + \frac{\partial \rho \varepsilon_i}{\partial Z} \frac{\partial Y_\alpha}{\partial Z} \right)$$

$$- \frac{1}{\mathrm{Le}_\alpha} \kappa_Z \sqrt{\frac{D_Z \chi_Z}{2}} \left( (\mathrm{Le}_\alpha - 1) \frac{\partial Y_\alpha}{\partial Z} + \frac{Y_\alpha}{W} \frac{\partial W}{\partial Z} \right) + \mathrm{HOT}_\alpha , \tag{3.6b}$$

where $\chi_Z = 2 D_Z \|\nabla Z\|^2$ is the scalar-dissipation rate of mixture-fraction, which can be interpreted as the reciprocal of the characteristic diffusion time and hence describes the local rate of mixing, and $\kappa_Z = \nabla \cdot (\nabla Z / \|\nabla Z\|)$ is the local curvature of the mixture-fraction field. The higher-order terms of Eqs. (3.6a)–(3.6b) correspond to the terms in the $Z_2$- and $Z_3$-directions, and are shown by Peters' asymptotic analysis [9] to be insignificant relative to the terms in the $Z$-direction. The expanded forms of the $v_{C,i}$-containing term and HOT for the temperature and species equations are expanded in Appendix A, and are not written in the above in the interest of brevity.

## 3.2 Scalar-Dissipation Rate

Neglecting all higher-order terms, the flamelet equations (3.6) are one-dimensional partial differential equations that can be solved in terms of the flamelet time, $\tau$, and mixture-fraction space, $Z$, for a given profile of the scalar-dissipation rate, $\chi_Z$. In turbulent flows, the scalar-dissipation rate distribution is affected by the surrounding turbulent structures and can therefore be interpreted as the boundary condition of the flamelet equations that couples the flame and turbulence dynamics. This interpretation, however, indicates that

the scalar-dissipation rate has to be modeled in the flamelet model, because the exact $\chi_Z$-profile will assert that the transport and corresponding flamelet equations be equivalent. Hence, there is no advantage to solving Eqs. (3.6a)–(3.6b) over Eqs. (2.14c)–(2.14d).

For a one-dimensional mixing layer problem, Peters [73] showed that $\chi_Z$ has an analytical expression:

$$\chi_Z (Z) = \chi_{Z,\text{st}} \exp \left[ 2 \left( \left( \text{erfc}^{-1} [2Z_{\text{st}}] \right)^2 - \left( \text{erfc}^{-1} [2Z] \right)^2 \right) \right] , \tag{3.7}$$

where $\text{erfc}^{-1}$ is the inverse complementary error function. Analytical scalar-dissipation rate profile are also derived for a semi-infinite mixing layer [79]:

$$\chi_Z (Z) = \chi_{Z,\text{st}} \left( \frac{Z}{Z_{\text{st}}} \right)^2 \frac{\ln [Z]}{\ln [Z_{\text{st}}]} , \tag{3.8}$$

which can allow for a better description of the complete fuel-air mixing.

Using analytical expressions of mixture-fraction for the scalar-dissipation rate, such as Eqs. (3.7)–(3.8), and neglecting the temporal derivative of the flamelet equations (3.6), the thermochemical structure of a flamelet, $\boldsymbol{\phi} = [T, Y_\alpha]$, can then be represented by a two-dimensional manifold of the form:

$$\boldsymbol{\phi} = \mathcal{F}_{\boldsymbol{\phi}} (Z, \chi_{Z,\text{st}}) . \tag{3.9}$$

The manifold described by Eq. (3.9) is the steady laminar flamelet model (SLFM) and can be illustrated by the S-shaped curve, as shown by the solid lines of the left plot in Fig. 3.1. The S-shaped curve can be sub-divided into three distinctive branches, namely the upper (stable, reacting), middle (unstable, reacting), and lower (stable, non-reacting) branches; instability of the middle branch refers to the tendency for the solution to move away from the branch when perturbed, towards the upper branch when the scalar-dissipation rate decreases (i.e. $\Delta \chi_{Z,\text{st}} < 0$; leftward shift relative to the S-shaped curve), and vice versa.

The omission of the temporal dependence by the SLFM implies that the flame-structure has an infinitely fast response time to changes in the scalar-dissipation rate, which will require the time-scale of $\chi_Z$ be significantly slower than that of thermochemistry. In cases where this condition is not satisfied, the transient term in Eqs. (3.6) has to be retained. Several models, for example the *ad hoc* SLFM [80], representative interactive flamelets (RIF) model [81], and Eulerian particle flamelet model (EPFM) [82], have been developed to accommodate unsteady effects by considering a time-varying scalar-dissipation rate. The unsteady flame response to changes in $\chi_Z$ has been studied by Cuenot *et al.* [83]. For turbu-
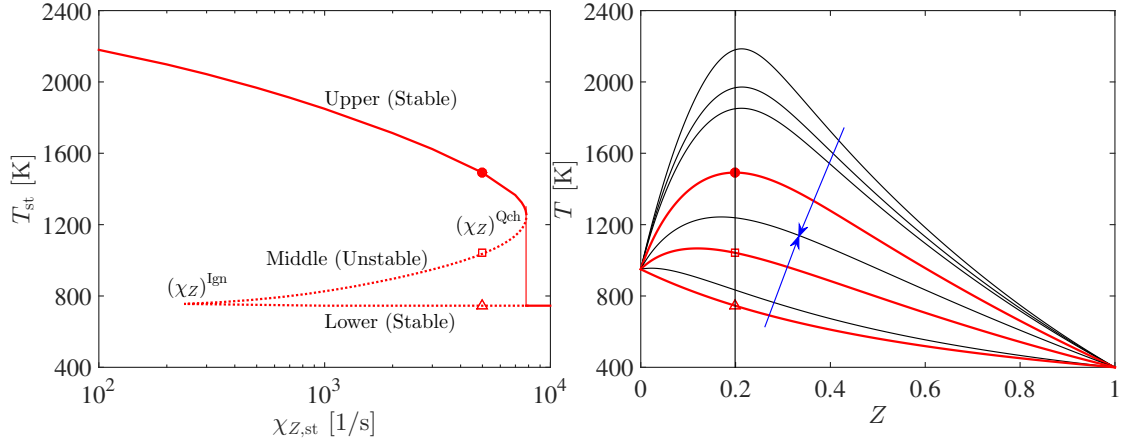
Figure 3.1: Illustration of a S-shaped curve (left) and the flamelet solutions (right). In the left plot, the solid and dotted lines denote the SLFM and FPV state-space trajectories, respectively. The vertical line in the right plot refers to the stoichiometric mixture-fraction, while the two arrows indicate the direction in which $\chi_{Z,\text{st}}$ increases. The solution on which the two arrows meet is the flame-quenching solution, denoted by $(\chi_Z)^{\text{Qch}}$ on the S-shaped curve. For illustration, the various solutions for $\chi_{Z,\text{st}} = 5000\ 1/\text{s}$ are denoted by the symbols and thickened lines on, while the thin lines are solutions at other $\chi_{Z,\text{st}}$ values.

lent jet diffusion flames, the relevant time-scale can be described by the flamelet residence time, $\tau$:

$$\tau\left(x_i\right) = \int_0^{x_i} \left( \left\| u_i\left(x_i'\right) - \frac{u_k\left(x_i'\right)}{\left\|\nabla Z\left(x_i'\right)\right\|^2} \frac{\partial Z\left(x_i'\right)}{\partial x_k} \frac{\partial Z\left(x_i'\right)}{\partial x_i} \right\| \Big|_{Z_{\text{st}}} \right)^{-1} \mathrm{d}x_i' , \qquad (3.10)$$

where the second term of the integrand denotes the advection component normal to the stoichiometric mixture-fraction iso-surface.

## 3.3 Reaction Progress-Variable

From Fig. 3.1, the use of the manifold by Eq. (3.9) will not provide a unique parameterization of the entire S-shaped curve since multiple solutions exist for any scalar-dissipation rate value within the range: $(\chi_Z)^{\text{Ign}} \leq \chi_Z \leq (\chi_Z)^{\text{Qch}}$. Therefore, the implementation of the SLFM is typically limited to only the upper branch of the S-shaped curve, unless the manifold is filtered with a log-normal distribution over the $\chi_Z$-space [33]. Otherwise, the SLFM is formally consistent only in steady-state calculations of fully-ignited flames [84].

In order to access the flamelet solutions along the middle branch of the S-shaped curve, Pierce & Moin [10, 33] developed the FPV model, wherein the thermochemical structure

of a flamelet is given by:

$$\boldsymbol{\phi} = \mathcal{F}_{\boldsymbol{\phi}}\left(Z,\,\Lambda\right)\,. \tag{3.11}$$

In Eq. (3.11), $\Lambda$ is any indicator of the reaction progress that satisfies the two constraints: (i) $\Lambda$ uniquely identifies all flame states along the entire S-shaped curve [85]; and (ii) $\Lambda$ is statistically independent of the mixture-fraction. Therefore, a possible definition of $\Lambda$ will be the stoichiometric value of a reaction progress-variable, $C$:

$$\Lambda = C|\,Z_{\mathrm{st}}\,, \tag{3.12}$$

where $C$ can be represented by the temperature or a linear combination of major species product mass fractions. Hence, $C$ is also described by the FPV manifold:

$$C = \mathcal{F}_C\left(Z,\,\Lambda\right)\,. \tag{3.13}$$

In practice, the FPV model makes use of $(Z,\,C)$, instead of $(Z,\,\Lambda)$, to parameterize the thermochemical states:

$$\boldsymbol{\phi} = \mathcal{F}_{\boldsymbol{\phi}}\left(Z,\,C\right) = \mathcal{F}_{\boldsymbol{\phi}}\left(Z,\,\mathcal{F}_C^{-1}\left(Z,\,C\right)\right)\,, \quad \Lambda = \mathcal{F}_C^{-1}\left(Z,\,C\right)\,, \tag{3.14}$$

where the inverse function-mapping $\mathcal{F}_C^{-1}\left(Z,\,C\right)$ implies that $\mathcal{F}_C$ is bijective. This approach is taken in order to circumvent the non-trivial complexities in solving the transport equation of $\Lambda$ [35]. On the contrary, the definition of $C$ as the temperature or a linear combination of species indicates that the transport equation of $C$ is typically well-defined and convenient to solve. To further reduce the ambiguity in the definition of $C$ as a combination of a pre-defined set of $Y_\alpha$, an optimization problem [86] can be solved to enforce a monotonicity condition on $C$:

$$\frac{\partial C}{\partial \Lambda} > \epsilon \geq 0\,, \tag{3.15}$$

thus satisfying the bijective property of $\mathcal{F}_C\left(Z,\,\Lambda\right)$. However, an optimal progress-variable appears to give only marginal improvements in simulation results [35, 84], suggesting that the definition of $C$ may be a secondary factor in representing the thermochemical states.

While its ability to access the entire S-shaped curve certainly gives the FPV model a wider applicability than the SLFM model, the FPV model should not be mistaken for a transient flamelet model. In fact, the FPV model is a steady-state model that will, by design, drive the simulation results towards the steady flamelet solutions given by the S-shaped curve. Ihme [35] has pointed out that a flamelet with a particular $\Lambda$-value can correspond to either an extinguishing, reigniting, or steady state, in which the flamelet

will be characterized by a different flame-structure. The differences in flame-structure for the various flamelet states are attributed to the unsteady transport of a flamelet during extinction and reignition [85]. In cases that are far from the transient states, however, the FPV model will be sufficient because its formulation provides the leading-order unsteady flamelet effects, which are due solely to the dynamics of the scalar-dissipation rate [35]. Otherwise, the unsteady FPV model developed by Ihme & See [36] should be considered.

## 3.4   Turbulence Closure

In order to be applicable in LES, which considers filtered quantities (cf. Sec. 2.3.1), flamelet-type models have to accommodate the loss of information with regards to the residual velocity and scalars due to filtering. Considering the approach in flamelet models where the thermochemical states are described by a lower-order manifold, such as that of Eqs. (3.9) and (3.14), Pope's concept of filter-density function (FDF) [87] can be employed to couple the two techniques. This coupling can be described by:

$$\widetilde{\boldsymbol{\phi}} = \int_{\min[\boldsymbol{\psi}]}^{\max[\boldsymbol{\psi}]} \int_{\min[Z]}^{\max[Z]} \mathcal{F}_{\boldsymbol{\phi}}\left(Z,\, \boldsymbol{\psi}\right) \widetilde{P}\left(Z,\, \boldsymbol{\psi}\right) \mathrm{d}Z \mathrm{d}\boldsymbol{\psi} \,, \tag{3.16}$$

where $\widetilde{P}(Z,\, \boldsymbol{\psi})$ is the joint-FDF of $Z$ and $\boldsymbol{\psi}$, which denotes the group of parameterizing variables that the flamelet model in consideration uses for its lower-order manifold. The SLFM and FPV models are obtained when $\boldsymbol{\psi}$ is simply $\chi_{Z,\mathrm{st}}$ and $C$, respectively. Note that $\widetilde{P}(Z,\, \boldsymbol{\psi})$ is formally a function of space and time and pertains to the sample space of $Z$ and $\boldsymbol{\psi}$, but such properties have not been made in Eq. (3.16) for simplicity.

Similar to the relation (2.17), the joint-FDF $\widetilde{P}(Z,\, \boldsymbol{\psi})$ is essentially the density-weighted joint-distribution of $Z$ and $\boldsymbol{\psi}$ within a computational cell, $\overline{P}(Z,\, \boldsymbol{\psi})$:

$$\overline{\rho}\widetilde{P}\left(Z,\, \boldsymbol{\psi}\right) = \rho\left(Z, \boldsymbol{\psi}\right)\overline{P}\left(Z,\, \boldsymbol{\psi}\right) \,. \tag{3.17}$$

Using Bayes' theorem, the joint-FDF can be expressed in terms of a marginal-FDF of $Z$ and a conditional-FDF of $\boldsymbol{\psi}$ with respect to $Z$:

$$\widetilde{P}\left(Z,\, \boldsymbol{\psi}\right) = \frac{\rho}{\overline{\rho}}\overline{P}\left(Z\right)\overline{P}\left(\boldsymbol{\psi}|\,Z\right) = \frac{\overline{\rho}}{\rho}\widetilde{P}\left(Z\right)\widetilde{P}\left(\boldsymbol{\psi}|\,Z\right) \,. \tag{3.18}$$

If $\boldsymbol{\psi}$ is statistically independent of $Z$, the conditional-FDF of $\boldsymbol{\psi}$ in Eq. (3.18) can be

further reduced to the marginal-FDF of $\boldsymbol{\psi}$:

$$\widetilde{P}\left(Z, \boldsymbol{\psi}\right) = \frac{\overline{\rho}}{\rho} \widetilde{P}\left(Z\right) \widetilde{P}\left(\boldsymbol{\psi}\right) \ , \tag{3.19}$$

thus leading to significant simplifications in the representation of the joint-FDF. Therefore, the rationale for the second constraint of the FPV model that $\Lambda$ and $Z$ are statistically independent is now apparent. However, this constraint is only valid in the steady flamelet limit because conditional effects can become important in the presence of flame extinction and reignition [85].

While a FDF-transport equation can be solved for $\widetilde{P}\left(Z, \boldsymbol{\psi}\right)$, such an approach is typically not taken due to its computational complexity and prohibitive cost. Instead, one of the more common methods is to describe the two PDF's of Eqs. (3.18)–(3.19) by presumed distributions, or the so-called presumed-FDF approach. For the marginal-FDF of the mixture-fraction, an often utilized model is the beta distribution, which is parameterized by the filtered mixture-fraction, $\widetilde{Z}$, and its SGS variance, $\widetilde{Z''^2}$. Further details on the presumed beta distribution and closure models for $\widetilde{Z''^2}$ are given in Sec. 5.3.3.

On the other hand, the conditional- or marginal-FDF of $\boldsymbol{\psi}$, which usually comprises of reactive scalars, cannot be easily represented by a presumed shape because of the FDF's multi-modal shape that depends on: (i) turbulence-chemistry interactions; (ii) chemical time-scales; and (iii) higher moment information. Practical models for such a FDF include the (double) delta functions, (clipped) Gaussian functions, beta distribution, and statistically most likely distributions.

Fo the FPV model, Pierce & Moin [10] assumed that the residual state in a computational cell is represented by one single flamelet. Hence, the marginal FDF of $\Lambda$ is given by a delta distribution:

$$\widetilde{P}\left(\Lambda\right) = \delta\left(\Lambda - \widetilde{\Lambda}\right) \ . \tag{3.20}$$

Consequently, the FPV manifold in the context of LES is given by:

$$\widetilde{\mathcal{F}_{\boldsymbol{\phi}}}\left(\widetilde{Z}, \ \widetilde{Z''^2}, \ \widetilde{\Lambda}\right) = \iint \mathcal{F}_{\boldsymbol{\phi}}\left(Z, \Lambda\right) \beta\left(Z; \ \widetilde{Z}, \ \widetilde{Z''^2}\right) \delta\left(\Lambda - \widetilde{\Lambda}\right) \mathrm{d}Z\mathrm{d}\Lambda \ , \tag{3.21}$$

where $\beta\left(Z; \ \widetilde{Z}, \ \widetilde{Z''^2}\right)$ refers to the beta distribution for a given combination of $\widetilde{Z}$ and $\widetilde{Z''^2}$. Following from the assumption of a bijective $\widetilde{\mathcal{F}_{\boldsymbol{\phi}}}$, the relation (3.21) can be inverted to give

a FPV flamelet library:

$$\widetilde{\boldsymbol{\phi}} = \widetilde{\mathcal{F}_{\boldsymbol{\phi}}}\left(\widetilde{Z},\ \widetilde{Z''^2},\ \widetilde{C}\right) = \widetilde{\mathcal{F}_{\boldsymbol{\phi}}}\left(\widetilde{Z},\ \widetilde{Z''^2},\ \widetilde{\mathcal{F}_C}^{-1}\left(\widetilde{Z},\ \widetilde{Z''^2},\ \widetilde{C}\right)\right)\ ,$$
$$\widetilde{\Lambda} = \widetilde{\mathcal{F}_C}^{-1}\left(\widetilde{Z},\ \widetilde{Z''^2},\ \widetilde{C}\right)\ . \tag{3.22}$$

Finally, the utilization of the FPV flamelet library (3.22) in an LES will require that the transport equations of $\widetilde{Z}$, $\widetilde{Z''^2}$, and $\widetilde{C}$ be solved, in place of the temperature and species equations (2.18c)–(2.18d). The working equation set of the FPV model is then given by:

$$\frac{\partial \overline{\rho}\widetilde{Z}}{\partial t} + \frac{\partial \overline{\rho}\widetilde{Z}\widetilde{u}_i}{\partial x_i} = \frac{\partial}{\partial x_i}\left[\overline{\rho}\left(\widetilde{D_Z} + \widetilde{D_t}\right)\frac{\partial \widetilde{Z}}{\partial x_i}\right]\ , \tag{3.23a}$$

$$\frac{\partial \overline{\rho}\widetilde{C}}{\partial t} + \frac{\partial \overline{\rho}\widetilde{C}\widetilde{u}_i}{\partial x_i} = \frac{\partial}{\partial x_i}\left[\overline{\rho}\left(\widetilde{D_C} + \widetilde{D_t}\right)\frac{\partial \widetilde{C}}{\partial x_i}\right] + \overline{\rho}\widetilde{\dot{\omega}_C}\ , \tag{3.23b}$$

along with Eqs. (2.18a)–(2.18b) and Eq. (5.27) for $\widetilde{Z''^2}$. Note that, in Eqs. (3.23), the SGS turbulent fluxes of $\widetilde{Z}$ and $\widetilde{C}$ have been represented by the closure models that are described in Sec. 2.3.2, and $\widetilde{Z}$ is defined in accordance to Pitsch & Peters [77].

Extensions to the aforementioned FPV model have been investigated in Refs. [35] and [88], and applied in the LES simulations [36] of a vitiated co-flow burner [37]. In essence, these extended FPV models will consider a presumed $\Lambda$-distribution that requires higher-moment information, for example the statistically most-likely distribution [89]. As a result, higher-moment transport equations of $\widetilde{C}$ will have to be solved, in addition to the equations (3.23), and modeled in a manner analogous to that for $\widetilde{Z''^2}$ (cf. Sec. 2.3.2).

# CHAPTER 4

# Assessment of Classical Flamelet Assumptions

Most of the flamelet models in the previous chapter adopt Peters' asymptotic assumption that only effects in the $Z$-direction are important [9] and disregard the higher-order terms of the flamelet equations (3.6), and some even assume a steady-state such that the temporal term can be neglected. While applications have shown that such treatments are reasonable, the importance of the transient and higher-order terms is worth exploring. For instance, by modeling one of the higher-order terms, Pitsch *et al.* demonstrated that the flamelet model can capture the reignition phenomenon reasonably [12]. Therefore, two *a-priori* studies [90,91] that specifically investigate the significance of the commonly omitted terms were conducted in this work, as detailed in the following sections. Then, a flamelet regime diagram that accounts for the numerical fidelity will be described as a potential diagnostic tool for future assessments of the flamelet model.

## 4.1   Methodology

To date, investigations have focused largely on the validation of flamelet models for LES and RANS, while underlying assumptions that are associated with the derivation of the flamelet formulation are seldom rigorously evaluated. The main reason for such a lack of evaluations is that these assumptions require information at very fine turbulent scales and thus cannot be fully addressed through experimental and theoretical investigations. Instead, DNS of relevant flame configurations are necessary to systematically examine the flamelet assumptions, including the effects of differential diffusion, omission of higher-order terms, and representation of combustion-physical mechanisms due to flame propagation.

Since a flamelet spans a transformed coordinate system (see Eq. (3.5)), a set of diagnostic techniques that accounts for the transformation [90] was developed to make use of the three-dimensional, Cartesian DNS data for flamelet analyses. The essential steps of the diagnosis are summarized as follow:

**Stoichiometric iso-surface parameterization**

The flamelet coordinate is constructed by tracing along the mixture-fraction gradient, which requires the definition of a certain starting point. Since the greatest contribution of chemical reaction typically occurs within a reaction-zone layer around stoichiometry [9], the logical choice for the starting point will be a stoichiometric location. The description of the entire domain in flamelet perspective demands that multiple flamelets be constructed, thus needing multiple starting points, which collectively represent the stoichiometric iso-surface.

The utilization of the stoichiometric iso-surface requires that the set of starting points be of a finite number, yet sufficient to represent the surface. This requirement is met by a parameterization of the stoichiometric iso-surface, which will be dependent on the flow configuration. In essence, the parameterization will result in a simplified description of the stoichiometric iso-surface, as shown in Fig. 4.1.



(a) Jet-in-crossflow parameterization.      (b) Turbulent counterflow parameterization.
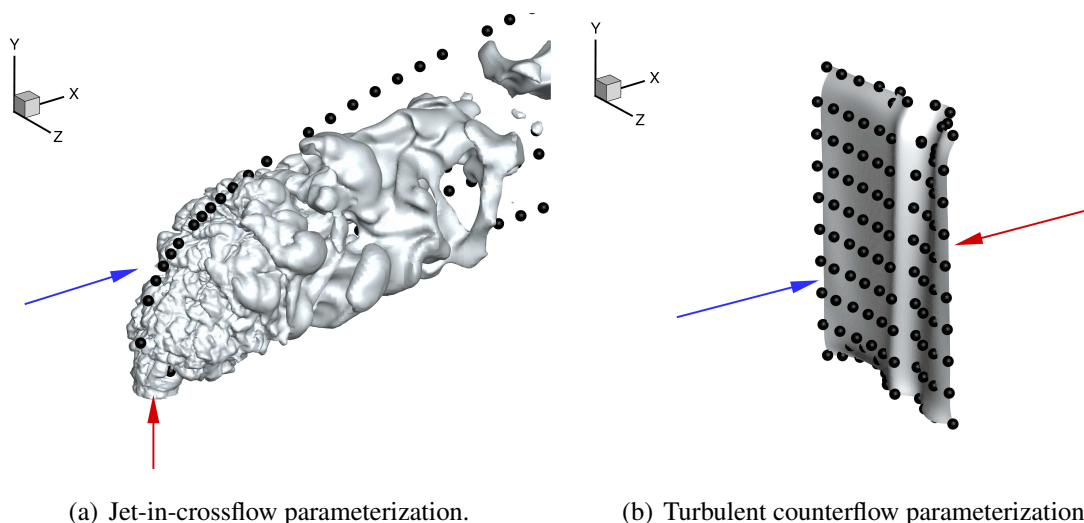
Figure 4.1: Parameterization of the stoichiometric iso-surface for the jet-in-crossflow (left) and turbulent counterflow diffusion flame (right) configurations. In both sub-figures, the iso-surface is the stoichiometric mixture-fraction iso-surface, the two arrows denote the two reactant injection directions, and the symbols indicate the points from the parameterization. Note that the parameterizations are performed using two different methods, which consider: (i) for the jet-in-crossflow, the mean jet-trajectories [92] stemming from four azimuthal locations around the nozzle; and (ii) for the counterflow flame, the points projected from the centerplane to the iso-surface.

## Mixture-fraction gradient tracing

From each stoichiometric point, a flamelet is constructed by tracing along the gradient of the mixture-fraction in both fuel-lean $(-\nabla Z)$ and fuel-rich $(\nabla Z)$ directions. This tracing operation is formally given by the integration, at a particular instant in time, of the following equation:

$$\Delta x_i = \frac{\Delta Z}{\|\nabla Z\|^{-2}} \frac{\partial Z}{\partial x_i} \, , \tag{4.1}$$

where $\Delta Z$ is a user-defined finite spacing in mixture-fraction space. The relation maps the flamelet space to the physical space in a Lagrangian point-of-view, so $\Delta x_i$ refers to the change in position from a previous location, starting from a stoichiometric point. From experience, however, this Lagrangian gradient tracing method is unsuitable for the domain decomposition procedure typical of a parallel programming environment, so an equivalent Eulerian flamelet extraction method is developed and applied in the *a-posteriori* studies of the current work. Following the iso-surface parameterization of Fig. 4.1, the corresponding instantaneous flamelets of the considered flow configurations are illustrated in Fig. 4.2.
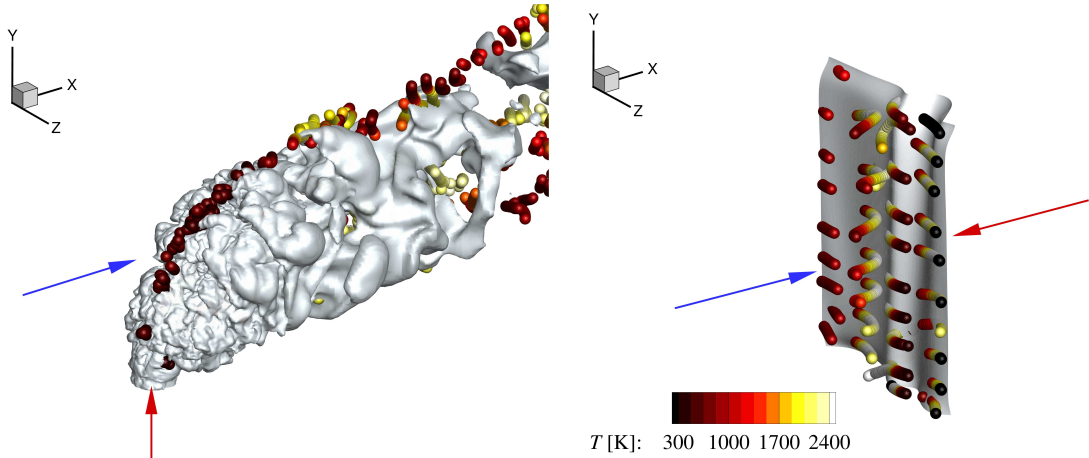


(a) Jet-in-crossflow flamelet extraction.    (b) Turbulent counterflow flamelet extraction.

Figure 4.2: Extracted flamelets following the iso-surface parameterization of Fig. 4.1 for the jet-in-crossflow (left) and turbulent counterflow diffusion flame (right) configurations. The flamelets are colored by temperature. Refer to Fig. 4.1 for further details on the contents of the two plots.

**Conditional averaging**

The three-dimensional, Cartesian mixture-fraction, scalar-dissipation rate, and thermochemical information can be interpolated onto each flamelet, which essentially spans a curve in space, constituting the one-dimensional flamelet species and temperature profiles that satisfy the flamelet equations (3.6). Treating the mixture-fraction as the independent coordinate, these one-dimensional profiles can be averaged to give the mean mixture-fraction conditioned distributions, which give insights to the statistical importance of the individual terms of the flamelet equations. The analysis of the mean flamelet terms can be conducted in the form of a budget analysis, similar to the turbulent kinetic energy budget [93].

The diagnostic tools were applied to the DNS of two different turbulent reacting flows, namely a jet-in-crossflow (JICF) [94,95] and a turbulent lifted jet flame [96,97], as further examined in the following.

## 4.2 Reacting Jet-In-Crossflow

The JICF configuration is schematically illustrated by Fig. 4.3, and the essential parameters of the configuration are given in Tab. 4.1. The JICF configuration is of practical relevance as fuel-injection system for high-speed propulsion applications and as mixing strategies in gas-turbine combustors. Despite its simplistic setup, the JICF configuration is characterized by complex vortical structures, which are associated with shear-layer and horseshoe vortices near the injector and counter-rotating and wake vortices in the jet far-field [98,99]. These vortical structures will control the mixing, ignition, and combustion dynamics, resulting in a significantly more complex flow-field than uni-directional jet flame configurations. Furthermore, the flame stabilization in a reacting JICF is affected by the interactions of different mechanisms, including autoignition, partially-premixed flame behavior, and vortex-induced recirculation modes [95, 100, 101].

In this study, the focus is on the temperature equation (2.14c) without the consideration of correction velocity in the diffusion velocity term. The corresponding temperature flamelet equation is written as:

$$\frac{\partial T}{\partial \tau} = \underbrace{\mathcal{J}_1^Z + \mathcal{J}_2^Z + \mathcal{J}_3^Z + \mathcal{J}_5^Z}_{\text{Flame-aligned contribution}} + \underbrace{\mathcal{J}_4^\perp + \mathcal{J}_5^\perp}_{\text{Flame-orthogonal contribution}} \quad , \tag{4.2}$$

where the flame-aligned terms refer to the first to fourth RHS terms of Eq. (3.6a), rewritten
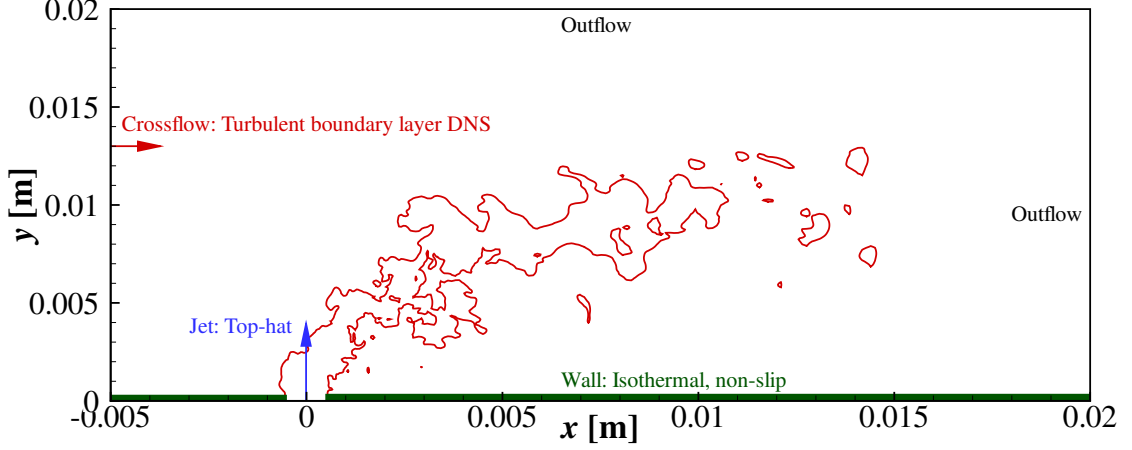
Figure 4.3: JICF DNS configuration and streamwise ($x$) and wall-normal ($y$) boundary conditions [94, 95]; the spanwise ($z$) direction uses a periodic boundary condition. The contour line refers to the stoichiometric mixture-fraction isoline.

| | Parameter | Value |
|---|---|---|
| | Nozzle diameter | 1 mm |
| | Mean velocity | $[0,\ 250,\ 0]^T$ m/s |
| Jet | Composition | $Y_{H_2},\ Y_{N_2} = 0.14,\ 0.86$ |
| | Temperature | 420 K |
| | Jet Reynolds number | 4000 |
| | Mean velocity | $[55,\ 0,\ 0]^T$ m/s |
| Crossflow | Composition | $Y_{O_2},\ Y_{N_2} = 0.23,\ 0.77$ |
| | Temperature | 750 K |
| Domain size | | $25 \times 20 \times 20$ mm |
| Grid resolution | | $1408 \times 1080 \times 1100$ |
| Chemical kinetics | | 9 species, 19 reactions [102] |
| Stoichiometric mixture-fraction | | 0.17 |
| Momentum ratio, $\sqrt{\left(\rho\,\|u_i\|^2\right)_{\text{Jet}}/\left(\rho\,\|u_i\|^2\right)_{\text{Crossflow}}}$ | | 3.5 |
| Velocity fluctuation, $\left(\|u_i'\|\,/\,\|u_i\|\right)_{\text{Crossflow}}$ | | 0.1 |

Table 4.1: Essential parameters of the JICF DNS by Grout *et al.* [94,95].

here for reference:

$$\frac{\partial T}{\partial \tau} = \frac{\chi_Z}{2}\frac{\partial^2 T}{\partial Z^2} - \sum_\alpha \frac{1}{c_p} h_\alpha \dot{\omega}_\alpha$$

$$+ \frac{\chi_Z}{2c_p}\left(\frac{\partial c_p}{\partial Z} + \sum_\alpha \left[\frac{c_{p,\alpha}}{\text{Le}_\alpha}\left(\frac{\partial Y_\alpha}{\partial Z} + \frac{Y_\alpha}{W}\frac{\partial W}{\partial Z}\right)\right]\right)\frac{\partial T}{\partial Z}$$

$$- \frac{\partial Z}{\partial x_i}\left(\frac{\partial v_{C,i}}{\partial Z} + \frac{\partial \rho \varepsilon_i}{\partial Z}\right)\frac{\partial T}{\partial Z} + \text{HOT}_T\ , \tag{3.6a}$$

and the flame-orthogonal terms are the explicit forms of the higher-order terms. The non-zero $\mathcal{J}_5$ terms are due to the use of the mixture-fraction in accordance to Bilger *et al.* [75], given by Eq. (3.2), instead of that by Pitsch & Peters [77].

### 4.2.1 Flamelet Topology

The physical locations of nine representative conditionally averaged flamelets, three for each of the three regions: (i) near-nozzle region; (ii) flame-ignition region; and (iii) far-field region; are shown in Fig. 4.4, with flamelets {1, 4, 7}, {2, 5, 8}, and {3, 6, 9} representing the windward, sideline, and leeward sides of the configuration, respectively.



(a) Isometric view.

(b) Top view.

(c) Rear view.

(d) Side view.
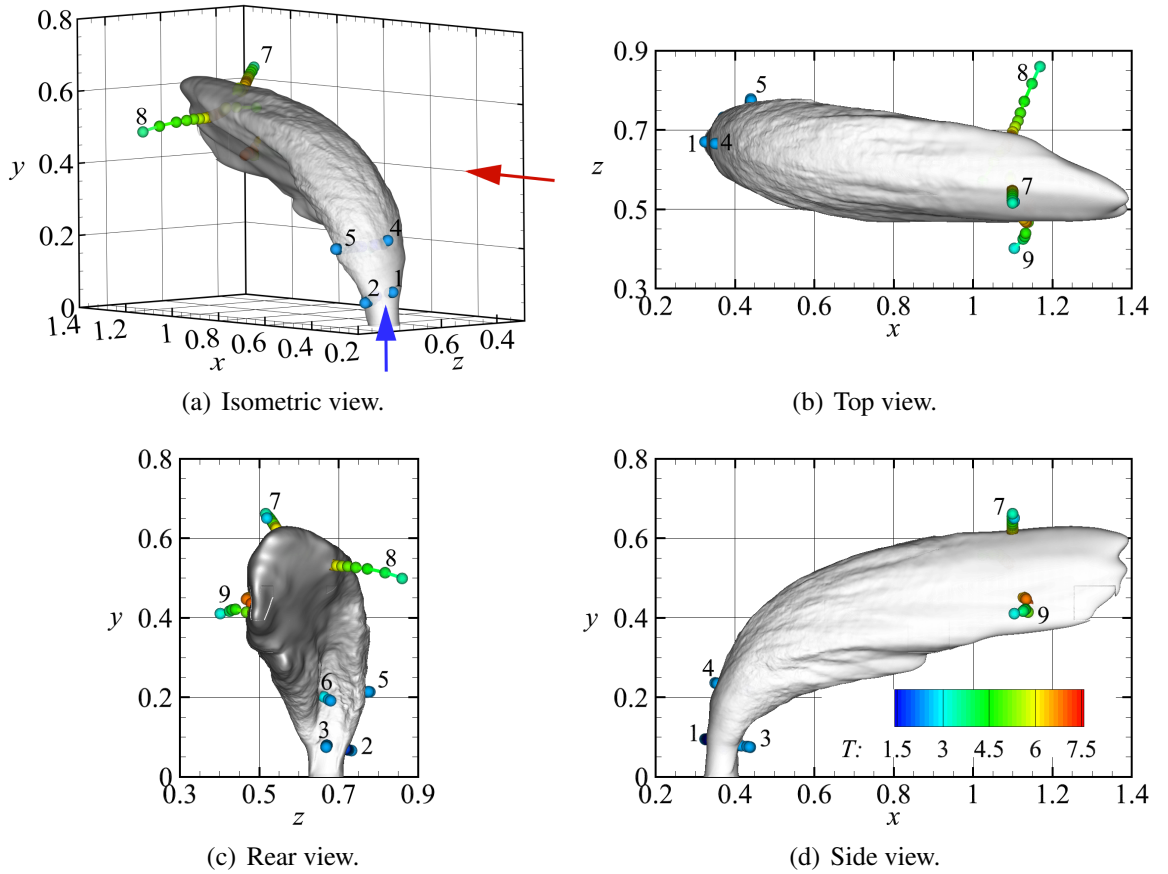
Figure 4.4: Locations of the evaluated conditionally averaged flamelets with respect to the mean stoichiometric mixture fraction iso-surface. The flamelets are colored by temperature normalized by $T^{\text{Ref}} = 300$ K. The coordinate system is normalized by $l^{\text{Ref}} = 1.5$ cm. Each flamelet is labeled by a number, ranging from 1 to 9, where flamelets 1–3 are in the jet near-field, 4–6 are in the flame-ignition region, and 7–9 are in the far-field. The two arrows denote the fuel and cross-flow injection directions.

Using the extracted flamelets, the flame structure can be characterized in terms of the flamelet topologies at the near-, ignition-, and far-field regions along the three azimuthal sides, which are illustrated in Figs. 4.5–4.7, respectively. Note that, in these figures, the notation $\xi = \{0, \ 0.25, \ 0.5\}$ has been introduced to denote the windward, sideline, and leeward sides of the JICF configuration, while $\eta$ indicates the distance from the nozzle.

Shown in the first row is the conditionally averaged flamelet topology and its intersection with the mean stoichiometric mixture-fraction iso-surface. The flamelets are colored by the temperature, which is normalized by its reference value of $300$ K, and the conditional velocity field along each flamelet is shown by vectors. A reference coordinate system is included for reference. In the second row, the conditional averaged temperature and arclength, $\xi$, of the flamelet with respect to mixture-fraction are shown. The third row consists of the mixture-fraction conditioned velocity field along the flamelet, where $\langle u_Z \rangle = \langle \boldsymbol{u} | Z \cdot \nabla Z / \|\nabla Z\| \rangle$ is the mean velocity component in the flame-aligned direction, and $\langle u_\perp \rangle = \|\langle \boldsymbol{u} | Z - u_Z \nabla Z / \|\nabla Z\| \rangle\|$ is the net velocity component orthogonal to the flamelet. The last row gives the conditional mean profiles of the scalar-dissipation rate and the most compressive and extensional strain rates. The latter two quantities correspond to the minimum and maximum eigenvalues that are evaluated from the decomposition of the strain-rate tensor, $s_{ij}$ (cf. Eq. (2.2)).

From Fig. 4.5, high shearing by the flow-field can be observed, causing all flamelets to exhibit insignificant amount of folding. Therefore, the averaged flamelet topology at this near-nozzle region has a quasi one-dimensional structure, which is consistent with the corresponding temperature and flame-length profiles. From the velocity plots, the results indicate that: (i) $u_Z$ is relatively insignificant for all azimuthal locations, suggesting that there is little flow in the flame-aligned direction; (ii) a low velocity region occurs on the fuel-lean side, which is attributed to the stagnation flow induced by the interactions of the fuel jet and the crossflow; and (iii) $u_\perp$ noticeably increases at the fuel-rich mixture, so the flame-orthogonal velocity component is mostly aligned with the bulk flow of the jet in the wall-normal direction. Interestingly, the scalar-dissipation rate and extensional strain, which is the dominant component here, exhibit a qualitatively common trend, although the maximum points of the two quantities do not usually coincide and the strain rate has a wider structure than the dissipation rate. Similar observations have been reported in a study of the effects of unsteady strain on scalar-dissipation rate [103]. In addition, the principal strain components appear to have an azimuthal dependence, in which the most extensional and most compressive strains dominate the windward and leeward sides, respectively. Such exchange in the dominance of the strain component may be due to the high shear at the windward side and strong compression due to vortices at the leeward side. Results for the

sideline location show comparable strain components. The leeward fuel-rich region at this near-nozzle location is seen to display a large compressive strain that is at least twice as strong as the dominating strain components at all other locations.

At the flame-ignition region, as shown by Fig. 4.6, little difference can be observed for all the flamelet structures than those in Fig. 4.5. For example, all flamelets still exhibit insignificant amount of bending and are distorted only by flame-aligned compression and extension. The most obvious indication of a flame-ignition is given by the rise in the maximum leeward temperature, whereas the windward and sideline locations retain the same mixing temperature profile shown in Fig. 4.5. In contrast to the flamelets in the nozzle-near region, all the flamelets in this ignition region are seen to possess a flame-aligned velocity component, $u_Z$, especially for the fuel-rich mixtures. The alignment between the flame-orthogonal velocity component, $u_\perp$, and bulk flow of the jet is sustained for the windward and leeward sides, while $u_\perp$ at the sideline location is relatively constant. The correlation between the dominant principal strain component and scalar-dissipation rate is still apparent, although the distinction between the most compressive and most extensional strains has largely diminished. The two strain components also maintain their dominance at the leeward and windward sides, respectively.

Flamelets at the far-field region, given by Fig. 4.7, are discernibly different from the earlier flamelets, exhibiting significant distortions due to folding and stretching. However, these distortions are partially attributed to an insufficient temporal sample size because the downstream region is characterized by large-scale mixing processes and hence associated with long hydrodynamic time-scales. None of the temperature distribution resembles the aforementioned mixing temperature profile, but corresponds to reacting profiles that are increasingly close to the laminar flamelet equilibrium solution from the windward to leeward sides. The reduction in the mixture-fraction range is an expected result of reactant mixing. From the velocity plots, the $u_\perp$-component is less sensitive to the azimuthal location than its $u_Z$ counterpart, with the former being approximately constant at $0.1$, while the latter decreases to zero as $\xi$ increases. The greatest difference at the far-field region is seen in the strain and dissipation rate terms, where: (i) the scalar-dissipation rate is hardly representative of its analytical Gaussian profile [9]; (ii) the principal strain components and scalar-dissipation rate are no longer correlated; and (iii) the most compressive strain component dominates all flamelets. Note that the magnitudes of the strain and dissipation rate terms are reduced by as much as three orders compared to the near-nozzle region.

In summary, this analysis showed that the flamelet structure is dominantly quasi one-dimensional, except in the downstream regions where statistical results are not fully converged. This finding is relevant for experimental investigations, suggesting that the planar
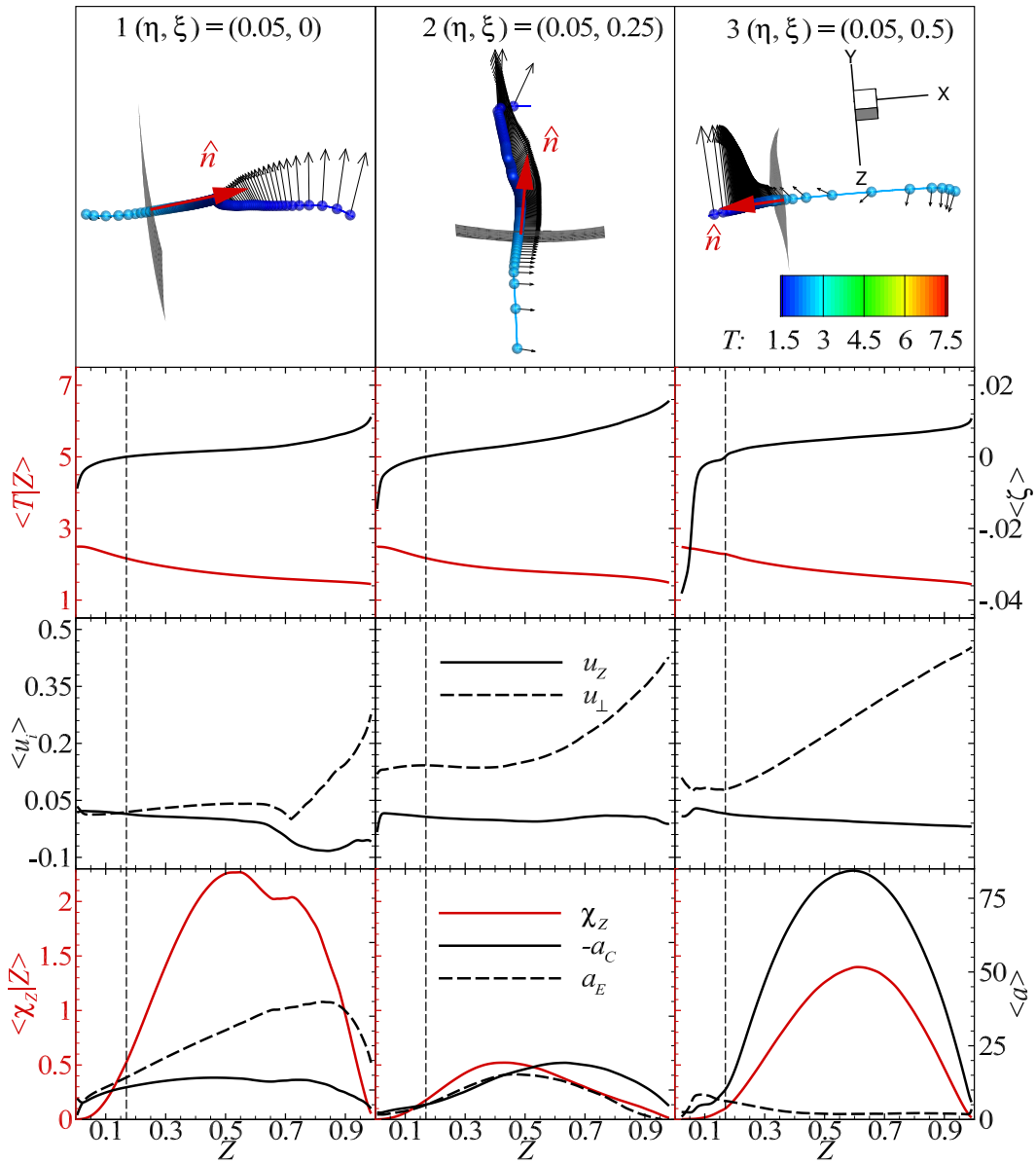
Figure 4.5: Flamelet-topology at the nozzle-near region. Velocity vectors are shown by black arrows (scaled relatively by magnitude), and the flame normal vector (pointing towards the fuel side) is denoted by $\widehat{n}$. Symbols are colored by normalized temperature, and individual flamelets are labeled following the notation in Fig. 4.4. The vertical dashed line denotes the location of the stoichiometric mixture. Conditional temperature and flame-length, velocity components, and scalar dissipation and principal strain rates are shown in the second to fourth rows and normalized by reference values of 300 K and 1.5 cm, 550 m/s, and $3.7 \times 10^4$ 1/s, respectively.
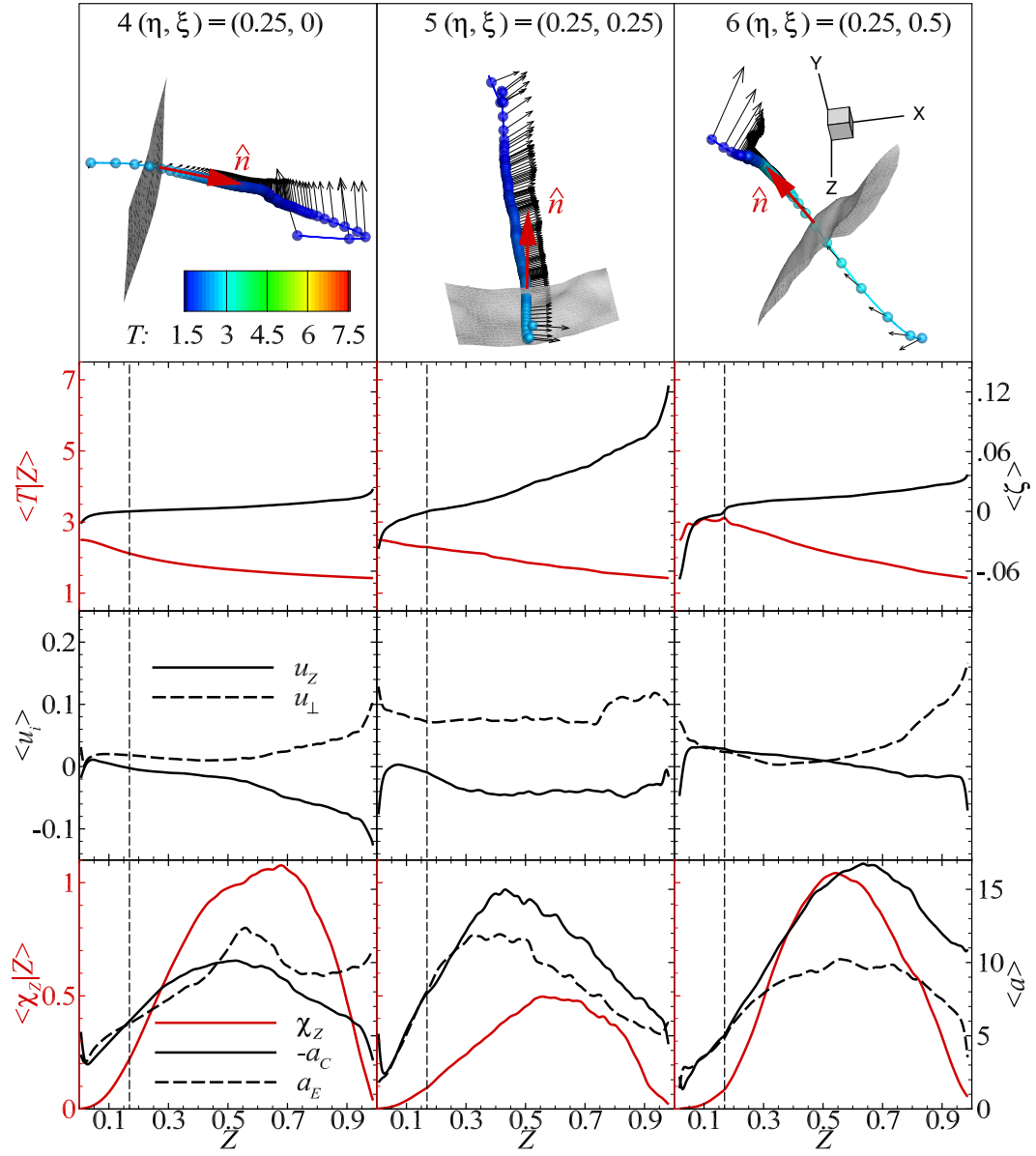
Figure 4.6: Flamelet topology at the leeward flame-ignition region. See Fig. 4.5 for description.
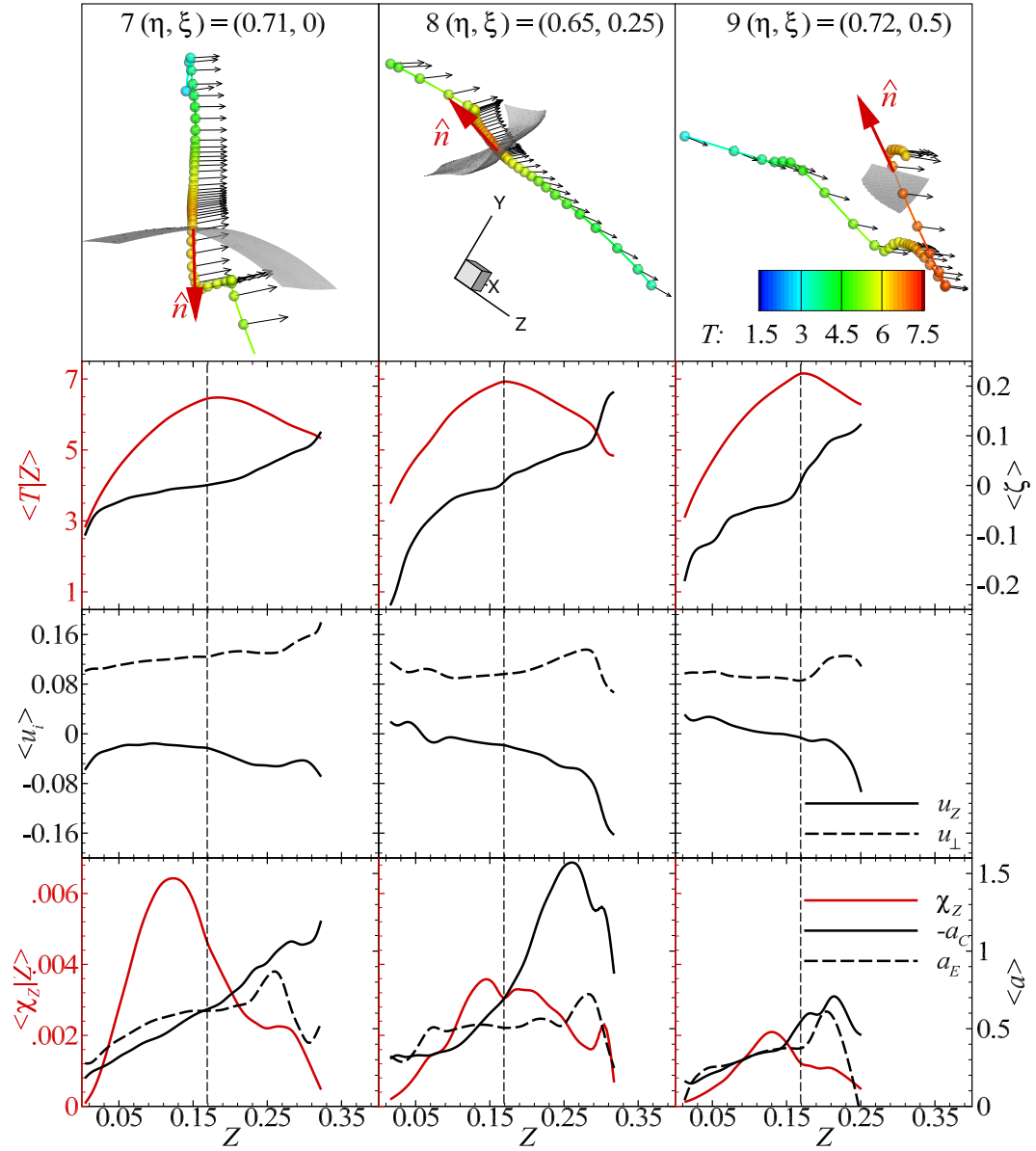
Figure 4.7: Flamelet topology at the far-field region. See Fig. 4.5 for description.

measurements that account for the alignment of the mixture-fraction field can provide valuable insights to the flame-topology. The differences in the flamelets at various regions of the flame indicate qualitatively different flame-regimes, which are characterized by different velocity and strain rate profiles and the resulting ignition scenarios, which can be represented by the flamelet formulation.

### 4.2.2 Mixture-Fraction Conditioned Data

The conditionally averaged normalized scalar-dissipation rate and temperature profiles (reference value of $3.7 \times 10^4$ 1/s and 300 K) at the three sides are given by Figs. 4.8–4.9. Most noticeable of these profiles is the difference in their flame regimes in different regions, which are characterized by different velocity and strain rate profiles, and the resulting ignition scenarios where the windward and leeward sides demonstrate the latest and earliest flame-ignition, respectively. Considering the variations in the scalar-dissipation rate and temperature, the early ignition at the leeward side, as compared to the windward and sideline sides, is attributed to a faster reduction in the dissipation rate. Interestingly, the scalar-dissipation rate profiles suggest that the flame-ignition occurs only when the stoichiometric dissipation value, $\chi_{Z,\mathrm{st}}$, falls below the laminar flamelet quenching value of approximately 4000 1/s. In addition, the comparison with the laminar profiles (thin solid line) indicates that: (i) the extracted scalar-dissipation rate profiles are generally asymmetric about $Z = 0.5$, in contrast to the quenching dissipation rate; and (ii) the far-field temperature profiles have not reached the flame-equilibrium state.



(a) Windward.  (b) Sideline.  (c) Leeward.
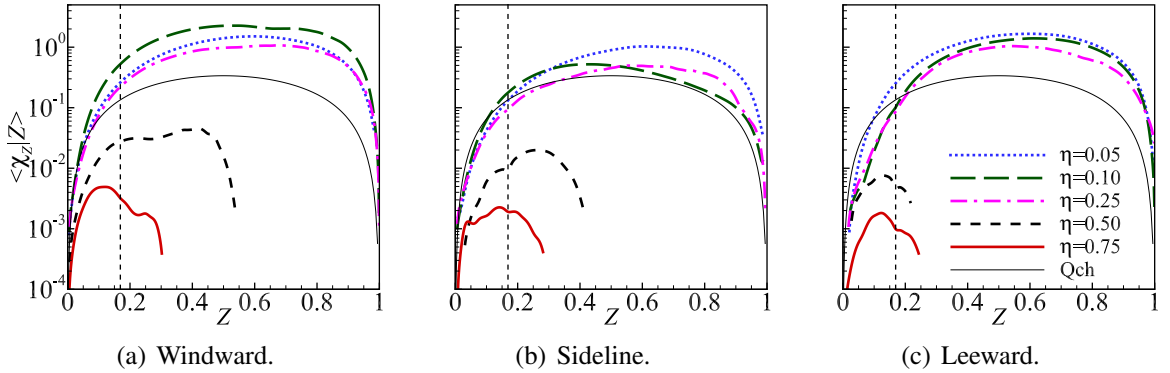
Figure 4.8:  Conditionally-averaged scalar dissipation rate profile for the three azimuthal sides and different locations along the jet-trajectory. The vertical dashed line indicates the stoichiometric mixture-fraction, and the analytic scalar dissipation rate profile [9] at laminar flamelet quenching condition (Qch) is denoted by the thin line. The results are normalized by $\chi_Z^{\mathrm{Ref}} = 3.7 \times 10^4$ 1/s.
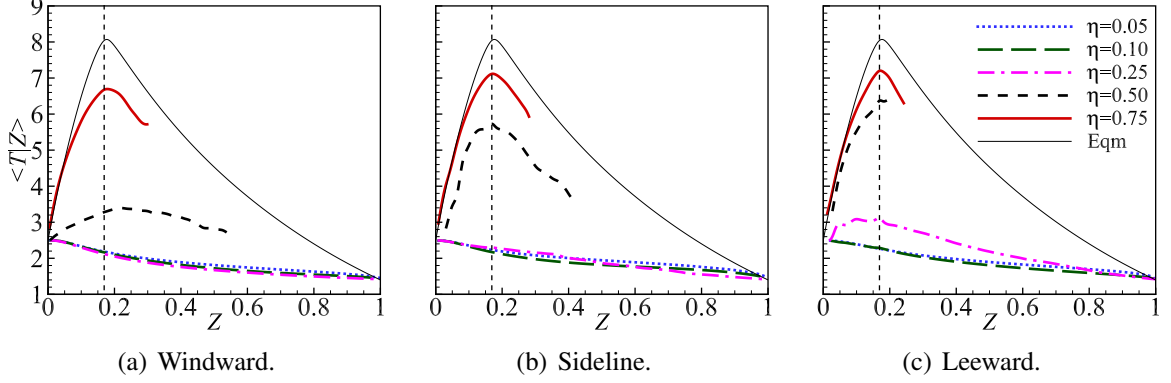
Figure 4.9: Conditionally-averaged temperature profiles for the three azimuthal sides and different locations along the jet-trajectory. The vertical dashed line indicates the stoichiometric mixture-fraction, and the laminar flamelet equilibrium solution (Eqm) is denoted by the thin line. The results are normalized by $T^{\text{Ref}} = 300$ K.

The conditionally averaged flamelet budget plots are shown in Fig. 4.10, where a negative contribution can be interpreted as a heat-sink term that delays flame-ignition. All contributions along the flame-aligned and flame-orthogonal directions are denoted by lines and symbols, respectively, in Fig. 4.10. From the budgets, the collective contribution due to curvature and lateral diffusion effects, as indicated by the $\mathcal{J}_4^\perp$ term, is observed to be negligible in this analysis, possibly due to the averaging of the information. In contrast, the temporal derivative term (dotted line), which represents the flamelet unsteady effect, is not always negligible, indicating a stronger compatibility with the unsteady flamelet models than the steady types. Also, the budget plots illustrate that the differential diffusion effect, represented by the $\mathcal{J}_5$ terms, is dominant by the flame-aligned contribution, confirming that only the consideration of the $\mathcal{J}_5^Z$ term is necessary in order to represent the effect.

Prior to flame-ignition, which initiates at the leeward side between $0.1 < \eta < 0.25$, the budget plots show similar relative significance between the various flamelet terms of the three sides, even though differences in their absolute values are apparent. Specifically, the prominent contributions are from the $\mathcal{J}_1^Z$, $\mathcal{J}_3^Z$, and $\mathcal{J}_5^Z$ terms, where the initial two terms are consistently competing against each other such that the transient heat-sinking effect is dominantly due to the last term. In physical sense, the pre-ignition dynamics are then given by the competition between the scalar mixing ($\mathcal{J}_1^Z$) and enthalpy flux due to species diffusion ($\mathcal{J}_3^Z$) and the heat-transfer from the fuel-rich mixture to the fuel-lean side by flame-aligned differential diffusion ($\mathcal{J}_5^Z$). Comparing the windward budget plots at the first three $\eta$-locations, the flamelet terms exhibit similar relative magnitudes, suggesting the existence of a consistent pattern in the non-reacting flamelet budgets.
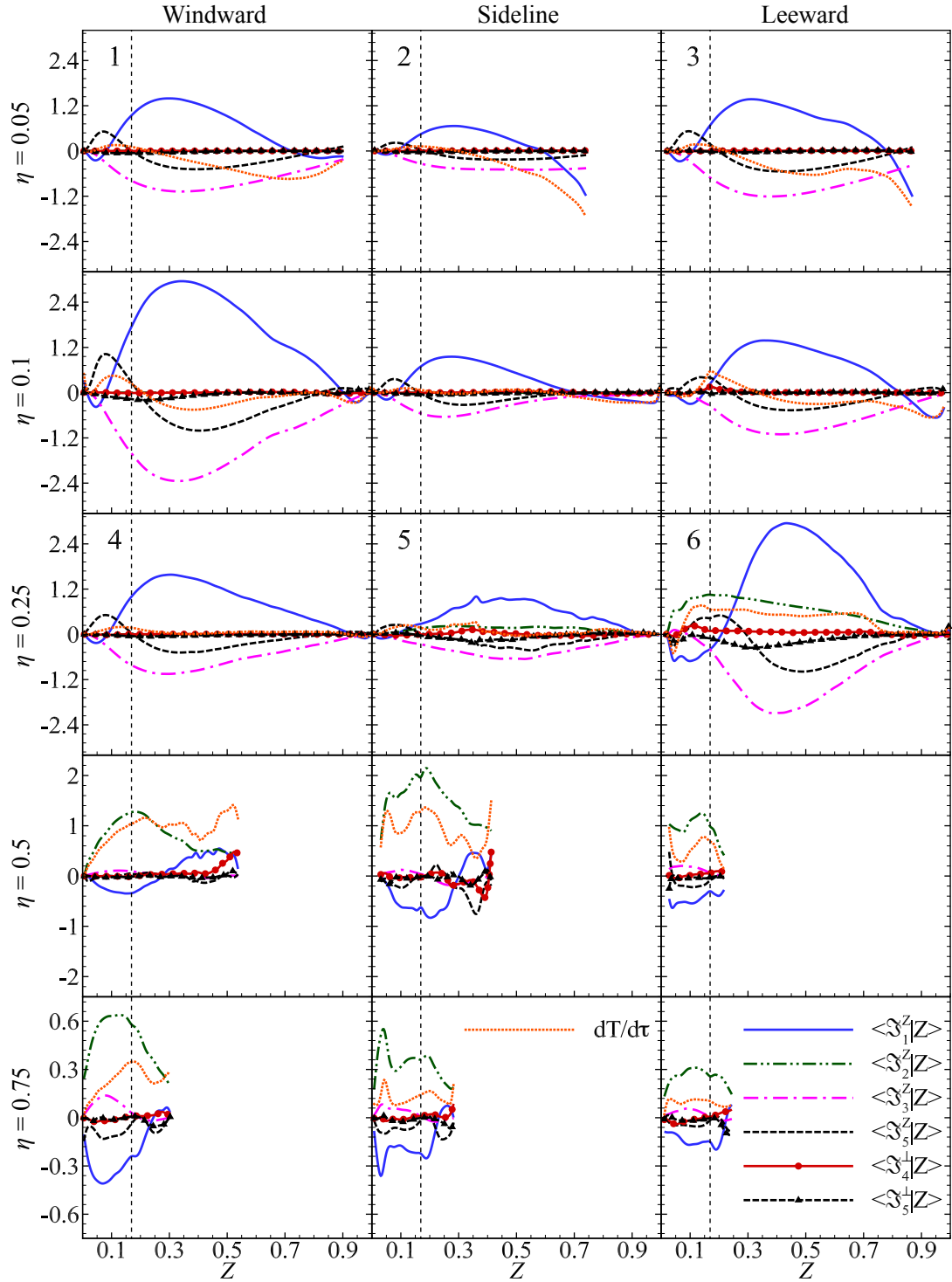
Figure 4.10: Budget-analysis of the temperature flamelet equation (4.2). Columns denote the three azimuthal positions, and rows correspond to the locations along the jet-trajectory. The flamelets with labels correspond to those shown in Fig. 4.4. The vertical dashed line indicates the location of the stoichiometric mixture-fraction. Note that all budget terms are mixture-fraction conditioned results and normalized by a reference value of $1.1 \times 10^7$ K/s.

40

Upon successful flame-ignition ($\eta > 0.5$), the major contributors become the $\mathcal{J}_1^Z$ and $\mathcal{J}_2^Z$ terms, while a decay in the other terms can be observed. Hence, the post-ignition dynamics is governed by the competition between the scalar mixing ($\mathcal{J}_1^Z$), which is now a heat-sink term, and heat-release rate ($\mathcal{J}_2^Z$), with the latter being the dominant contribution such that the overall temporal term is positive.

In summary, this study shows that the flamelet paradigm [7] remains on average valid in the JICF configuration, despite its complex flow-field. This deduction is based on the budget analysis, which shows that the flame-aligned terms are dominant contributions to the temperature flamelet equation (4.2), while the flame-orthogonal terms are on average negligible. In addition, the flame-aligned differential diffusion effect is found to be crucial and favors ignition. These findings are encouraging because they indicate that the JICF configuration may be represented by a flamelet model that accounts for non-unity Lewis number and unsteady effects.

## 4.3   Turbulent Lifted Jet Flame

The turbulent lifted jet flame configuration is schematically illustrated in Fig. 4.11, and the essential parameters of the configuration are given in Tab. 4.2. Turbulent lifted jet flames have been widely investigated due to their practical relevance to fuel-injection internal combustion engines and theoretical suitability for understanding autoignition and partial-premixing phenomena. Specifically, the stabilization mechanism of turbulent lifted jet flames has been examined extensively, with various theories proposed. These theories can be categorized based on the degree of fuel-air premixing upstream of the flame base [104–106], or on the local turbulence effect on the flame base [107, 108]. For lifted flames in a heated coflow [37, 109], autoignition was considered as an additional contribution to the flame stabilization phenomenon. Using DNS, Yoo *et al.* [96] concluded that autoignition is indeed the key mechanism for stabilization of lifted jet flames in heated coflow. The same DNS results, but at a slightly lower coflow temperature of $950$ K, are employed for the current study.

The focus of this study is on an asymptotic scaling analysis, developed by Scholtissek *et al.* [91], for the identification of different flamelet regimes that are relevant to the turbulent lifted jet flame. The analysis in the general case will distinguish three regimes, as given in Tab. 4.3, using two characteristic ratios:

$$\frac{\varepsilon}{\nu} \, , \quad \frac{\varepsilon^3}{\nu^2} \, , \tag{4.3}$$
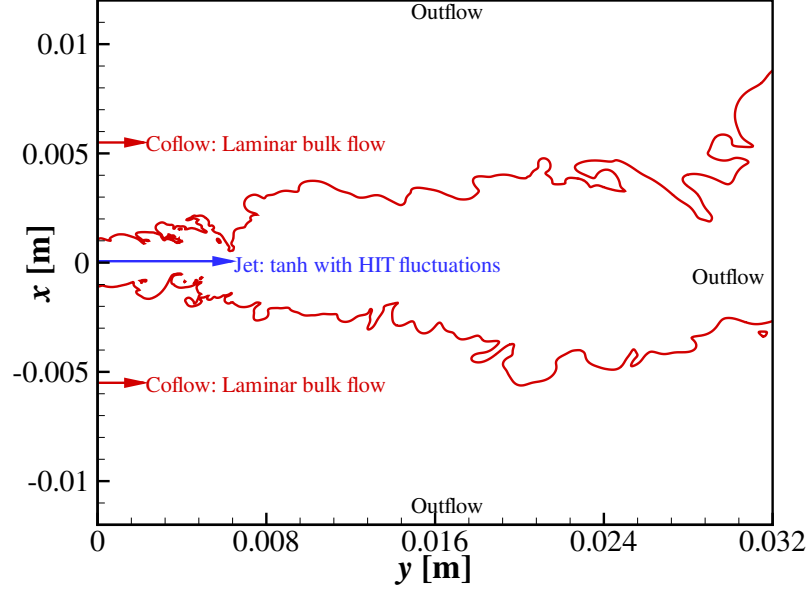
Figure 4.11: Turbulent lifted jet flame DNS configuration and traverse ($x$) and stream-wise ($y$) boundary conditions [96]; the spanwise ($z$) direction uses a periodic boundary condition. The contour line denotes the stoichiometric mixture-fraction isoline.

| Parameter | | Value |
|:---:|:---:|:---:|
| | Slot width | 2 mm |
| | Mean velocity | $[240,\ 0,\ 0]^T$ m/s |
| Jet | Composition | $Y_{H_2},\ Y_{N_2} = 0.12,\ 0.88$ |
| | Temperature | 400 K |
| | Reynolds number | 8000 |
| | Mean velocity | $[4,\ 0,\ 0]^T$ m/s |
| Coflow | Composition | $Y_{O_2},\ Y_{N_2} = 0.23,\ 0.77$ |
| | Temperature | 950 K |
| Domain size | | $24 \times 32 \times 6.3$ mm |
| Grid resolution | | $1600 \times 1372 \times 430$ |
| Chemical kinetics | | 9 species, 19 reactions [102] |
| Stoichiometric mixture-fraction | | 0.2 |
| Velocity fluctuation, $(\|u_i'\| / \|u_i\|)_{\text{Jet}}$ | | 0.091 |
| Integral length | | 0.7 mm |
| Turbulent Reynolds number, $\text{Re}_\Lambda$ | | 340 |

Table 4.2: Essential parameters of the turbulent lifted jet flame DNS by Yoo *et al.* [96].

where $\varepsilon$ and $\nu$ refer to two small parameters that scale with the reaction-zone thickness and flame curvature, respectively. The first ratio in Eq. (4.3) is related to the order of the

curvature term of Eq. (3.6b):

$$\left(\frac{1}{\text{Le}_\alpha} - 1\right)\kappa_Z\sqrt{\frac{D_Z\chi_Z}{2}}\frac{\partial Y_\alpha}{\partial Z} \sim \mathcal{O}\left(\frac{\varepsilon}{\nu}\right) \ ,$$

and has a dependence on non-unity Lewis number effects, hence does not concern the temperature flamelet equation (3.6a) since $\text{Le}_T = D_Z/D_{\text{th}} = 1$. The latter ratio represents the magnitude of the primary effect of the higher-order terms in both flamelet equations (i.e. HOT $\sim \mathcal{O}(\varepsilon^3/\nu^2)$), and will be present regardless of differential diffusion effects, but can be negligible in the asymptotic limit of a thin reaction-zone thickness [78] or configurations, for example the counterflow diffusion flame [110], where scalar diffusion occurs dominantly in the direction of the mixture-fraction gradient.

| | Regime | Limit |
|---|---|---|
| I | Classical flamelet | $\varepsilon/\nu < 1$ |
| II | Curvature-affected | $\varepsilon/\nu > 1$, $\varepsilon^3/\nu^2 < 1$ |
| III | Higher-order flamelet | $\varepsilon/\nu > 1$, $\varepsilon^3/\nu^2 > 1$ |

Table 4.3: Flamelet regimes derived from asymptotic scaling flamelet analysis [91].

These physical distinctions of the various flamelet regimes render the current turbulent lifted jet flame a suitable configuration to study, since: (i) the turbulence from the flow will distort the mixture-fraction field on fine-scale levels, inducing significant local curvatures; (ii) the use of a hydrogen/air mixture ensures that non-unity Lewis number effects are not negligible because of the difference in molecular diffusivity of the light-weighted hydrogen and the heavier nitrogen and oxygen; and (iii) the flame stabilization mechanism suggests that flamelets near the flame base cannot be isolated structures, and will influence one another in conceptually analogous manner as those of the interactive flamelet model [5]. Due to the last point, Scholtissek *et al.* [91] had addressed the higher-order flamelet regime of the current work as the multi-dimensional regime because the flamelet interactions can be interpreted as scalar diffusion in the direction orthogonal to mixture-fraction gradient.

An instantaneous planar view of the temperature field along the centerplane is shown in Fig. 4.12, along with four representative flamelets . For convention, the four flamelets will be distinguished by their stoichiometric streamwise locations $x_{\text{st}} = \{5,\ 14,\ 17,\ 27\}$ mm and labels 1–4. The regime and budget plots of the same four flamelets are illustrated by Figs. 4.13–4.14, respectively. Note that the legends of Fig. 4.14 are notations introduced

by rewriting of the flamelet equations (3.6a)–(3.6b):

$$\frac{\partial T}{\partial \tau} = \frac{\chi_Z}{2} \frac{\partial^2 T}{\partial Z^2} - \sum_\alpha \frac{1}{c_p} h_\alpha \dot{\omega}_\alpha$$

$$+ \frac{\chi_Z}{2c_p} \left( \frac{\partial c_p}{\partial Z} + \sum_\alpha \left[ \frac{c_{p,\alpha}}{\mathrm{Le}_\alpha} \left( \frac{\partial Y_\alpha}{\partial Z} + \frac{Y_\alpha}{W} \frac{\partial W}{\partial Z} \right) \right] \right) \frac{\partial T}{\partial Z}$$

$$- \frac{\partial Z}{\partial x_i} \left( \frac{\partial v_{C,i}}{\partial Z} + \frac{\partial \rho \varepsilon_i}{\partial Z} \right) \frac{\partial T}{\partial Z} + \mathrm{HOT}_T \; , \tag{3.6a}$$

$$\frac{\partial Y_\alpha}{\partial \tau} = \frac{\chi_Z}{2\mathrm{Le}_\alpha} \left( \frac{\partial^2 Y_\alpha}{\partial Z^2} + \frac{Y_\alpha}{W} \frac{\partial^2 W}{\partial Z^2} \right) + \dot{\omega}_\alpha$$

$$+ \frac{1 - \mathrm{Le}_\alpha}{4\rho \mathrm{Le}_\alpha} \left( \frac{\partial \rho \chi_Z}{\partial Z} + \frac{\chi_Z}{D_Z} \frac{\partial \rho D_Z}{\partial Z} - \frac{2\rho \chi_Z}{\mathrm{Le}_\alpha (1 - \mathrm{Le}_\alpha)} \frac{\partial \mathrm{Le}_\alpha}{\partial Z} \right) \frac{\partial Y_\alpha}{\partial Z}$$

$$+ \frac{1}{4\rho \mathrm{Le}_\alpha} \left( \frac{\partial}{\partial Z} \left[ \frac{\rho \chi_Z Y_\alpha}{W} \right] + \frac{\chi_Z}{D_Z} \frac{\partial}{\partial Z} \left[ \frac{\rho D_Z Y_\alpha}{W} \right] - \frac{2\rho \chi_Z Y_\alpha}{\mathrm{Le}_\alpha W} \frac{\partial \mathrm{Le}_\alpha}{\partial Z} \right) \frac{\partial W}{\partial Z}$$

$$- \frac{1}{\rho} \frac{\partial Z}{\partial x_i} \left( \frac{\partial \rho Y_\alpha v_{C,i}}{\partial Z} + \frac{\partial \rho \varepsilon_i}{\partial Z} \frac{\partial Y_\alpha}{\partial Z} \right)$$

$$- \frac{1}{\mathrm{Le}_\alpha} \kappa_Z \sqrt{\frac{D_Z \chi_Z}{2}} \left( (\mathrm{Le}_\alpha - 1) \frac{\partial Y_\alpha}{\partial Z} + \frac{Y_\alpha}{W} \frac{\partial W}{\partial Z} \right) + \mathrm{HOT}_\alpha \; , \tag{3.6b}$$

in the form:

$$\frac{\partial T}{\partial \tau} = ft_1 + ft_{\mathrm{source}} + (ft_2 + ft_3) + ft_C \; , \tag{4.5a}$$

$$\frac{\partial Y_\alpha}{\partial \tau} = f_{\alpha,1} + f_{\alpha,\mathrm{source}} + (f_{\alpha,2} + f_{\alpha,3} + f_{\alpha,7}) + f_{\alpha,C_3} + f_{\alpha,C_1} \; , \tag{4.5b}$$

where the correction velocity in the diffusion velocity term is not considered, the mixture-fraction is defined in accordance to Pitsch & Peters [77], and the mixture molecular weight is assumed constant. Here, the curvature and higher-order terms are differentiated from the classical terms by the subscript $(\;)_C$.

From the regime diagram in Fig. 4.13, flamelet 1 and 2 are seen to occupy only the classical and curvature-affected flamelet regimes I and II, while flamelet 3 and 4 cross over into the higher-order flamelet regime III as well. Therefore, only flamelet 3 and 4 will be expected to be affected by the higher-order $f_{\alpha,C_1}$- and $ft_C$-terms in their corresponding flamelet budgets.

Referring to the budget plots in Fig. 4.14, which have been normalized by their corresponding maximum absolute budget value, the budgets for $H_2O$- and OH-mass fraction and temperature of flamelet 2, 3, and 4 exhibit higher-order $f_{\alpha,C_1}$- and $ft_C$-terms that are comparable to the classical flamelet terms. On the other hand, the curvature-induced differ-
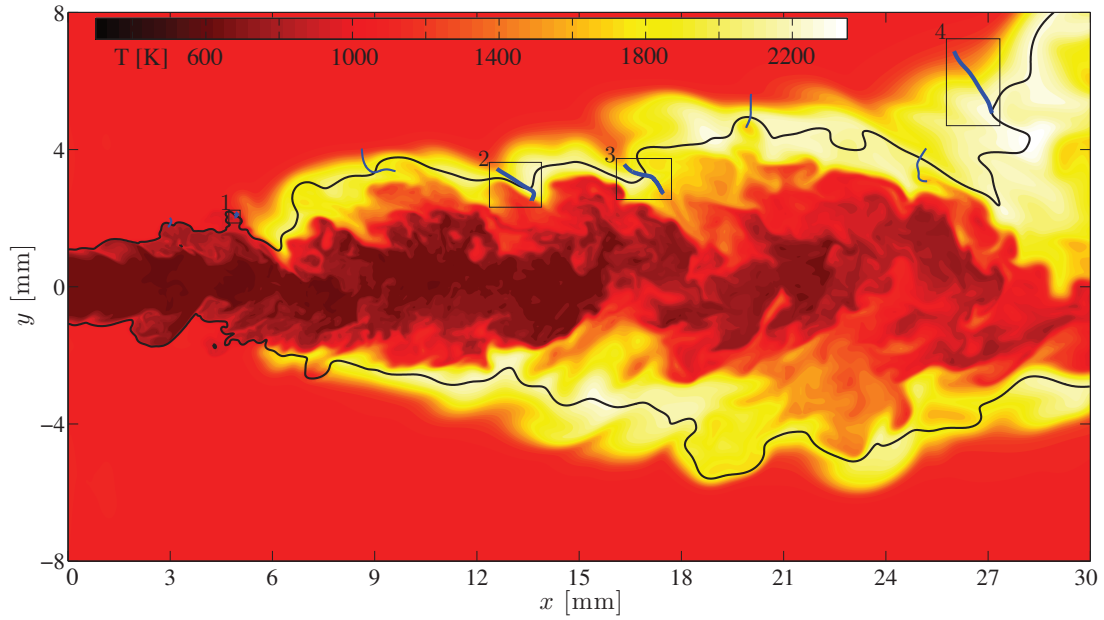
Figure 4.12: Instantaneous temperature profile along the centerplane at simulation time $t = 1.3$ ms. The blue curves represent various flamelets in physical space, while the four windows serve to single out the flamelets that were used in further analyses.
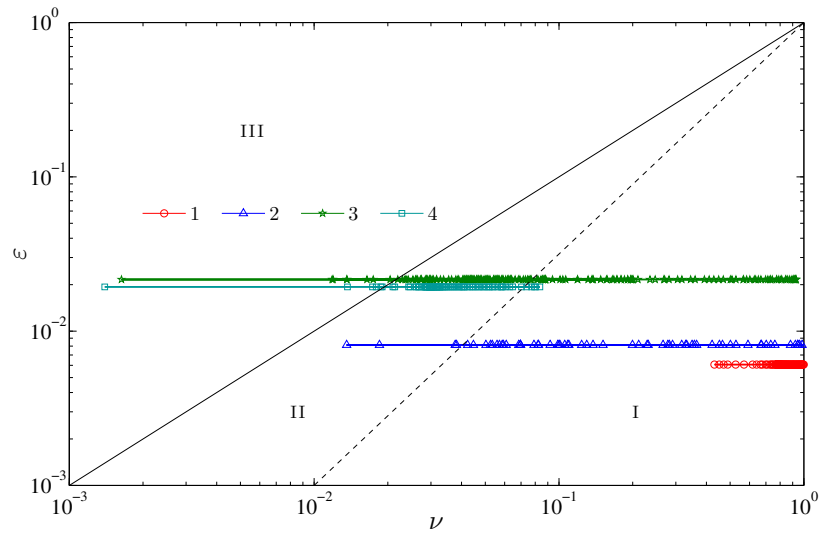


Figure 4.13: Regime diagram of the four representative flamelets shown in Fig. 4.12 The black solid and dashed lines are the boundaries between regimes I and II and regimes II and III, respectively. Note that only the points located within the interval $0.1 < Z < 0.3$ are shown, since chemical reactions typically do not occur outside of this range.
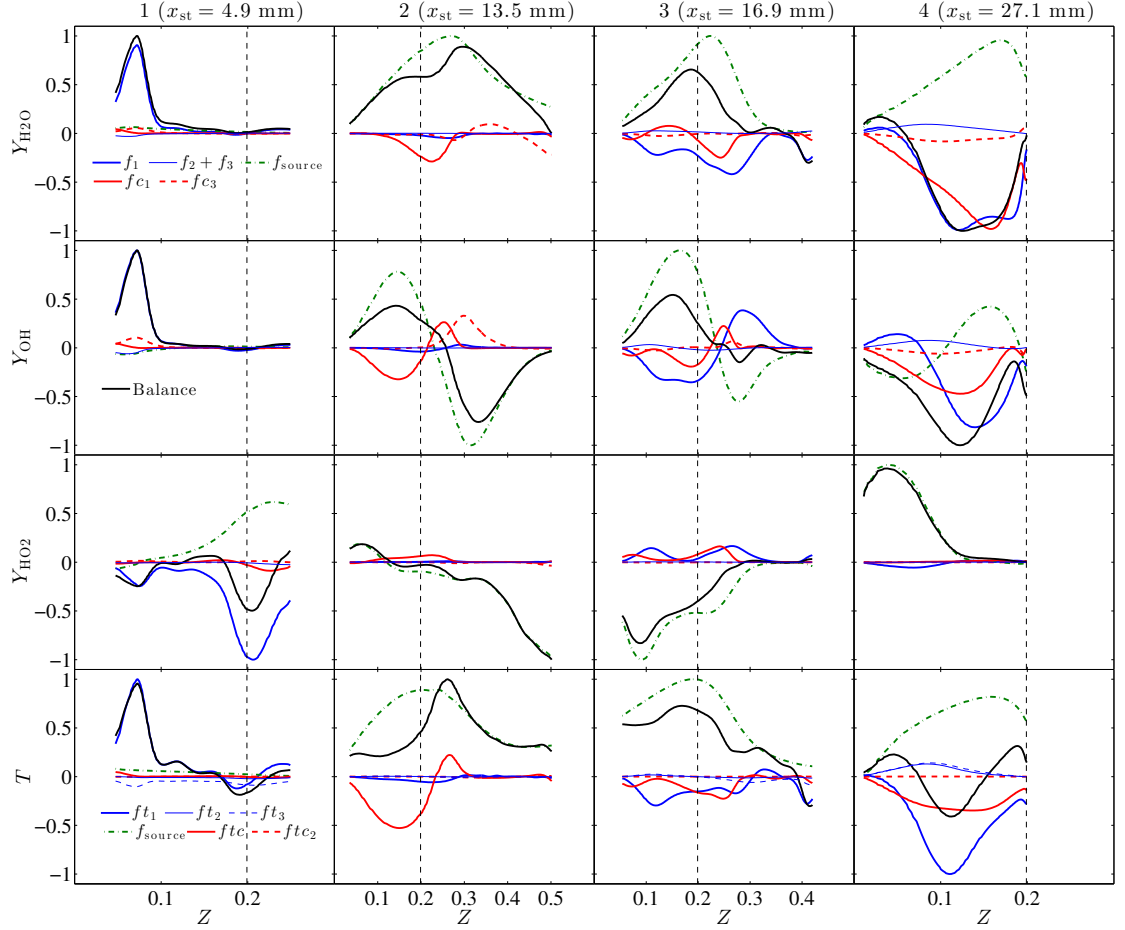
Figure 4.14: Instantaneous flamelet budgets for (top to bottom row) $Y_{\text{H2O}}$, $Y_{\text{OH}}$, $Y_{\text{HO2}}$, and $T$ of the four chosen flamelets, as shown in Fig. 4.12. The columns are arranged (left to right) in ascending order of the stoichiometric streamwise location, $x_{\text{st}}$, of the flamelets. The vertical dashed line indicates the stoichiometric mixture fraction. Note that each plot has been normalized by its corresponding maximum absolute budget value.

ential diffusion $f_{\alpha,C_3}$-term is generally of a smaller order than the major flamelet terms. The only exception is observed in the budget plots for $H_2O$- and $OH$-mass fraction of flamelet 2, where the curvature $f_{\alpha,C_3}$-term appears to be comparable to the reaction-rates. Interestingly, a competition between the curvature-induced and conventional differential diffusion terms, given by $f_{\alpha,C_3}$ and $(f_{\alpha,2} + f_{\alpha,3})$, respectively, can be discerned in the budgets for $H_2O$- and $OH$-mass fraction budgets of flamelet 4. In contrast to the other evaluated scalars, all the $HO_2$-mass fraction budgets show little dependence on the higher-order effects.

The temporal term of the flamelet equations (4.5a)–(4.5b), denoted by the black "Balance" line in the budget plots, deviates significantly from zero, suggesting that the evaluated flamelets are unsteady. This transient character can be attributed to the lifted flame con-

figuration because the unsteadiness will be expected to reduce in magnitude for anchored flame configurations.

Combining the results of the regime diagram and budget plots, the two diagnostic tools are generally consistent with each other, although there is a slight disagreement with regards to the importance of the higher-order flamelet effects along flamelet 2. However, such discrepancy is reasonable because the the regime analysis is relevant only to the order-of-magnitude of the scaling parameters, $\varepsilon$ and $\nu$, and thus susceptible to uncertainties within the same order. Hence, the fact that the regime diagram, which is based on an asymptotic scaling analysis, provides such a robust flamelet regime characterization is remarkable.

In summary, this study shows that both the higher-order and unsteady flamelet effects are significant instantaneous flamelet contributions in the turbulent lifted flame configuration. The omission of such effects, as in the case of the SLFM and FPV models, may introduce modeling errors with respect to flame structure and ignition characteristics in some regions of the flow, for instance the flame base of lifted jet flames. However, pre-processing the flamelet equations including the unsteady and higher-order terms requires modeling since these contributions, in contrary to the classical flamelet terms, are unclosed. This closure is addressed in the subsequent chapters by the higher-order flamelet model.

## 4.4 Flamelet Regime Diagram

For this investigation, we will consider the simplified species flamelet equation that contains the higher-order term, which is rewritten as:

$$\frac{\partial Y_\alpha}{\partial \tau} = (1 + \psi) \frac{\chi_Z}{2} \frac{\partial^2 Y_\alpha}{\partial Z^2} + \dot{\omega}_\alpha \, , \tag{4.6}$$

where the term $\psi$ denotes the diffusion orthogonal to the mixture-fraction gradient relative to that along the flamelet. This term is defined as:

$$\psi = \left( \frac{1}{\rho} \frac{\partial}{\partial x_i} \left[ \rho D \frac{\partial Y_\alpha}{\partial x_i} \right] - \frac{\chi_Z}{2} \frac{\partial^2 Y_\alpha}{\partial Z^2} \right) \left( \frac{\chi_Z}{2} \frac{\partial^2 Y_\alpha}{\partial Z^2} \right)^{-1} . \tag{4.7}$$

Note that Eq. (4.6) can be demonstrated to be: (i) equivalent to the classic flamelet equation [7] when $\psi \to 0$; (ii) consistent with the higher-order formulation by Scholtissek *et al.* [91]; and (iii) analogous to the interacting flamelet equation by Pitsch *et al.* [12].

The term $\psi$ of Eq. (4.7) can be approximated through a scaling argument similar to that

presented in Ref. [91]:

$$\psi \sim \mathcal{O}\left(\frac{\Delta Y_{\alpha\perp}}{(l_\perp)^2}\frac{(l_Z)^2}{\Delta Y_{\alpha Z}}\right) = \mathcal{O}\left((\Delta Z)_r\left(\frac{l_Z}{l_\perp}\right)^2\right), \tag{4.8}$$

where $(\Delta Z)_r$ is the reaction-zone thickness in mixture-fraction space [111], the subscripts $(\ )_\perp$ and $(\ )_Z$ indicate the direction orthogonal and parallel to the mixture-fraction gradient, respectively, and $l$ represents a characteristic lengthscale. Note that Eq. (4.8) is scaled with the square of a lengthscale because it considers diffusion effects. In Ref. [91], the higher-order flamelet effects were attributed to the corrugation of the mixture-fraction field, thus rendering the orthogonal length $l_\perp$ to scale at the order of the reciprocal of the mixture-fraction curvature. However, due to the multi-dimensionality of turbulent flows, the interaction of flamelets should be feasible regardless of the corrugation intensity of the mixture-fraction field. Hence, a more appropriate definition of $l_\perp$ will be based on the concept of the dissipation element [112], which is a notional turbulent structure that is characterized by the Kolmogorov lengthscale, $\eta$, for a practical range of Taylor-Reynolds numbers up to $\mathcal{O}(10^2)$. For the remaining terms of Eq. (4.8), we will follow the arguments presented in Ref. [91], giving:

$$\log(\psi) = -2\log\left(\frac{\Delta}{\delta_r}\right) + \log\left(2Z_{\mathrm{st}}\left(\frac{\Delta}{\eta}\right)^2\right). \tag{4.9}$$

where $\delta_r$ is the reaction-zone thickness. For LES with $\Delta$ of the order of the integral lengthscale the ratio $\Delta/\eta$ can be written as $\mathrm{Re}_\Lambda^{3/4}$, based on Kolmogorov's turbulent theories. The $(2Z_{\mathrm{st}})$ term arises from the estimation of $(\Delta Z)_r$ using the prescribed beta PDF for the mixture-fraction (cf. Sec. 5.3.3):

$$(\Delta Z)_r \sim \mathcal{O}\left(2Z_{\mathrm{st}}\left(1 + \frac{\widetilde{Z''^2}}{Z_{\mathrm{st}}^2}\right)^{1/2}\right), \tag{4.10}$$

where $\widetilde{Z''^2}$ is the SGS mixture-fraction variance introduced by the LES spatial-filtering. It is interesting to note that Eq. (4.10) will approach Peters' approximation for diffusion flame thickness [9] in the limit of small $\widetilde{Z''^2}$. In this case, the square-root term of Eq. (4.10) will approach unity, so $(\Delta Z)_r \to 2Z_{\mathrm{st}}$. This approximation is typically reasonable for regions away from the reactant injection point, where the flow composition is more homogeneous due to more complete mixing.

From Eq. (4.9), different regimes can be demarcated, as shown in Fig. 4.15. The broad-

est categorization is separated by the abscissa. The region above this line is characterized by significant flamelet interaction, hence invalidating the isolated flamelet model that considers only diffusion along a flamelet. For this reason, we will refer to this region as the "Multi-Dimensional Flamelet (MDFM) Regime", following Ref. [91]. Below the abscissa, a sub-section defined by $\psi \leq 2Z_{\text{st}}$ can be extracted. A flame within this sub-section will have a reaction zone that is thinner than the smallest turbulent eddy, which, in accordance to Peters [9], is the criterion for the validity of the isolated flamelet theory. Hence, we will refer to this zone as the "Peters' Regime". Recognizing that the ordinate and diagonal $\Delta = \eta$ indicate the grid resolution relative to the reaction-zone thickness and smallest turbulent length, respectively, the diagram can be divided according to the level of numerical fidelity. These divisions are addressed by the terms DNS and LES in Fig. 4.15.

Two properties of the regime diagram are distinguished. First, a mere change in grid resolution will result in only a horizontal shift, thus not altering the regime categorization. However, the fidelity of the simulation will obviously be affected, moving closer to or further from a DNS. Second, keeping the grid resolution constant, a shift away from Peters' regime can be attributed to: (i) a thicker flame (a diagonal shift at constant $\Delta/\eta$); and (ii) a higher turbulent Reynolds number (a vertical shift). Since the two effects are not mutually exclusive, a transition in the regime is more likely due to a combination of the pair.

Referring to Eq. (4.7), the regime-diagram parameter $\psi$ is related to the difference between the total diffusion and the diffusion along a flamelet. To leading-order, this difference is given by the diffusion along the mixture-fraction iso-surface [91, 113]:

$$\left( \frac{1}{\rho} \frac{\partial}{\partial x_i} \left[ \rho D \frac{\partial Y_\alpha}{\partial x_i} \right] - \frac{\chi_Z}{2} \frac{\partial^2 Y_\alpha}{\partial Z^2} \right) \sim \mathcal{O} \left( \frac{\partial^2 Y_\alpha}{\partial Z_k^2} \right) \, ,$$

which can be readily evaluated by interpolating information from the Cartesian space onto the locally orthogonal curvilinear coordinates, $\widetilde{\boldsymbol{z}} = [\widetilde{Z}, \ \widetilde{Z_2}, \ \widetilde{Z_3}]^T$, where the $\widetilde{Z_k}$ terms are defined according to Eq. (3.5). The local mixture-fraction coordinate can be extracted using the iso-surface parameterization and gradient tracing procedures described in Sec. 4.1.
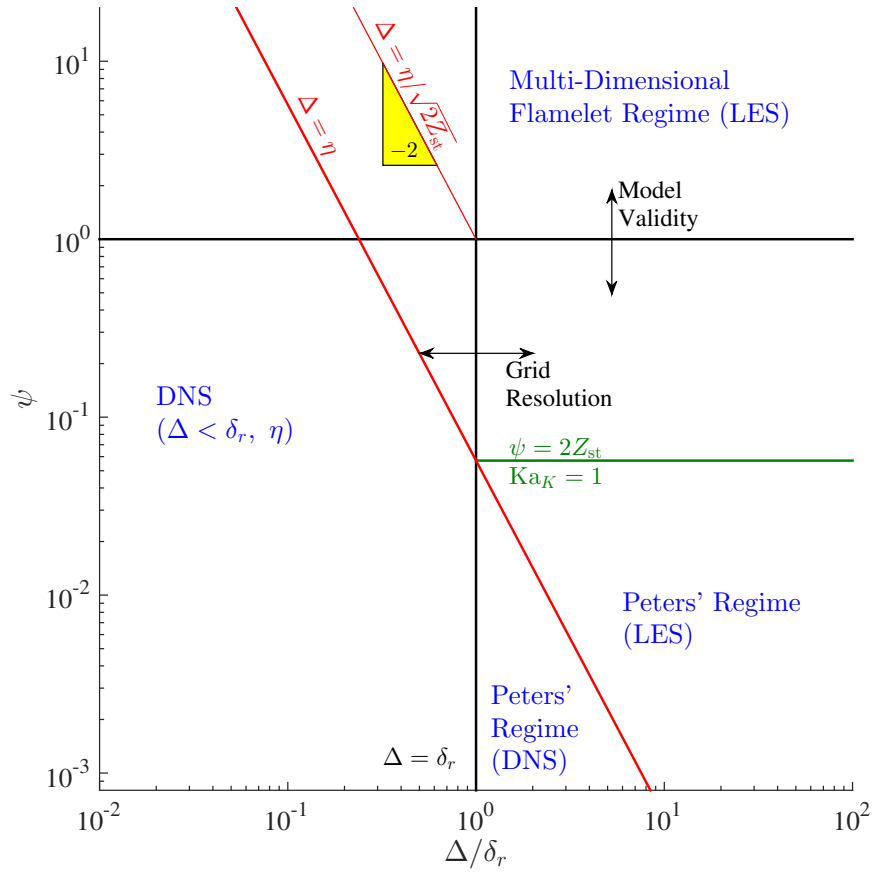
Figure 4.15: Schematic illustration of the flamelet regime diagram from Eq. (4.9).

# CHAPTER 5

# Development of Higher-Order Flamelet Model

In this chapter, the development of the higher-order flamelet model is presented, first by revisiting the laminar flamelet equation derivation from a Lagrangian perspective. Similar to the unfiltered reacting flow governing equations in Sec. 2.1, the laminar flamelet equation will be shown to possess a filtered counterpart, of which we refer to as the turbulent flamelet equations in Sec. 5.2. Similar to the filtered working equations in Sec. 2.1, the turbulent flamelet equation consists of unclosed, SGS terms that are modeled in the following section. An *a priori* analysis of the resulting model in the context of a turbulent counterflow diffusion flame is provided in the final Sec. 5.4. Note that the utilization of the simplest form of the species transport equation hereafter is without a loss of generality, because similar conclusions will be drawn for the detailed species equation (2.1d) and other thermochemical variables, such as temperature.

## 5.1   Laminar Flamelet Equations

Assuming: (i) unity Lewis number ($\text{Le}_\alpha = 1$); (ii) Fick's law ($v_{\alpha,i} = -D_Z \nabla X_\alpha / X_\alpha$); and (iii) constant mixture molecular weight; the resulting species transport equation for reacting flows, in the non-conservative form, is given by:

$$\frac{\partial Y_\alpha}{\partial t} + u_i \frac{\partial Y_\alpha}{\partial x_i} = \frac{1}{\rho} \frac{\partial}{\partial x_i} \left[ \rho D \frac{\partial Y_\alpha}{\partial x_i} \right] + \dot{\omega}_\alpha \ . \tag{5.1}$$

Similar to Lagrangian particle-tracking, we can define a material derivative with Gibson's velocity [114] along the mixture-fraction iso-surface, $u_{\text{G},i}$, by:

$$\frac{\partial Y_\alpha}{\partial \tau} = \frac{\partial Y_\alpha}{\partial t} + u_{\text{G},i} \frac{\partial Y_\alpha}{\partial x_i} \ , \tag{5.2}$$

$$u_{\text{G},i} = u_i - \frac{1}{\rho \, \|\nabla Z\|} \left( \frac{\partial}{\partial x_j} \left[ \rho D \frac{\partial Z}{\partial x_j} \right] \right) \widehat{n}_{Z,i} \ , \tag{5.3}$$

where the flamelet time $\tau$ can be interpreted as the Lagrangian residence time of Eq. (3.10) and $\widehat{n}_{Z,i}$ refers to the normalized mixture-fraction gradient. Combining Eqs. (5.1)–(5.3):

$$
\begin{aligned}
\frac{\partial Y_\alpha}{\partial \tau} &= \frac{1}{\rho}\frac{\partial}{\partial x_i}\left[\rho D\left(\left(\frac{\partial Y_\alpha}{\partial x_j}\widehat{n}_{Z,j}\right)\widehat{n}_{Z,i} + \left(\frac{\partial Y_\alpha}{\partial x_j}\widehat{n}_{Z\perp,j}\right)\widehat{n}_{Z\perp,i}\right)\right] + \dot{\omega}_\alpha \\
&\qquad\qquad - \frac{1}{\rho\,\|\nabla Z\|}\left(\frac{\partial}{\partial x_j}\left[\rho D\frac{\partial Z}{\partial x_j}\right]\right)\widehat{n}_{Z,i}\frac{\partial Y_\alpha}{\partial x_i}\,, \\
&= D\frac{\partial Z}{\partial x_i}\frac{\partial}{\partial x_i}\left[\|\nabla Z\|^{-1}\left(\frac{\partial Y_\alpha}{\partial x_j}\widehat{n}_{Z,j}\right)\right] + \dot{\omega}_\alpha \\
&\qquad\qquad\qquad + \frac{1}{\rho}\frac{\partial}{\partial x_i}\left[\rho D\left(\left(\frac{\partial Y_\alpha}{\partial x_j}\widehat{n}_{Z\perp,j}\right)\widehat{n}_{Z\perp,i}\right)\right]\,, \quad (5.4)
\end{aligned}
$$

where $Z^\perp$ denotes a local quantity constrained by the condition:

$$
\frac{\partial Z}{\partial x_i}\frac{\partial Z^\perp}{\partial x_i} = \|\nabla Z\|\,\|\nabla Z^\perp\|\,\widehat{n}_{Z,i}\widehat{n}_{Z\perp,i} = 0\,. \quad (5.5)
$$

Therefore, $\nabla Z^\perp$ is a directional vector along the local tangent plane of the mixture-fraction field, which is spanned by the $(Z_2,\ Z_3)$-coordinates of Eq. (3.5).

The physical interpretation of the $\nabla Z$ and $\nabla Z^\perp$, along with the gradient of a scalar, in this case $\nabla Y_{\mathrm{H_2O}}$, is shown in Fig. 5.1. In the figure, the scalar gradient along the stoichiometric iso-line $Z_{\mathrm{st}} = 0.5$ (solid line), which is indicated by the thin, open arrows, is seen to be opposing, but aligned with the mixture-fraction gradient. Therefore, we can expect that the last term on the RHS of Eq. (5.4) will be small relative to the first term.

Considering the following geometrical argument:

$$
\begin{aligned}
\frac{\partial Y_\alpha}{\partial Z} &= \lim_{\Delta Z \to 0}\frac{\Delta Y_\alpha}{\Delta Z} = \lim_{\|\Delta\boldsymbol{x}\| \to 0}\left(\frac{\partial Z}{\partial x_i}\|\Delta\boldsymbol{x}\|\widehat{n}_{Z,i}\right)^{-1}\left(\frac{\partial Y_\alpha}{\partial x_i}\|\Delta\boldsymbol{x}\|\widehat{n}_{Z,i}\right) \\
&= \lim_{\|\Delta\boldsymbol{x}\| \to 0}(\|\nabla Z\|\,\|\Delta\boldsymbol{x}\|)^{-1}\left(\left(\frac{\partial Y_\alpha}{\partial x_j}\widehat{n}_{Z,j}\right)\widehat{n}_{Z,i} + \left(\frac{\partial Y_\alpha}{\partial x_j}\widehat{n}_{Z\perp,j}\right)\widehat{n}_{Z\perp,i}\right)\|\Delta\boldsymbol{x}\|\widehat{n}_{Z,i} \\
&= \lim_{\|\Delta\boldsymbol{x}\| \to 0}\left(\|\nabla Z\|^{-1}\left(\frac{\partial Y_\alpha}{\partial x_j}\widehat{n}_{Z,j}\right) + \|\nabla Z\|^{-1}\left(\frac{\partial Y_\alpha}{\partial x_j}\widehat{n}_{Z\perp,j}\right)\underbrace{\widehat{n}_{Z\perp,i}\widehat{n}_{Z,i}}_{0}\right) \\
&= \|\nabla Z\|^{-1}\left(\frac{\partial Y_\alpha}{\partial x_j}\widehat{n}_{Z,j}\right)\,, \quad (5.6)
\end{aligned}
$$

where the local orthogonality of $Z$ and $Z^\perp$ is applied, we see that the first term on the RHS of Eq. (5.4) can be rewritten as:
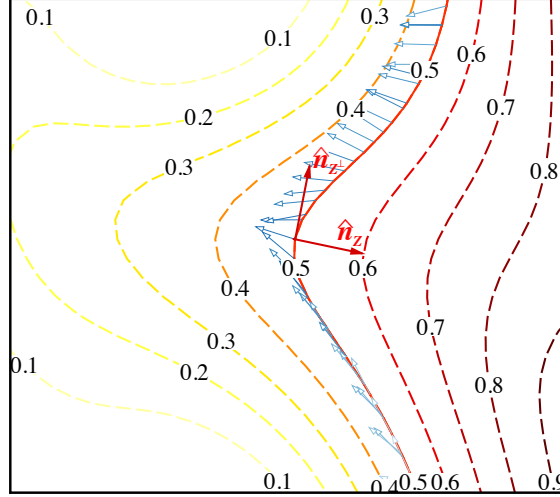
Figure 5.1: Illustration of the normalized $\nabla Z$ and $\nabla Z^\perp$ vectors (thickened, closed arrows denoted by $\widehat{n}_Z$ and $\widehat{n}_{Z\perp}$, respectively) along a stoichiometric iso-line (solid line) of $Z_{\text{st}} = 0.5$. The numerical labels denote the level of the various mixture-fraction iso-lines (dashed line), and the thin, open arrows represent the normalized $\nabla Y_{\text{H}_2\text{O}}$ along the $Z_{\text{st}}$ iso-line.

$$
D \frac{\partial Z}{\partial x_i} \frac{\partial}{\partial x_i} \left[ \|\nabla Z\|^{-1} \left( \frac{\partial Y_\alpha}{\partial x_j} \widehat{n}_{Z,j} \right) \right]
$$

$$
= D \|\nabla Z\|^2 \left( \|\nabla Z\|^{-1} \frac{\partial}{\partial x_i} \left[ \frac{\partial Y_\alpha}{\partial Z} \right] \widehat{n}_{Z,i} \right) = \frac{\chi_Z}{2} \frac{\partial^2 Y_\alpha}{\partial Z^2} , \tag{5.7}
$$

As a result, we arrive at the Lagrangian form of Eq. (5.1):

$$
\frac{\partial Y_\alpha}{\partial \tau} = \frac{\chi_Z}{2} \frac{\partial^2 Y_\alpha}{\partial Z^2} + \dot{\omega}_\alpha + \frac{1}{\rho} \frac{\partial}{\partial x_i} \left[ \rho D \frac{\partial Y_\alpha^\perp}{\partial x_i} \right] , \quad \frac{\partial Y_\alpha^\perp}{\partial x_i} = \left( \frac{\partial Y_\alpha}{\partial x_j} \widehat{n}_{Z\perp,j} \right) \widehat{n}_{Z\perp,i} , \tag{5.8}
$$

which is identical to the unsteady species flamelet equation [36, 78], except for the additional last term on the RHS. However, recognizing that the last term will reduce to zero for: (i) the case of a perfect alignment between mixture-fraction and species; or (ii) the asymptotic limit of a thin reaction-zone, Eq. (5.8) can be regarded as the higher-order form of the leading-order species flamelet equation [73]. Note that Eq. (5.8) incorporates Klimenko's notion of coordinate-invariant flamelets [13] by the use of Gibson's velocity via Eq. (5.2).

Therefore, we now have a formal physical interpretation for the derivation of flamelet equation through Crocco-type coordinate transformation [78]: The one dimensional profile from the projection of a scalar field onto a mixture-fraction gradient-trajectory will vary in accordance to the flamelet equation (5.8), where the temporal variations include the local

motion of the mixture-fraction iso-surface (i.e. Gibson's velocity) and the spatial diffusion is separated into two terms, one that aligns with the mixture-fraction gradient and the other orthogonal to the gradient (i.e. in the direction of $\widehat{n}_{Z,i}$ and $\widehat{n}_{Z\perp,i}$, respectively; cf. Fig. 5.1). In addition, if we advance the species transport equation (5.1), we are essentially solving the species flamelet equation (5.8) *with the higher-order terms accounted for*.

## 5.2  Turbulent Flamelet Equations

In the context of LES, the scalar transport equations will be solved in a spatially-filtered form. The filtered species transport equation for reacting flows that corresponds to Eq. (5.1) is given by:

$$\frac{\partial \widetilde{Y_\alpha}}{\partial t} + \widetilde{u}_i \frac{\partial \widetilde{Y_\alpha}}{\partial x_i} = \frac{1}{\overline{\rho}} \frac{\partial}{\partial x_i} \left[ \overline{\rho} \widetilde{D} \frac{\partial \widetilde{Y_\alpha}}{\partial x_i} \right] + \widetilde{\dot{\omega}_\alpha} + \frac{1}{\overline{\rho}} \frac{\partial}{\partial x_i} \left[ \overline{\rho} \left( -\widetilde{(u_i Y_\alpha)''} + \widetilde{\left( D \frac{\partial Y_\alpha}{\partial x_i} \right)''} \right) \right] \ . \quad (5.9)$$

Recalling the equivalence of transport and flamelet equations (cf. Sec. 5.1), the filter operation can similarly be applied to Eq. (5.8):

$$\widetilde{\frac{\partial Y_\alpha}{\partial \tau}} = \widetilde{\frac{\partial Y_\alpha}{\partial t}} + \widetilde{u_{\text{G},i} \frac{\partial Y_\alpha}{\partial x_i}} = \widetilde{\frac{\chi_Z}{2} \frac{\partial^2 Y_\alpha}{\partial Z^2}} + \widetilde{\dot{\omega}_\alpha} + \frac{1}{\overline{\rho}} \frac{\partial}{\partial x_i} \left[ \overline{\rho} D \widetilde{\frac{\partial Y_\alpha^\perp}{\partial x_i}} \right] \ . \quad (5.10)$$

Note that Eq. (5.10) implicitly contains unclosed SGS terms on both sides of the equation, and is not useful for modeling purposes. In order to gain more insights from Eq. (5.10), we will need to differentiate between the resolved and SGS components, denoted by $(\ )^{\text{Res}}$ and $(\ )^{\text{SGS}}$, respectively, of Gibson's velocity

$$\widetilde{u_{\text{G},i}} = (\widetilde{u_{\text{G},i}})^{\text{Res}} + (\widetilde{u_{\text{G},i}})^{\text{SGS}} \ , \quad (5.11a)$$

$$(\widetilde{u_{\text{G},i}})^{\text{Res}} = \widetilde{u}_i - \frac{1}{\overline{\rho} \left\| \nabla \widetilde{Z} \right\|} \left( \frac{\partial}{\partial x_j} \left[ \overline{\rho} \widetilde{D} \frac{\partial \widetilde{Z}}{\partial x_j} \right] \right) \widehat{n}_{\widetilde{Z},i} \ , \quad (5.11b)$$

and mixture-fraction dissipation rate:

$$\widetilde{\chi_Z} = (\widetilde{\chi_Z})^{\text{Res}} + (\widetilde{\chi_Z})^{\text{SGS}} \ , \quad (5.12a)$$

$$(\widetilde{\chi_Z})^{\text{Res}} = 2\widetilde{D} \frac{\partial \widetilde{Z}}{\partial x_i} \frac{\partial \widetilde{Z}}{\partial x_i} \ . \quad (5.12b)$$

Accordingly, the SGS components of Eqs. (5.11a) and (5.12a) are given by:

$$
(\widetilde{u_{\mathrm{G},i}})^{\mathrm{SGS}} = - \left( \overbrace{\frac{1}{\rho \left\| \nabla Z \right\|} \left( \frac{\partial}{\partial x_j} \left[ \rho D \frac{\partial Z}{\partial x_j} \right] \right) \widehat{n}_{Z,i}} \right.
$$

$$
\left. - \frac{1}{\overline{\rho} \left\| \nabla \widetilde{Z} \right\|} \left( \frac{\partial}{\partial x_j} \left[ \overline{\rho} \widetilde{D} \frac{\partial \widetilde{Z}}{\partial x_j} \right] \right) \widehat{n}_{\widetilde{Z},i} \right) , \qquad (5.13)
$$

$$
(\widetilde{\chi_Z})^{\mathrm{SGS}} = 2 \left( D \widetilde{\frac{\partial Z}{\partial x_i} \frac{\partial Z}{\partial x_i}} - \widetilde{D} \frac{\partial \widetilde{Z}}{\partial x_i} \frac{\partial \widetilde{Z}}{\partial x_i} \right) . \qquad (5.14)
$$

Rewriting Eq. (5.10) with and rearranging in accordance to the resolved and SGS terms, we will obtain:

$$
\frac{\partial \widetilde{Y_\alpha}}{\partial t} + (\widetilde{u_{\mathrm{G},i}})^{\mathrm{Res}} \frac{\partial \widetilde{Y_\alpha}}{\partial x_i} = \frac{(\widetilde{\chi_Z})^{\mathrm{Res}}}{2} \frac{\partial^2 \widetilde{Y_\alpha}}{\partial \widetilde{Z}^2} + \widetilde{\dot{\omega}_\alpha} + \frac{1}{\overline{\rho}} \frac{\partial}{\partial x_i} \left[ \overline{\rho} \widetilde{D} \frac{\partial \widetilde{Y_\alpha^\perp}}{\partial x_i} \right]
$$

$$
- \left[ (\widetilde{u_{\mathrm{G},i}})^{\mathrm{SGS}} \frac{\partial \widetilde{Y_\alpha}}{\partial x_i} + \left( \widetilde{u_{\mathrm{G},i} \frac{\partial Y_\alpha}{\partial x_i}} \right)'' \right]
$$

$$
+ \left[ \frac{(\widetilde{\chi_Z})^{\mathrm{SGS}}}{2} \frac{\partial^2 \widetilde{Y_\alpha}}{\partial \widetilde{Z}^2} + \frac{\widetilde{\chi_Z}}{2} \left( \widetilde{\frac{\partial^2 Y_\alpha}{\partial Z^2}} - \frac{\partial^2 \widetilde{Y_\alpha}}{\partial \widetilde{Z}^2} \right) + \left( \widetilde{\frac{\chi_Z}{2} \frac{\partial^2 Y_\alpha}{\partial Z^2}} \right)'' \right]
$$

$$
+ \frac{1}{\overline{\rho}} \frac{\partial}{\partial x_i} \left[ \overline{\rho} \left( \widetilde{D \frac{\partial Y_\alpha^\perp}{\partial x_i}} \right)'' \right] , \qquad (5.15)
$$

where all, except the last three terms on the RHS, are resolved. Referring to Eq. (5.8), the resolved components of the rewritten filtered species flamelet equation (5.15) clearly resemble their unfiltered counterparts.

Following the derivation in Sec. 5.1, we can define a material derivative with the *resolved* component of Gibson's velocity, which combines with Eq. (5.9) to give:

$$
\frac{\partial \widetilde{Y_\alpha}}{\partial \widetilde{\tau}} = \frac{\partial \widetilde{Y_\alpha}}{\partial t} + (\widetilde{u_{\mathrm{G},i}})^{\mathrm{Res}} \frac{\partial \widetilde{Y_\alpha}}{\partial x_i} = \frac{(\widetilde{\chi_Z})^{\mathrm{Res}}}{2} \frac{\partial^2 \widetilde{Y_\alpha}}{\partial \widetilde{Z}^2} + \widetilde{\dot{\omega}_\alpha} + \frac{1}{\overline{\rho}} \frac{\partial}{\partial x_i} \left[ \overline{\rho} \widetilde{D} \frac{\partial \widetilde{Y_\alpha^\perp}}{\partial x_i} \right]
$$

$$
+ \frac{1}{\overline{\rho}} \frac{\partial}{\partial x_i} \left[ \overline{\rho} \left( -\widetilde{(u_i Y_\alpha)}'' + \left( \widetilde{D \frac{\partial Y_\alpha}{\partial x_i}} \right)'' \right) \right] . \qquad (5.16)
$$

Comparing the two filtered species flamelet equations, we can deduce that the unclosed SGS terms of Eq. (5.15) are derived from the SGS turbulent fluxes of Eq. (5.9).

Interestingly, a Crocco-type coordinate-transformation [78] of Eq. (5.9) with respect to $\widetilde{Z}$ will also result in the filtered species flamelet equation (5.16), suggesting that the physical interpretation of flamelet equations will still apply in the filtered setting: The one dimensional profile from the projection of a *filtered* scalar field onto a *filtered* mixture-fraction gradient-trajectory will vary in accordance to the *filtered* flamelet equation (5.16), where the temporal variations include the local *resolved* motion of the *filtered* mixture-fraction iso-surface and the spatial diffusion is separated into the *filtered* mixture-fraction gradient aligned and orthogonal components. In addition, the *filtered* species transport and flamelet equations are equivalent, and unclosed SGS terms will be prevalent in both equations. We also note that the SGS turbulent fluxes of Eqs. (5.9) and (5.16) have corresponding flamelet forms that are described by the last three terms on the RHS of Eq. (5.15).

In the limit of resolution at the DNS level (i.e. all relevant spatial/temporal scales resolved), all SGS terms will approach zero, thus reducing the turbulent flamelet equation (5.15), or equivalently Eq. (5.16) to the corresponding laminar flamelet equation (5.8). Therefore, the turbulent flamelet equations are consistent with LES [14] in that they converge the filtered system to the DNS limit as resolution increases.

## 5.3 Turbulent Flamelet Model

In the following, our closure models for the turbulent flamelet equation are described. Additional numerical techniques and procedures for the turbulent flamelet model to be functional are subsequently provided.

### 5.3.1 Mixture-Fraction Conditioned Equations

In general, the spatial-filter operation on the species field can be described by a convolution of the species' conditional profile on mixture-fraction and the FDF of mixture-fraction:

$$
\begin{aligned}
\widetilde{Y_\alpha}(x_i) &= \frac{1}{\overline{\rho(x_i)}} \int \rho(x_i')Y_\alpha(x_i')\delta(Z(x_i') - \zeta)\mathcal{G}(x_i - x_i';\ \Delta_i)\mathrm{d}x_i' \\
&= \frac{1}{\overline{\rho(x_i)}} \int (Y_\alpha|\,\zeta)\,\widetilde{P}(Z = \zeta)\mathrm{d}\zeta\ ,
\end{aligned}
\tag{5.17}
$$

where $\delta(\ )$ is the fine-grained PDF, $\zeta$ is the independent variable of the mixture-fraction space, and $(\ |\,\zeta)$ and $\widetilde{P}(Z = \zeta)$ denote the mixture-fraction conditioned profile and density-weighted FDF of the mixture-fraction, respectively. Note that the filter/convolution relation (5.17) can be applied to scalar fields other than species as well.

Recalling Eq. (5.10), which can now be written in the convolution form:

$$\int \left( \frac{\partial Y_\alpha}{\partial \tau} \bigg| \zeta \right) \widetilde{P}(Z = \zeta) \, \mathrm{d}\zeta = \tag{5.18}$$

$$\int \left( \frac{\chi_Z}{2} \frac{\partial^2 Y_\alpha}{\partial Z^2} + \dot{\omega}_\alpha + \frac{1}{\rho} \frac{\partial}{\partial x_i} \left[ \rho D \frac{\partial Y_\alpha^\perp}{\partial x_i} \right] \bigg| \zeta \right) \widetilde{P}(Z = \zeta) \, \mathrm{d}\zeta \,, \tag{5.19}$$

we see that each *point* of a filtered flamelet, which satisfies the turbulent flamelet equation Eq. (5.10) or Eqs. (5.15)–(5.16), is essentially the convolution of the representative mixture-fraction conditioned laminar flamelet *profile* within the filter-cell surrounding the point.

Considering a filtered mixture-fraction field that is co-located with the filtered species profile, $\widetilde{Y_\alpha}(x_i)$, the filtered species profile can be expressed as a function of $\widetilde{Z}$:

$$\widetilde{Y_\alpha}(x_i) = \widetilde{Y_\alpha} \left( \left( \widetilde{Z}(x_i) \right)_f \right) \,, \tag{5.20}$$

where $( \ )_f$ denotes a particular path-$f$ that follows the gradient of the filtered mixture-fraction and passes through the point of evaluation. The one-dimensional filtered species distribution projected onto the path-$f$ will vary according to the turbulent flamelet equation (5.15), given that the latter is derived for filtered profiles along a gradient-trajectory.

This relation between the projected filtered species profile and the turbulent flamelet equation, which has also been pointed out in Sec. 5.2, forms the basis of the turbulent flamelet model. In essence, the model will represent the filtered reaction rate, $\widetilde{\dot{\omega}_\alpha}$, by using information along the instantaneous filtered flamelets that are present in the computational domain. Further details of this closure are provided in the subsequent sections.

## 5.3.2 Conditional Source Term Estimation

In the preceding section, the filtered species profile that is projected onto a filtered mixture-fraction gradient trajectory , as given by Eq. (5.20), is demonstrated to evolve according to the turbulent flamelet equation (5.10), or Eqs. (5.15)–(5.16). However, we should recognize that the formulation is at this point unclosed due to the presence of the filtered reaction term (i.e. $\widetilde{\dot{\omega}_\alpha}$). This observation is based on the fact that the turbulent flamelet equation is equivalent to the LES species equation (5.9), hence inherits the latter's closure problem.

In order to close the turbulent flamelet equations, we first note that convolution such as Eq. (5.17) belongs to a general class of problem that is typically referred to as the Fredholm equation of the first kind. In discrete form, such problem is described by a linear system:

$$A_{mn} x_n = b_m \,,$$

where $A$ is the matrix populated by $m$ FDF's, each spanning $n$ points on the $\zeta$-space, of the filtered mixture-fraction field, $\widetilde{Z}$, $x$ is the variable (solution) vector with $n$ components on $\zeta$-space that describe the mixture-fraction conditioned profile, $(\ )|\zeta$, and $b$ is the RHS (known) sampled from $m$ locations along a flamelet and projected onto the corresponding $\widetilde{Z}$-space. Following these notations, we can write the discrete form of Eq. (5.17) as:

$$\widetilde{P}\left(Z = \zeta_n;\ \widetilde{Z}_m\right)(Y_\alpha|\zeta_n)\,\Delta\zeta_n = \widetilde{Y_\alpha}\left(\widetilde{Z}_m\right)\ . \tag{5.21}$$

In general, the linear system described by Eq. (5.21) is ill-posed, thus requiring further treatment before it can be solved [115]. One conventional technique for this issue is to apply Tikhonov's regularization [116] to the problem, which essentially implements a low-pass filter on the system such that a representative distribution of the exact solution of Eq. (5.21) can be obtained. One caveat to this approach is its implicit assumption that the exact solution has some inherent smoothness, which is generally true for flamelet profiles (on $\zeta$- or $Z$-space). Mathematically, Tikhonov's regularization method on Eq. (5.21) is to find a regularized mixture-fraction conditioned solution, $(Y_\alpha|\zeta)_\lambda$, for the problem:

$$\min\left[\left\|\widetilde{P}\left(Z = \zeta_n;\ \widetilde{Z}_m\right)(Y_\alpha|\zeta_n)_\lambda\,\Delta\zeta_n - \widetilde{Y_\alpha}(\widetilde{Z}_m)\right\|^2\right.$$
$$\left. +\ \lambda^2\left\|I_{mn}\left((Y_\alpha|\zeta_n)_\lambda - (Y_\alpha|\zeta_n)^{\text{Guess}}\right)\right\|^2\right]\ , \tag{5.22}$$

where $\lambda$ is the regularization parameter that controls the weight given to the minimization of the regularization constraint (i.e. the second L2-norm) and $(\ )^{\text{Guess}}$ denotes a reasonable estimate of the solution. Clearly, the asymptotic choice of $\lambda \to \{0,\ \infty\}$ will drive the regularized solution to $Y_\alpha|\zeta_n$ and $(Y_\alpha|\zeta_n)^{\text{Guess}}$, respectively. Therefore, an appropriate choice of $\lambda$ is important to ensure that the problem does not: (i) reduce to the original ill-posed form; and (ii) relax to the prescribed estimate of the solution. Following Ref. [117], we will choose $\lambda = \mathrm{Tr}\left[\widetilde{P}\left(Z = \zeta_n;\ \widetilde{Z}_m\right)\Delta\zeta_n\right]/\mathrm{Tr}\left[I_{mn}\right]$, which has demonstrated good performance for the regularized inversion [118].

With the regularized solution, $(Y_\alpha|\zeta)_\lambda$, we can assume first-order conditional-moment closure:

$$(\dot\omega_\alpha\,(Y_\alpha,\ T)|\zeta_n) \approx \dot\omega_\alpha\,((Y_\alpha,\ T|\zeta_n)_\lambda)\ , \tag{5.23}$$

based on the general observations [17] that: (i) the conditional species profiles are more representative of the reactive species fields than the filtered terms, $\widetilde{Y_\alpha}$; (ii) the conditional variances are typically of smaller order than SGS species variances, $\widetilde{Y_\alpha''}$; and (iii) the mixture-fraction provides information on the stoichiometry of the mixture, which is relevant to the

chemical structure of the reacting flow. Subsequently, we can retrieve the discrete filtered reaction term with Eq. (5.21):

$$\widetilde{\dot{\omega}_\alpha}\left(\widetilde{Z}_m\right) = \widetilde{P}\left(Z = \zeta_n;\ \widetilde{Z}_m\right)(\dot{\omega}_\alpha|\zeta_n)\,\Delta\zeta_n\ , \tag{5.24}$$

thus providing a closure to the filtered reaction-rate of the turbulent flamelet model.

At this point, we should note that the described closure is similar to the conditional-source term estimation (CSE) [25] method. However, this similarity extends only to the fact that both methods share the same objective to approximate mixture-fraction conditioned information from LES filtered quantities, but the fundamental concepts that led the methods to the objective are different. First, the CSE model assumes a region in physical space, usually a cross-section of an axisymmetric configuration, where mixture-fraction conditioned profiles are homogeneous. The turbulent flamelet model also assumes homogeneous mixture-fraction conditioned profiles, but only along individual filtered flamelets, thus allowing the model to be applied to more complex configurations where a symmetry plane is hard to define. Furthermore, the choice to use mixture-fraction as the conditioning variable in CSE is based on phenomenological observations that the mixture-fraction, being intrinsically related to the mixture's stoichiometry, generally represents the flow's chemical states well. In contrast, the utilization of mixture-fraction for conditioning in the turbulent flamelet model is attributed to: (i) the equivalence of laminar flamelet and transport equations (cf. Sec. 5.1); and (ii) the existence of some mixture-fraction conditioned profiles within a filter-cell, which corresponds to a point on a filtered flamelet. Third, the CSE model often considers a doubly CMC approach, with a reaction progress indicator (e.g. scalar-dissipation rate, sensible enthalpy) as the second conditioning variable, in order to improve the model's accuracy in the presence of transient events, such as flame-extinction. The turbulent flamelet model circumvents this need for a second conditioning variable by extracting numerous filtered flamelets from different locations in the flow-field.

### 5.3.3 Presumed FDF Method

In the exchange of LES filtering with FDF convolution, such as Eq. (5.17), the knowledge of the FDF has been implied. Pope has interpreted the FDF as a distribution in composition space, weighted by the spatial-filter function, $\mathcal{G}$, within a filter-cell [87]; the FDF is equal to the PDF in the asymptotic limit of zero filter width:

$$\lim_{\Delta_i \to 0} \overline{P}(\phi = \psi) = \lim_{\Delta_i \to 0} \int \delta(\phi(x_i') - \psi)\mathcal{G}(x_i - x_i';\ \Delta_i)\mathrm{d}x_i' = P(\psi \le \phi \le \psi + \mathrm{d}\psi)/\mathrm{d}\psi\ ,$$

where $\overline{P}(\phi = \psi)$ is the FDF that does not consider density-weighting (i.e. $(\rho|\psi)\overline{P}(\phi = \psi) = \widetilde{P}(\phi = \psi)$). In principle, the FDF can be transported in the form of a conservation equation, but this approach is computationally expensive due to the need of a Monte-Carlo method and the closure problem due to molecular diffusion. Due to these computational complexities, and the fact that the present model requires only the FDF of mixture-fraction, which is a conserved, non-reacting scalar, the current work does not consider any transported FDF approach. Instead, a presumed FDF closure is implemented.

A common model for the presumed FDF of the mixture-fraction is the beta-distribution, which has been shown by *a-priori* studies [119–121] to reasonably represent non-reacting scalar distribution in most turbulent flows. However, experimental results by Tong [122] showed that the beta-distribution may not be appropriate in extreme cases, for instance strongly sheared flows. In such conditions, one may consider the direct quadrature method of moments (DQMOM) [123, 124] approach, which is an Eulerian transported PDF technique that does not rely on stochastic method and has demonstrated potential in transporting FDF practically in the LES framework.

The beta distribution for mixture-fraction is parameterized by its first two moments in a filter-cell, namely the filtered mixture-fraction, $\widetilde{Z}$, and the SGS mixture-fraction variance, $\widetilde{Z''^2} = \widetilde{Z^2} - \widetilde{Z}^2$. For a given interval $Z \in [\zeta^-, \zeta^+]$, the beta distribution is written as:

$$\beta\left(\zeta; \widetilde{Z}, \widetilde{Z''^2}\right) = \frac{\Gamma(a+b)}{\Gamma(a)\Gamma(b)} \left(\zeta - \zeta^-\right)^{a-1} \left(\zeta^+ - \zeta\right)^{b-1} \left(\zeta^+ - \zeta^-\right)^{1-a-b} , \qquad (5.25)$$

where $\Gamma(\ )$ denotes the gamma function and

$$a = \frac{\widetilde{Z} - \zeta^-}{\zeta^+ - \zeta-}\gamma , \quad b = \frac{\zeta^+ - \widetilde{Z}}{\zeta^+ - \zeta-}\gamma , \quad \gamma = \frac{\left(\widetilde{Z} - \zeta^-\right)\left(\zeta^+ - \widetilde{Z}\right)}{\widetilde{Z''^2}} - 1 . \qquad (5.26)$$

Clearly, the use of the beta distribution will require the solutions of $\widetilde{Z}$ and $\widetilde{Z''^2}$. The LES transport equation for $\widetilde{Z}$ has been given as:

$$\frac{\partial \overline{\rho}\widetilde{Z}}{\partial t} + \frac{\partial \overline{\rho}\widetilde{Z}\widetilde{u}_i}{\partial x_i} = \frac{\partial}{\partial x_i}\left[\overline{\rho}\left(\widetilde{D_Z} + \widetilde{D_t}\right)\frac{\partial \widetilde{Z}}{\partial x_i}\right] , \qquad (3.23a)$$

while the SGS mixture-fraction variance can be obtained from the following filtered trans-

port equation:

$$\frac{\partial \overline{\rho} \widetilde{Z''^2}}{\partial t} + \frac{\partial \overline{\rho} \widetilde{u_i} \widetilde{Z''^2}}{\partial x_i} = \frac{\partial}{\partial x_i} \left[ \overline{\rho} \widetilde{D} \frac{\partial \widetilde{Z''^2}}{\partial x_i} \right] - 2\overline{\rho} \widetilde{(u_i Z)''} \frac{\partial \widetilde{Z}}{\partial x_i} - \overline{\rho} \left( \widetilde{\chi_Z} \right)^{\text{SGS}}$$

$$- \frac{\partial}{\partial x_i} \left[ \overline{\rho} \left( \left( \widetilde{u_i Z^2} - \widetilde{u_i Z} \widetilde{Z} - \widetilde{(u_i Z)''} \widetilde{Z} \right) - \widetilde{u_i} \widetilde{Z''^2} \right) \right]$$

$$+ \frac{\partial}{\partial x_i} \left[ \overline{\rho} \widetilde{\left( D \frac{\partial Z^2}{\partial x_i} \right)''} \right] - 2\widetilde{Z} \frac{\partial}{\partial x_i} \left[ \overline{\rho} \widetilde{\left( D \frac{\partial Z}{\partial x_i} \right)''} \right] , \qquad (5.27)$$

where the second and third terms on the RHS are the production and dissipation terms, respectively, the fourth term corresponds to transport by turbulent motions, and the last two terms are related to SGS molecular diffusion; further modeling is required to close these specific terms. Following Poinsot & Veynante [62], the production and turbulent transport terms will be modeled by a gradient transport assumption:

$$\widetilde{(u_i Z)''} = -\widetilde{D_t} \frac{\partial \widetilde{Z}}{\partial x_i} , \quad \left( \left( \widetilde{u_i Z^2} - \widetilde{u_i Z} \widetilde{Z} - \widetilde{(u_i Z)''} \widetilde{Z} \right) - \widetilde{u_i} \widetilde{Z''^2} \right) = -\widetilde{D_t} \frac{\partial \widetilde{Z''^2}}{\partial x_i} ,$$

with $\widetilde{D_t}$ is determined from a dynamic approach (see Sec. 2.3.2). Using spectral arguments [35], the dissipation term can be modeled as:

$$(\widetilde{\chi_Z})^{\text{SGS}} = \frac{\mathcal{C}_\varepsilon \mathcal{C}_{\chi_Z} \text{Sc}_t}{\mathcal{C}_u} \frac{\widetilde{D_t}}{\Delta^2} \widetilde{Z''^2} ,$$

where $\mathcal{C}_\varepsilon / \mathcal{C}_u$ and $\mathcal{C}_{\chi_Z}$ are chosen as $\pi^2$ and 2.25, respectively, and $\text{Sc}_t = 0.4$ [34] is the turbulent Schmidt number. Finally, based on the general observation of negligible molecular diffusion relative to turbulent transport, all SGS molecular diffusion effects are omitted, thus giving the closed form of the SGS mixture-fraction variance transport equation as:

$$\frac{\partial \overline{\rho} \widetilde{Z''^2}}{\partial t} + \frac{\partial \overline{\rho} \widetilde{u_i} \widetilde{Z''^2}}{\partial x_i} = \frac{\partial}{\partial x_i} \left[ \overline{\rho} \left( \widetilde{D} + \widetilde{D_t} \right) \frac{\partial \widetilde{Z''^2}}{\partial x_i} \right] + 2\overline{\rho} \widetilde{D_t} \frac{\partial \widetilde{Z}}{\partial x_i} \frac{\partial \widetilde{Z}}{\partial x_i}$$

$$- \frac{\mathcal{C}_\varepsilon \mathcal{C}_{\chi_Z} \text{Sc}_t}{\mathcal{C}_u} \frac{\widetilde{D_t}}{\Delta^2} \widetilde{Z''^2} . \qquad (5.28)$$

### 5.3.4 Adaptive Inverse-Distance Weighting

One inconvenience of using filtered flamelet information to predict the reaction in a LES is the need to redistribute the filtered reaction-rate from the filtered flamelet space to Cartesian space. This requirement arises from the fact that the reconstructed reaction term, as

shown in Eq. (5.24), co-locates with individual flamelets, instead of the three-dimensional coordinate system. However, if the connections between adjacent flamelet points via the filtered mixture-fraction gradient are disregarded, the space covered by the extracted flamelets can be considered as a set of sampled locations. Therefore, the redistribution of filtered reaction-rate information can be accomplished by a spatial-interpolation scheme. Borrowing knowledge from the field of geoscience, the common tools for such a task are the deterministic inverse-distance weighting (IDW) method [125] or the geostatistical kriging approach [126]. To this end, we employed the adaptive IDW (AIDW) interpolation technique by Lu & Wong [127], which circumvents the lack of consideration of spatial variability by the classic IDW method, while not introducing as much computationally complexities as kriging does.

The AIDW method retains the fundamental assumptions of IDW: (i) Tobler's first law of geography [128]: "everything is related to everything else, but near things are more related than distant things" holds true for the sampled dataset. (ii) The data's probabilistic distribution is not needed for the spatial-interpolation. As a result, the spatial-interpolation can be expressed as:

$$\widetilde{\dot{\omega}_\alpha}\left(x_i\right) = \sum_{p=1}^{N_p} \left[ \frac{\|x_i - x_i^p\|^{-\xi}}{\sum_{p=1}^{N_p} \|x_i - x_i^p\|^{-\xi}} \widetilde{\dot{\omega}_\alpha}\left(x_i^p\right) \right] , \qquad (5.29)$$

where $\xi$ is the interpolation exponent and each $x_i^p$ corresponds to a point in space occupied by one flamelet. Clearly, the formulation stated in Eq. (5.29) will induce a so-called distance-decay effect that will bias against locations that are far from the sampled points, hence the name inverse-distance weighting. Interestingly, the two asymptotic limits of the exponent $\xi$ at $0$ and $\infty$ will automatically reduce the spatial-interpolation method to the sample-averaging (across all $N_p$ samples) and nearest-neighbor schemes, respectively.

As aforementioned, the classic IDW method usually lacks spatial variability consideration because it prescribes and applies the interpolation exponent uniformly across the domain-of-interest, thus fixing the distance-decay relation (5.29). The general idea behind the AIDW approach is to introduce variability in the distance-decay effect by prescribing the function, instead of the value, of the exponent, $\xi$, in accordance to the neighborhood point pattern. Specifically, the AIDW technique will emphasize on the sample-averaging scheme ($\xi \to 0$) when the point-of-evaluation at $x_i$ lies in a region with highly clustered samples, and give weight to the nearest-neighbor scheme ($\xi \to \infty$) if the point-of-evaluation resides in an area where the samples are relatively dispersed. In order to quantify the neighborhood point pattern so the appropriate scheme can be selected, the

AIDW method considers the nearest-neighbor statistic, $r$:

$$r(x_i) = \left( \left( \frac{4\pi\rho_N}{3} \right)^{-1/3} \Gamma \left( \frac{4}{3} \right) \right)^{-1} \frac{\sum_{p=1}^{N_q} \text{sort}^+ \left[ \| x_i - x_i^p \| \right]}{N_q} , \qquad (5.30)$$

where $\rho_N$ is the number density given by the ratio of $N_V$ points that defines the study region to the region's volume $V$, and $\text{sort}^+[\,]$ indicates that the set of $\| x_i - x_i^p \|$ is sorted in ascending order. The coefficient on the RHS of Eq. (5.30) corresponds to the expected nearest-neighbor distance for a random three-dimensional pattern, while the fraction refers to the observed average nearest-neighbor distance of the $N_q$ *nearest* samples. Note that the sorting function is critical for an efficient estimation of $r$ because it allows for $N_q \leq N_p$ (i.e. a subset of the total $N_p$ samples), thus limiting the number of evaluations of Eq. (5.30) to $(N_V \times N_q)$ times.

In order to invoke some degree of uncertainty in the method, fuzzy logic is implemented to map $r$ to the interpolation exponent, $\xi$. Following Ref. [127], we define the fuzzy set by a triangular membership function with five categories, as shown in Fig. 5.2. In doing so, the determination $\xi$ is divided into two steps:

1. Use $r$ to evaluate the weights ($w^{\pm}$) of the relevant upper/lower categories, as given by the ordinate.

2. Compute $\xi$ by the sum: $w^+ \xi^+ + w^- \xi^-$, where $\xi^{\pm}$ are the prescribed values of the relevant upper/lower categories.

For example, if $(r - r_{\min})/(r_{\max} - r_{\min}) = 0.34$, as indicated by the vertical line in Fig. 5.2, then the corresponding weights will be $w^+ = 0.2$ and $w^- = 0.8$, as shown by the horizontal lines, so $\xi = 0.2(1) + 0.8(0.5) = 0.6$. After the interpolation exponent has been computed for all the domain points, the spatial-interpolation can be performed with Eq. (5.29), with $\xi$ now a function of $x_i$ instead of a constant value as in the case of the IDW method.

While relatively robust, spatial-interpolation using the AIDW technique was found to return undesirably noisy profiles of chemical source terms. These noisy outputs are attributed to the locality of chemical reactions, thus allowing only samples that are extremely close by (i.e. a stringent upper limit on $N_q$) in order for the results to be smooth as they should be. To circumvent this issue, the spatial-interpolation is currently applied on a composition space, consisting of the mixture-fraction and its SGS variance, $\widetilde{Z}$ and $\widetilde{Z''^2}$, and temperature, $\widetilde{T}$. This switch of the interpolation space is possible because all three variables are transported fields that exist at every $x_i$-location (i.e. $\widetilde{\phi} = \widetilde{\phi}(x_i)$). For this reason, we will not differentiate between the space in which the AIDW interpolation scheme is performed, and simply express the interpolation in terms of $x_i$ wherever applicable. Note
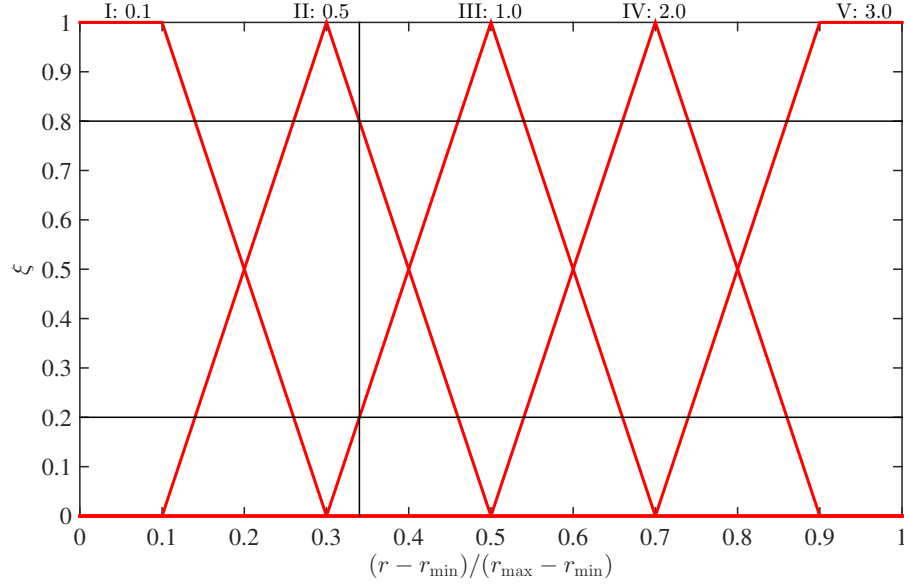
Figure 5.2: Fuzzy set as described by triangular membership function with five categories for AIDW interpolation technique [127].

that the current composition space interpolation can be interpreted as a *dynamic* FPV tabulation, with temperature being the progress-variable and in contrast to the conventional FPV model in which the tabulation is static and done *a-priori*.

### 5.3.5   Model Implementation Procedure

Having established the theories and components of the turbulent flamelet model, we will now summarize the implementation procedure of the model, which will be performed for each global time-step iteration.

**Step 1:** Compute the filtered mixture-fraction gradient, $\nabla \widetilde{Z}$, at all $N_V$ domain points.

**Step 2:** Choose $N_f$ points $(N_f \leq N_V)$ at which the tracing of $N_f$ flamelets will begin; a sensible choice should consider the stoichiometric mixture-fraction isosurface, $Z_{\mathrm{st}}$, or its vicinity.

**Step 3:** Construct the $N_f$ flamelets by tracing in the positive and negative direction of $\nabla \widetilde{Z}$. This tracing step will terminate at either a stationary point of the filtered mixture-fraction profile, or the domain boundary faces. To this end, an Eulerian pseudo-time-stepping method is utilized for efficient extraction of the flamelet paths.

Adjacent points along each flamelet will be separated by a defined bin-width in the filtered mixture-fraction space, $\Delta \widetilde{Z} = 1/N_b$, where $N_b$ is the user-defined *maximum* number of bins per flamelet. Note that the flamelets may not have an equal number of *occupied* bins, since the turbulent flow should affect each flamelet differently. Hence, the total of $N_p$ flamelet points will lie within the range $N_f \leq N_p \leq (N_f \times N_b)$, where the lower and upper bounds of the inequality correspond to the cases where all flamelets have only 1 or all $N_b$ bins occupied, respectively.

**Step 4:** Populate the $N_p$ flamelet points with filtered information relevant to the CSE method (cf. Sec. 5.3.2), including density, mixture-fraction and its SGS variance, species, and temperature. Currently, a tri-linear interpolation scheme is used for this step, and the benefits of higher-order interpolation schemes are worth exploring.

**Step 5:** Evaluate the mixture-fraction FDF for all $N_p$ flamelet points, using the presumed FDF method described in Sec. 5.3.3. One caveat to this step is the implicit condition that the number of bins in the $\zeta$-space, $N_{n,f}$ has to be less than or equal to the number of *occupied* bins of each flamelet, $N_{m,f}$:

$$N_{n,f} \leq N_{m,f} \, , \tag{5.31}$$

where the notations of $m$ and $n$ corresponds to that of Eqs. (5.21) and (5.24), while $f$ indicates that the stated bin numbers have a dependence on the flamelet being evaluated. In other words, the regularized matrix inversion, similar to the least square method, is only applicable for over-determined ($N_{n,f} < N_{m,f}$) or consistent ($N_{n,f} = N_{m,f}$) systems. For simplicity, a consistent linear system is always enforced by equating $N_{n,f}$ to $N_{m,f}$. In the case where $N_{m,f} = N_{n,f} = 1$, the inversion will be replaced by the assignment: $\phi\left(\zeta_n\right) = \widetilde{\phi}\left(\widetilde{Z}_m\right)$.

**Step 6:** Perform the regularized inversion as described by Eq. (5.22), using the filtered flamelet profile as the estimate of the solution (i.e. $(\phi|\zeta)^{\text{Guess}} = \widetilde{\phi}\left(\widetilde{Z}\right)$). If a consistent linear system is not enforced (i.e. $N_{n,f} < N_{m,f}$), an extra interpolation step will be needed to reduce the $(N_{m,f} \times 1)$ $\widetilde{\phi}\left(\widetilde{Z}\right)$-array to a $(N_{n,f} \times 1)$ array.

**Step 7:** Compute the mixture-fraction conditioned reaction-rate, $\dot{\omega}_\phi|\zeta$, using the converged conditional thermochemical profiles from the previous step. Currently, the first-order CMC, given by Eq. (5.23), is used for this calculation. Next, convolve the conditional reaction-rate with its corresponding mixture-fraction FDF from Step 5 in accordance to Eq. (5.24), thus obtaining the filtered reaction-rate, $\widetilde{\dot{\omega}_\phi}$. This step

will be performed for all $N_f$ flamelets, so $\dot{\omega}_\phi|\zeta$ and $\widetilde{\dot{\omega}_\phi}$ will be one-dimensional arrays with $N_{n,f}$ and $N_{m,f}$ entities, respectively.

**Step 8:** Distribute $\widetilde{\dot{\omega}_\phi}$, which at this point correspond only to the physical space occupied by the filtered flamelets, to the three-dimensional space using the AIDW approach of Sec. 5.3.4. Since the AIDW method disregards the relation between adjacent flamelet points via $\nabla\widetilde{Z}$, $\widetilde{\dot{\omega}_\phi}$ and their corresponding spatial locations $(x_i^p)$ can be gathered into a set of $N_p$ samples.

Subsequently, the AIDW interpolation weights for each of the $N_V$ domain points $(x_i)$ can be evaluated by sorting the $N_p$ samples in ascending order of $\|x_i - x_i^p\|$ and using the first $N_q \leq N_p$ samples of the sorted list. Without intensive parametric analyses, $N_q = 40$ is currently chosen based on its observed balance in solver efficiency and model accuracy.

Since the combustion model is developed with a consideration of the high-performance computing (HPC) architecture, the described implementation procedure is applicable to both serial- and parallel-processing simulations. For the latter case, a program interface that enables process communication will be necessary for Steps 1, 3–4, and 8. In addition, a performance gain in the model may be possible with an optimatization of the parallel-process workload, but is not pursued in this work.

Admittedly, the model implementation is not trivial and incurs approximately 14 times more computational overhead as compared to the standard FPV model and 8 times more than the laminar approximation model. However, this price is deemed reasonable in light of the advantages provided by the turbulent flamelet model, as will be demonstrated in the following study. In particular, the flamelet extraction step of the model (i.e. Step 3) will, by virtue of the equivalence of flamelet and transport equations (see Secs. 5.1–5.2), include the higher-order flamelet terms that are conventionally neglected by classic flamelet models. Since these higher-order flamelet terms are introduced without resolving to further modeling, our turbulent flamelet model is indeed a higher-order flamelet model. Also worth mentioning is the model's flexibility to be coupled to any LES flow-solver that transports the filtered mixture-fraction and its variance.

## 5.4 *A-Priori* Investigations

This section presents the study that was utilized to assess the higher-order flamelet model. The study was conducted in the context of a turbulent counterflow diffusion flame (TCDF) simulation, which is further described in the following sub-section. Subsequently, the reference DNS solutions of the TCDF configuration, including the instantaneous flow-field characteristics, turbulent kinetic energy spectrum, and scalar-dissipation rate PDF, will be analyzed. Then, a diagnostic LES method that is designed for the *a-priori* investigation of combustion models' performance in a time-varying fashion will be introduced, followed by the results of the analysis.

### 5.4.1 Turbulent Counterflow Diffusion Flame

The choice to use a turbulent counterflow diffusion flame to assess the higher-order flamelet model was made in consideration of the configuration's advantages from a computational viewpoint [129]. Specifically, the benefits of TCDF are:

- Simple, but versatile setup that allows for conditions from flame equilibrium to quenching, hence covering a broad range of turbulent Reynolds and Damköhler numbers ($\mathrm{Re}_\Lambda$ and $\mathrm{Da}_\Lambda$, respectively).
- Compact system, on the order of centimeters, approximately one to two orders-of-magnitude smaller than typical turbulent jet flames.
- Little influence from flame-surface interactions or pilot flames since the flame is hydrodynamically stabilized in the vicinity of the stagnation plane.

Furthermore, the counterflow configuration finds relevance as the flame stabilization strategy in aviation gas turbine combustors, and also serves as the canonical model that represents the near-field environment of strongly strained mixing layers [9]. In a series of studies [129–131], the TCDF configuration was demonstrated to operate under conditions in the Williams' regime diagram [11] that are relevant to Diesel engines and gas turbines ($\mathrm{Re}_\Lambda = [10^2,\ 10^3]$, $\mathrm{Da}_\Lambda = [10^0,\ 10^2]$), exhibiting localized flame holes, flame reignition, strain-induced flame quenching, and substantial flame sheet distortions.

The TCDF configuration that is used in the present work is schematically illustrated in Fig. 5.3, and the essential parameters of the configuration are given in Tab. 5.1. The global turbulent Reynolds and Damköhler numbers are based on the mean integral scale of the homogeneous isotropic turbulence (HIT) simulation that was separately performed to introduce turbulent fluctuations at the fuel and oxidizer boundaries. In order to reduce complexities in the model analysis so that the combustion model's performance can be
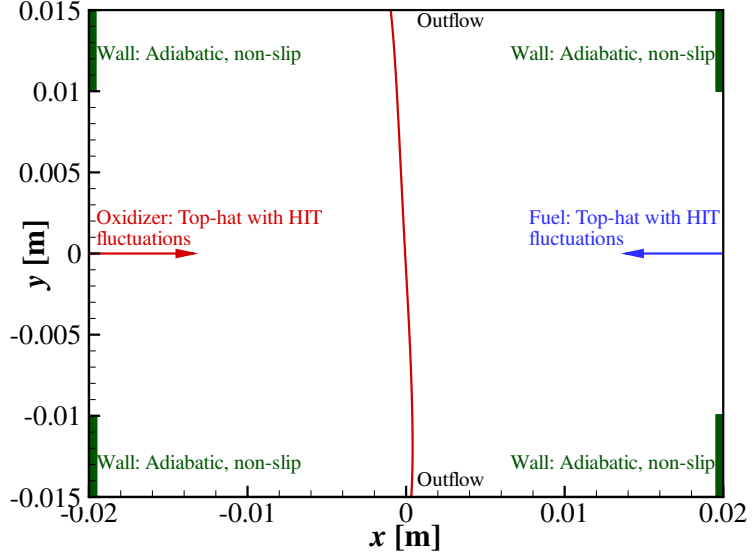
Figure 5.3: TCDF DNS and LES configuration and streamwise ($x$) and traverse ($y$) boundary conditions; the spanwise ($z$) direction uses a periodic boundary condition. The contour line refers to the stoichiometric mixture-fraction isoline.

thoroughly understood, a one-step, irreversible hydrogen/air chemistry mechanism [132] is currently considered. It is noted, however, that the utilization of such a reactive mechanism will favor a stable flame, thus eliminating any occurrence of overall flame extinction in the simulations. The high reactivity of the one-step mechanism is reflected by the high $\mathrm{Da}_\Lambda$, for which the chemical time-scale is estimated with the formulation of Marinov *et al.* [132]:

$$\mathrm{H}_2 + \frac{1}{2}\mathrm{O}_2 \xrightarrow{k_g} \mathrm{H}_2\mathrm{O} \ ,$$

$$k_g = \left(1.8 \times 10^{13}\right) \exp\left(\frac{-17614 \ \mathrm{K}}{T}\right) \ , \quad \dot{\omega} = k_g \left(\frac{\rho Y_{\mathrm{H}_2}}{W_{\mathrm{H}_2}}\right) \left(\frac{\rho Y_{\mathrm{O}_2}}{W_{\mathrm{O}_2}}\right)^{0.5} \ , \qquad (5.32)$$

where the average of the mixing (300 K) and adiabatic (1600 K) temperatures and a stoichiometric composition were used.

## 5.4.2   DNS Flow-Field Analysis

In this section, the flow-field characteristics of the TCDF DNS will be explored. These analyses will facilitate later discussions on the corresponding LES results (cf. Chap. 6), where the DNS results will be regarded as the reference solutions.

The flame-vortex interactions at three instants, each separated by half a characteristic time step, are shown in Fig. 5.4. The characteristic time of the current configuration is

| Parameter | | Value |
|---|---|---|
| Fuel | Slot width | 2 cm |
| | Mean velocity | $[-1, \ 0, \ 0]^T$ m/s |
| | Composition | $Y_{H_2}, \ Y_{N_2} = 0.03, \ 0.97$ |
| | Temperature | 300 K |
| Oxidizer | Slot width | 2 cm |
| | Mean velocity | $[1, \ 0, \ 0]^T$ m/s |
| | Composition | $Y_{O_2}, \ Y_{N_2} = 0.23, \ 0.77$ |
| | Temperature | 300 K |
| Domain size | | $4 \times 3 \times 2$ cm |
| Grid resolution | | $256 \times 192 \times 128$ |
| Chemical kinetics | | 4 species, 1 reaction [132] |
| Stoichiometric mixture-fraction | | 0.49 |
| Velocity fluctuation, $(\|u_i'\| \, / \, \|u_i\|)_{\text{Fuel/Oxidizer}}$ | | 0.2 |
| Integral length | | 5 mm |
| Turbulent Reynolds number, $\mathrm{Re}_\Lambda$ | | 47 |
| Turbulent Damköhler number, $\mathrm{Da}_\Lambda$ | | $3.2 \times 10^4$ |

Table 5.1: Essential parameters of the TCDF DNS.

defined by the reciprocal of the global strain rate:

$$a_g = \frac{\left| \langle \|u_i\| \rangle^{\text{Fuel}} - \langle \|u_i\| \rangle^{\text{Oxidizer}} \right|}{l_x} = \frac{|-1-1|}{0.04} = 50 \ 1/\mathrm{s} \ , \tag{5.33}$$

where the values on the RHS are given in Tab. 5.1. From the figure sequence, we see that the flame-sheet, which is represented by the stoichiometric mixture-fraction iso-surface, is constantly distorted by the vortical structures of the turbulent flow; in figure 5.4, these vortical structures are represented by the definition of Jeong & Hussain [133]. Some of the flame distortions that can be discerned in Fig. 5.4 are: (i) compression, resulting in a relatively flat (quasi two-dimensional) flame-sheet in the earliest instant; and (ii) folding, leading to a multi-dimensional flame-sheet of the latest time. The variation of the temperature field along the flame-sheet indicates that the strain on the flame-sheet, which tends to induce flame-quenching and hence is reflected by the low temperature region, is shifting from the negative spanwise side towards the centerplane ($z = 0$). However, based on the temperature of the flame-sheet, which is always at least five times larger than the injection temperature of 300 K, we note that there is no occurrence of flame-extinction in the DNS across the evaluated time period. This resilience of the flame is attributed to the use of a one-step hydrogen/air chemistry mechanism [132], which is highly reactive. Another indication of the strong reaction from using the one-step chemistry is the small flame-

thickness, $l_{\text{Fl}}$, that can be observed from the temperature contours along the $y = 0$ plane shown in Fig. 5.4. The contour lines in the $y$-plane describe the planar intersection with the vortices, emphasizing the correlation between the flame-sheet and vortical structures.

The mean turbulent kinetic energy spectrum, which is shown in Fig. 5.5, is obtained by averaging over one characteristic time period of $0.02$ s, using the results presented in Fig. 5.4. The convergence (arrow) of the spectrum at intermediate instants (thin curves) towards the mean spectrum (thickened curve) suggests that this dataset, which is used in the subsequent studies, has sufficiently approached a statistically-steady state. Compared to the analytical Kolmogorov $-5/3$-spectrum, which is indicated by the slope of the thickened linear line, the mean energy spectrum does not display a noticeable integral range. This absence of scale is common to the low turbulent Reynolds number regime, wherein the current TCDF configuration belongs. Due to low Reynolds number, the Kolmogorov length-scale, $\eta$, is just approximately $1/3$ of the mean flame-thickness, $l_{\text{Fl}}$ (solid vertical line) and therefore more likely to be larger than the reaction-zone thickness, resulting in the lack of flame-extinction as aforementioned.

Further indication of a statistical-steady state in the current dataset can be inferred from the smoothness of the scalar-dissipation rate PDF, shown in a discrete form in Fig. 5.6. The dissipation-rate profile is seen to approximately resemble its analytical log-normal distribution [134], which is given by the thin line in Fig. 5.6 and calculated using the mean and variance of the logarithm of the scalar-dissipation rate. The discrepancies between the two PDFs may be attributed to the presence of reaction in the current flow, which will increase diffusivity and laminarize the flow. In turn, the laminarization is possibly the cause of the dense region at low $\chi_Z$-values seen in the PDF extracted from the DNS.

The joint PDF of scalar-dissipation rate and temperature along the flame-sheet, shown in Fig. 5.4, is given in Fig. 5.7, along with the S-shaped curve that corresponds to the current configuration. From the distribution, we see that the variations in both $\chi_{Z,\text{st}}$ and $T_{\text{st}}$ are modest, spanning a range of $\sim 10$ 1/s and $\sim 50$ K, respectively. However, analysis within the region of high probability, which is denoted by darker colors, indicates that the results deviate from the solutions of SLFM, which reside on the S-shaped curve. Therefore, we can deduce that the flamelets in the current TCDF are mildly unsteady.

Overall, this flow-field study demonstrates that the current TCDF does possess the necessary complexities, namely flamelet unsteadiness and turbulence-flame interactions, but at a moderate level so that the assessment of the proposed model will not be overwhelmed by the difficulties posed by the flow-field. From a modeling perspective, this approach is acceptable because the characteristics of the combustion model can then be understood thoroughly, thus facilitating its further application to more complicated configurations.
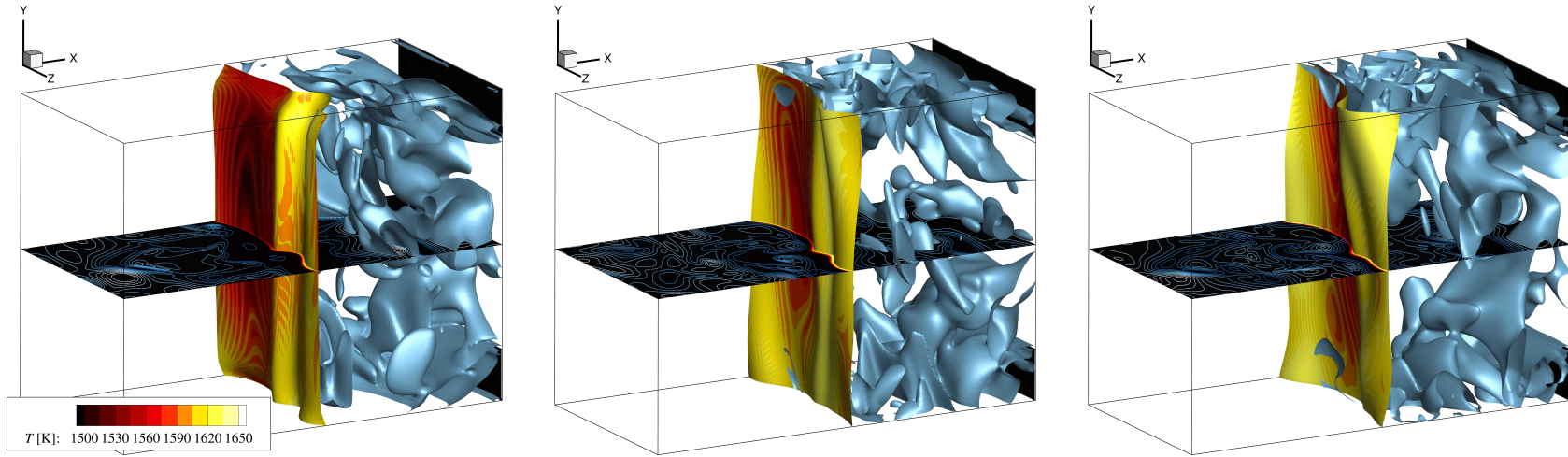
Figure 5.4: Flame-vortex interactions from the TCDF DNS at three instants, increasing in steps of half a characteristic time of $0.02$ s from left to right. In each figure, the flame-sheet (stoichiometric mixture-fraction iso-surface) is colored by temperature, and the vortex tubes are represented by the iso-surface of the second eigenvalue, $\lambda_2 = 0$, of the symmetric tensor $s_{ij}s_{ji} + \Omega_{ij}\Omega_{ji}$ [133], where $s_{ij}$ and $\Omega_{ij}$ refer the symmetric and asymmetric components of the velocity-gradient tensor. The intersection of the vortex tubes and the $y = 0$ plane, which is also colored by temperature, is shown by the contour lines.

### 5.4.3 Constrained LES Methodology

As aforementioned, the current study is conducted with a method that considers the temporal effects of the combustion model. This method, hereafter referred to as the constrained LES technique, is introduced to make full use of the autonomy from performing our own DNS. In essence, the method consists of the DNS of the TCDF configuration, along with the additional procedures of: (i) spatial-filtering of all flow-field information (i.e. density, diffusivities, and velocities); and (ii) solving of filtered transport equations that utilize the filtered DNS flow quantities; which are performed simultaneously. Through these treatments, the method is essentially considering an LES with a perfect turbulence model, thus constraining errors to be dominantly attributed to the combustion model. Numerical errors, which are usually insignificant relative to the model errors, will not be relevant since the calculations are performed with mathematical operators of the same solver, thus affecting each step in a consistent and impartial manner. In contrast to the proposed technique, conventional combustion model assessments will usually involve the post-processing of individual instantaneous DNS snapshots, which may overpredict the model performance because the error accumulation over time cannot be accounted for.

To further illustrate the concept, the constrained LES technique will, for each iteration, solve the following equation set:

$$\frac{\partial \rho}{\partial t} + \frac{\partial \rho u_i}{\partial x_i} = 0 \ , \tag{2.14a}$$

$$\frac{\partial \rho u_i}{\partial t} + \frac{\partial \rho u_i u_j}{\partial x_j} = -\frac{\partial p}{\partial x_i} + \frac{\partial}{\partial x_j}\left[ 2\mu \left( s_{ij} - \frac{1}{3}\frac{\partial u_k}{\partial x_k} I_{ij} \right) \right] \ , \tag{2.14b}$$

$$\frac{\partial \rho Y_\alpha}{\partial t} + \frac{\partial \rho u_i Y_\alpha}{\partial x_i} = \frac{\partial}{\partial x_i}\left[ \rho D \frac{\partial Y_\alpha}{\partial x_i} \right] + \rho \dot{\omega}_\alpha \ , \tag{5.34a}$$

$$\frac{\partial \overline{\rho}\widetilde{Y_\alpha}^*}{\partial t} + \frac{\partial \overline{\rho u_i}\widetilde{Y_\alpha}^*}{\partial x_i} = \frac{\partial}{\partial x_i}\left[ \overline{\rho D}\frac{\partial \widetilde{Y_\alpha}^*}{\partial x_i} \right] + \overline{\rho \dot{\omega}_\alpha}^*$$

$$+ \frac{\partial}{\partial x_i}\left[ -\overline{\rho}\widetilde{(u_i Y_\alpha)''} + \overline{\rho}\widetilde{\left( D\frac{\partial Y_\alpha}{\partial x_i} \right)''} \right] \ , \tag{5.34b}$$

where the first three equations denote the standard DNS formulation, while the asterisk $(\ )^*$ in Eq. (5.34b) indicates a modeled variable. All the spatially-filtered $\overline{(\ )}$-terms and turbulent fluxes in the latter equation are provided from the DNS solutions of the first two equations of the set. Therefore, if a combustion model is exact, the modeled $\widetilde{Y_\alpha}^*$ term of Eq. (5.34b) will be identical to the Favre-filtered $Y_\alpha$ solution of Eq. (5.34a). Conversely, any inaccuracies in the combustion model will lead to discrepancies between the transported $\widetilde{Y_\alpha}^*$ term and the Favre-filtered $Y_\alpha$ field.
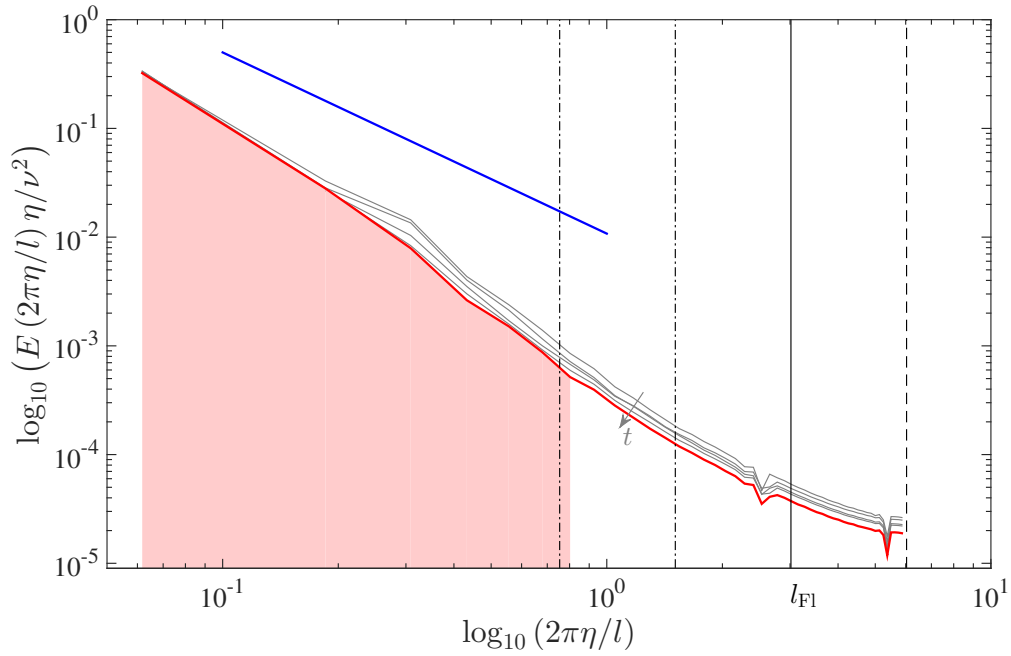
Figure 5.5: Mean turbulent kinetic energy spectrum, averaged across one characteristic time period of $0.02$ s using the results shown in Fig. 5.4. The intermediate spectrums are illustrated by the thin curves, showing clearly a convergence towards the final mean spectrum (thickened curve) and hence a statistically steady-state. The shaded region denotes the range that contains 98% of the turbulent energy, and the dashed (– –) and solid (—) vertical lines represent the mean flame-thickness $l_{Fl}$ and Nyquist limit, respectively. The order of $2l_{Fl}$ and $4l_{Fl}$ are denoted, from right to left, by the dashed-dotted vertical lines (–·–), and the Kolmogorov $-5/3$-spectrum is indicated by the slope of the thickened linear line.
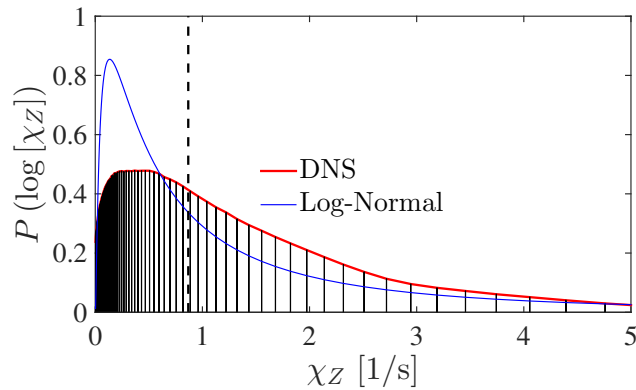


Figure 5.6: Discrete representation of the scalar-dissipation rate PDF across one characteristic time period of $0.02$ s. The thin line indicates the analytical log-normal distribution [134] obtained from the mean $(-0.14)$ and variance $(1.9)$ of $\log[\chi_Z]$. The dashed line indicates the mean scalar-dissipation rate, $\langle \chi_Z \rangle = 0.9$ 1/s.
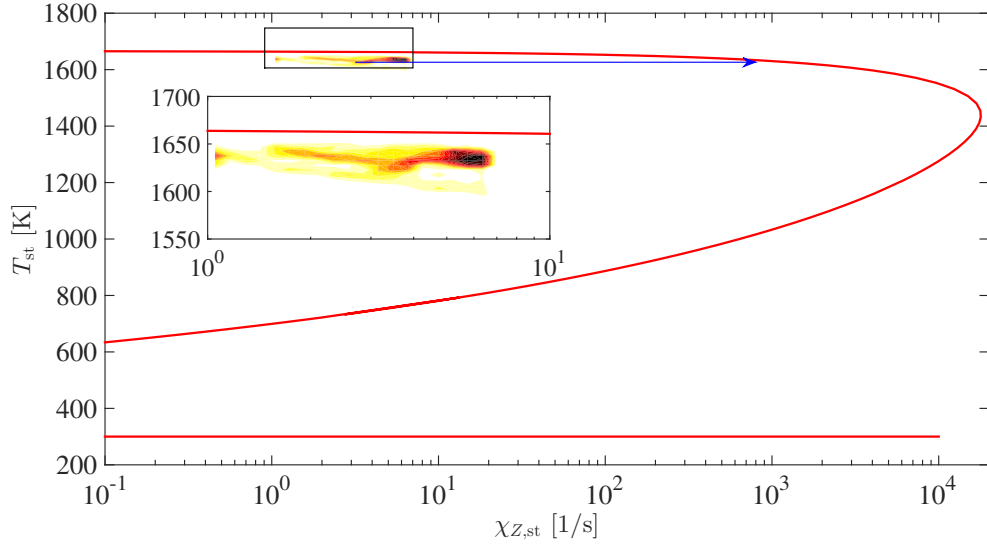
Figure 5.7: Joint PDF of scalar-dissipation rate and temperature along the flame-sheet (cf. Fig 5.4) across one characteristic time period of $0.02$ s. The inset, which better illustrates the region of high probability (dark color), demonstrates that the dataset deviates from the steady laminar flamelet formulation, which is described by the S-shaped curve (—). The arrow indicates the general region on the S-shaped curve where the FPV model will obtain its solutions.

Note that the conservative form of the simplified species equation (5.34a) is used here only for brevity. The method is in fact general, and has been applied to the working temperature and species equations (2.14c)–(2.14d), in which the consideration of a correction velocity term and a non-homogeneous mixture molecular weight profile (cf. Eq. (2.6)) will only introduce additional diffusive and turbulent flux terms of forms analogous to those given in Eq. (5.34b).

## 5.4.4 Constrained LES Analysis

The TCDF simulation results from the constrained LES using three combustion models, namely the current higher-order flamelet model (HOFM), conventional FPV model, and laminar approximation model (i.e. no combustion closure), and a filter-width of $\Delta/l_{\rm Fl} = 3$ are shown in Fig. 5.8–5.9. Note that, in these figures, the DNS results are filtered before the spanwise-averaging step, which is applied on all results. The two instants shown in the figures refer to the half (center column) and full (right column) period of the characteristic time of $0.02$ s, which is defined by the reciprocal of the global strain rate (cf. Eq. (5.33)). All three constrained LES use the same initial condition that is represented by the mean

filtered DNS results of the earliest instant shown by the left diagram of Fig. 5.4 and borrow the closure for turbulence from the simultaneous DNS, as explained in Sec. 5.4.3. For the ease of discussion, this earliest instant will be taken as the temporal origin and referred to as $t = 0$ hereafter, so the other two instants will be $t = 0.01$ s and $t = 0.02$ s accordingly.

In Fig. 5.8, the spanwise-averaged, filtered temperature profile for all combustion models exhibit qualitative agreement with the reference mean filtered DNS solutions, which is expected from the simplicity of the current setup and the omission of errors from the turbulence SGS model.

While not apparent in the qualitative comparison of filtered temperature in Fig. 5.8, the filtered temperature profile predicted by the different combustion models does vary in its accuracy relative to the reference DNS solution. This observation can be best made in terms of a correlation plot using scattered data that are derived from the point-to-point comparison of results against the reference DNS solutions. The correlation plots for the mean filtered temperature corresponding to Fig. 5.8 are given in Fig. 5.9, where the abscissa and ordinate denote the reference DNS results and modeled solutions, respectively, and any error is reflected as a deviation from the perfect correlation line, which is denoted by the diagonal of the plot. This deviation can be quantified by the slope of the linear best-fit line of the scatters, which are illustrated by the thickened lines in the figures and presented in Tab. 5.2. In essence, a slope that is more than one indicates an overprediction in the evaluated quantity, and vice versa.

| Combustion Model | Linear Best-Fit Slope | |
|---|---|---|
| | $t = 0.01$ s | $t = 0.02$ s |
| Mean Filtered Temperature | | |
| HOFM | 0.95 | 1.06 |
| FPV | 0.93 | 0.89 |
| Laminar | 0.96 | 0.93 |

Table 5.2: Comparison of the slope of the linear best-fit for the modeled results relative to the reference DNS solutions, which are illustrated in Fig. 5.9 by the thickened lines.

In consistent with the qualitative comparison, the filtered temperature profiles are reasonably captured in the LES, with all the slopes of the linear best-fit approximately within 10% of unity. Slight underprediction in the filtered temperature are consistently observed for the FPV and laminar model results, while the HOFM temperature solution is slightly underpredicted at $t = 0.01$ s and evolve to an overprediction at the later time.

In summary, this analysis shows that the proposed HOFM model can be applied as a combustion closure model for turbulent reacting flow LES, showing improvement over the laminar approximation model in the TCDF configuration. It should be recognized, how-
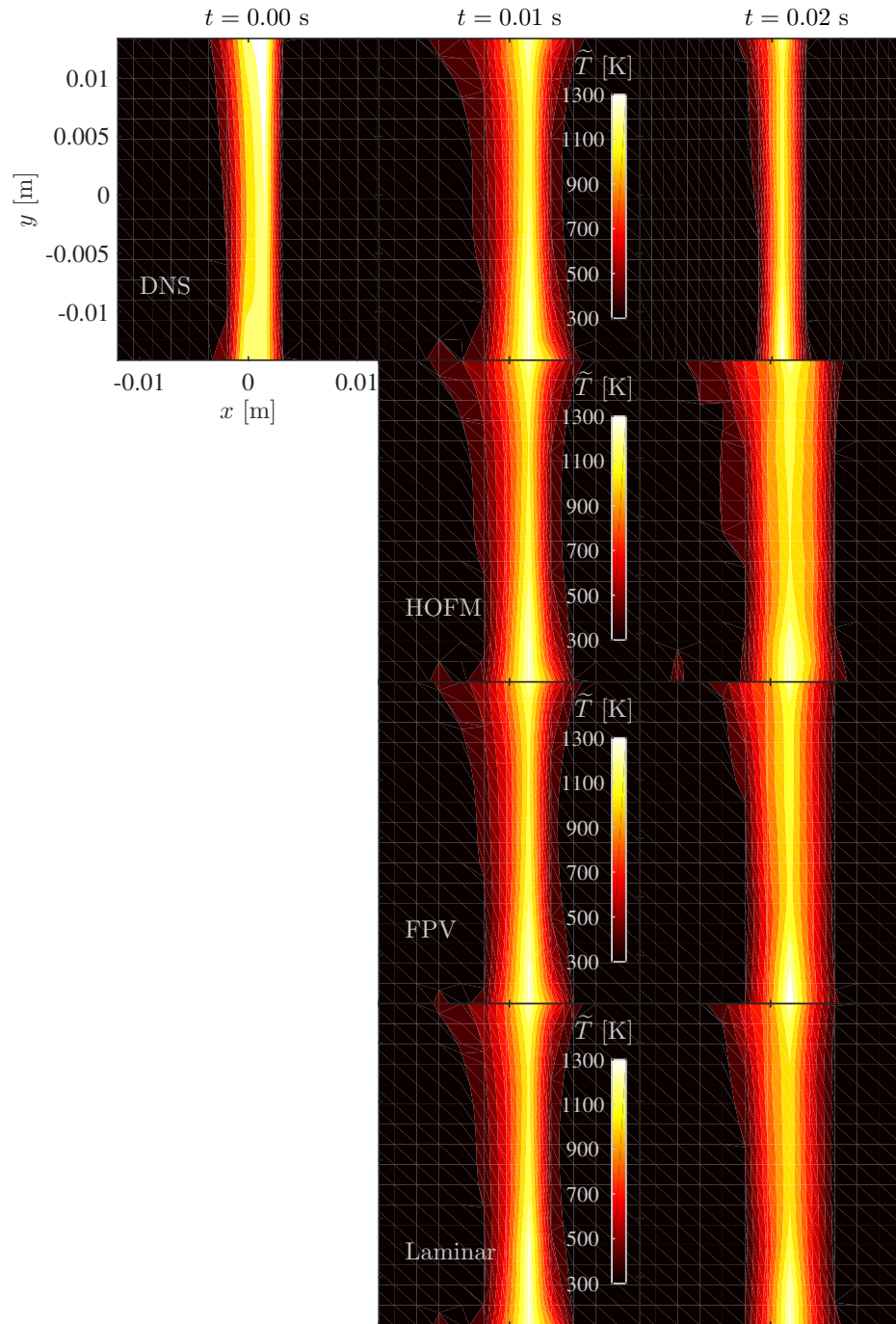
Figure 5.8: Spanwise-averaged, filtered temperature from DNS, HOFM, FPV, and laminar model (top to bottom) at $t = 0.01$ s (center) and $t = 0.02$ s (right). The filter-width is $\Delta/l_{\mathrm{Fl}} = 3$. Only the filtered DNS profile is needed for $t = 0$ (left) because it is the initial condition for the LES.
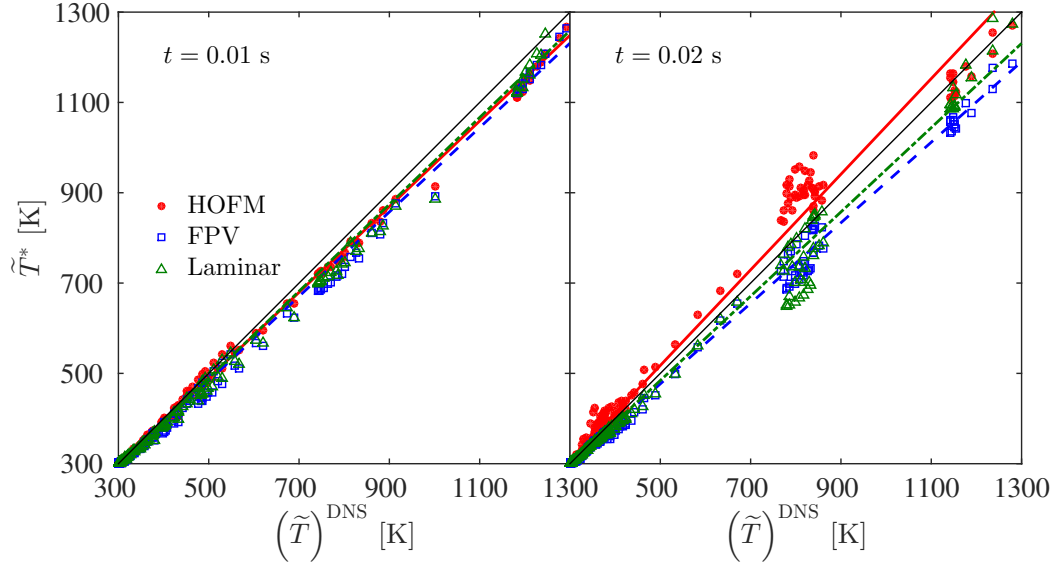
Figure 5.9: Correlation plot for the spanwise-averaged, filtered temperature of HOFM (●, —), FPV (□, --), and laminar (△, ---) model relative to that of DNS at $t = 0.01$ s (left) and $t = 0.02$ s (right). The thickened lines are the respective linear best-fit of the scatters, while the thin line denotes a perfect correlation. The filter-width is $\Delta/l_{\mathrm{Fl}} = 3$.

ever, that the analysis has specifically eliminated errors due to the turbulence SGS model, which can lead to further inaccuracies in the combustion model predictions. Therefore, further model performance evaluations on the HOFM were performed in similar fashion to this section, but in the context of actual LES, as discussed in the following section.

# CHAPTER 6

# Application of Higher-Order Flamelet Model

Following on from the formal model derivations and encouraging *a-priori* assessment results of the preceding chapter, the proposed higher-order flamelet model is applied to actual LES in the following. The LES are performed in the context of the same turbulent counterflow diffusion as the *a-priori* studies. Therefore, the presented DNS results can be employed as the reference solutions, because they are computed with all combustion and turbulent scales resolved and without additional models other than those discussed in Sec. 2.2. However, in order to compare to LES results, which pertain to Favre-filtered variables (cf. Sec. 2.3), the DNS solutions first have to be explicitly filtered. The effects of such treatment on the DNS solutions, performed in accordance to the Favre formulation, are first investigated. Then, the LES with three combustion closure models, namely HOFM, FPV, and laminar approximation, will be presented, followed by a study of one particular flamelet extracted from the filtered field to substantiate HOFM's good agreements with the reference DNS solutions.

## 6.1 Filtered Flow Field Analysis

The resolved flame-vortex interactions at three instants, each separated by half a characteristic time step, defined by the reciprocal of the global strain rate (see Eq. (5.33)), are shown in Fig. 6.1. These data are filtered from the results of Fig. 5.4 using a filter-width of $\Delta/l_\mathrm{Fl} = 2$ , thus allowing for direct comparisons with the earlier observations of the unfiltered results. The amount of information lost from the filtering is quantified by the region to the right of the dashed-dotted line at higher wavenumber of the turbulent kinetic energy spectrum, as shown in Fig. 5.5. From the energy spectrum, we see that more than 98% of the turbulent energy (shaded region) is resolved with the current filter-width.
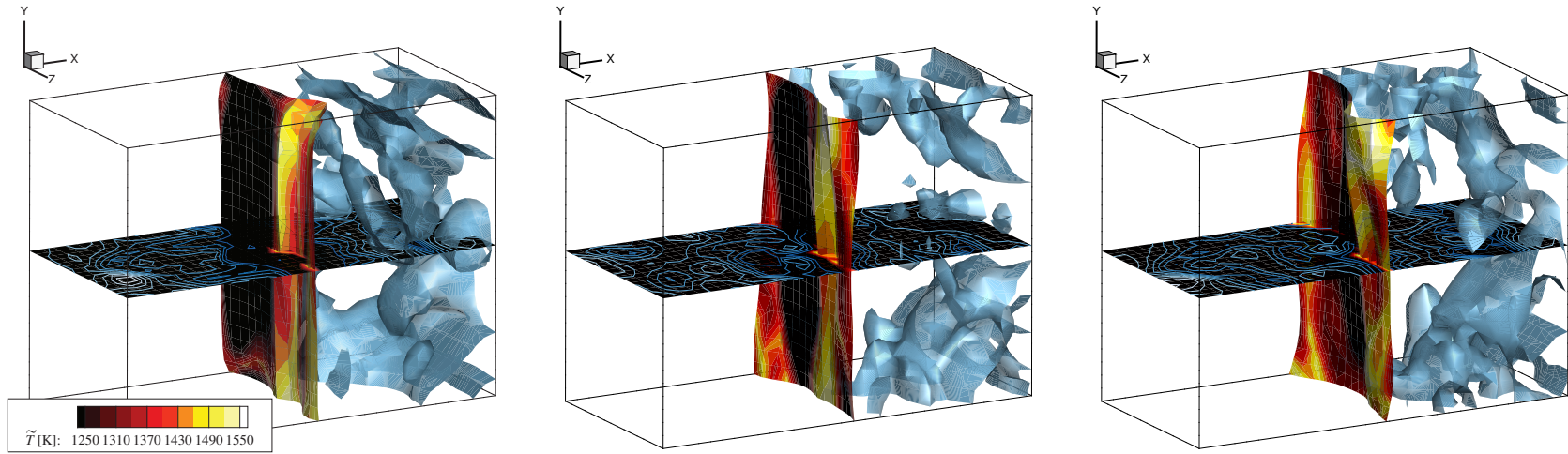
Figure 6.1: Resolved flame-vortex interactions from the Favre-filtered TCDF DNS at three instants, increasing in steps of half a characteristic time of $0.02$ s from left to right. In each figure, the resolved flame-sheet (stoichiometric filtered mixture-fraction iso-surface) is colored by Favre-filtered temperature, and the vortex tubes are represented by the iso-surface of the second eigenvalue, $\lambda_2 = 0$, of the symmetric tensor [133] constructed by the symmetric and asymmetric components of the resolved velocity-gradient tensor. The intersection of the vortex tubes and the $y = 0$ plane, which is also colored by filtered temperature, is shown by the contour lines. Note that the unfiltered counterparts of these results are given in Fig. 5.4 and the filter-width is $\Delta/l_{Fl} = 2$.

Most noticeable of all is the loss in fine-scale features in both types of iso-surface, especially for the vortex tubes. In contrast, the filtered flame-sheet still bears a resemblance to its unfiltered counterpart, exhibiting features of quasi two-dimensionality due to compression and vortex-induced folding at the earliest and later instants, respectively. Applying the earlier conventions of Sec. 5.4.2, these snapshots will hereafter be referred to as $t = 0$, $t = 0.01$ s, and $t = 0.02$ s.

Another prominent difference between the filtered and unfiltered results is the substantially lower resolved temperature, with a maximum value of approximately $1500$ K, which is the minimum temperature along the unfiltered flame-sheet. This decrease in temperature, which is reflected by the dark region along the filtered flame-sheet, is so dominant that the shifting of high strain on the sheet towards the centerplane in the unfiltered case is no longer apparent. Instead, multiple cool spots are discerned along the filtered flame-sheet.

From the $y = 0$ plane in figure 6.1, the filtered flame is slightly thicker than its unfiltered counterpart, but overall still thin relative to the domain length-scales. In addition, the influence of the resolved vortical structures on the filtered flame-sheet is still noticeable from the contour lines shown on the $y$-plane.

In Fig. 6.2, one-dimensional filtered (thickened solid line) and unfiltered (thin solid lines) temperature profiles in mixture-fraction space at $t = 0$ are presented. The filtered profile in figure 6.2 corresponds to the flamelet that passes through the spatial origin, which we will hereafter refer to as the centerline flamelet. The centerline flamelet profile is extracted using the technique described in Sec. 4.1, wherein the spatial origin is used as the starting point for the gradient-tracing operation. On the other hand, the unfiltered distributions correspond to the various flamelets that are enclosed by the filter-cell around the origin, and are extracted with the same technique as the centerline flamelet, but using the grid points within the filter-cell as the starting locations for the gradient-tracing.

Comparing the filtered and unfiltered profiles in Fig. 6.2, the resolved temperature is clearly lower than the unfiltered temperature, which is a typical effect due to filtering. Interestingly, we see that the resolved and unfiltered temperature profiles will converge at both fuel-lean and fuel-rich regions, suggesting that the turbulence-chemistry interactions occur mostly in a mixture-fraction range that is closer to the inner flame- and reaction-zones [111]. Also, in contrast to the unfiltered profiles, which peak at the stoichiometric mixture-fraction value of $0.5$, the filtered $\widetilde{T}$-profile skews slightly towards the fuel-lean and has its maximum point at $\widetilde{Z} \approx 0.45$.

Considering the SLFM solution (thickened dashed-dotted line of Fig. 6.2) with the same peak unfiltered temperature value of $\max[T] = 1600$ K, the unfiltered profiles are seen to be accurately described by the steady flamelet profile on the fuel-rich side, but are slightly

lower than the flamelet solution on the fuel-lean side. An inset that emphasizes on the close-up region around the peak of these profiles has been provided in figure 6.2 to further demonstrate this discrepancy between the SLFM and DNS profiles at the fuel-lean side.
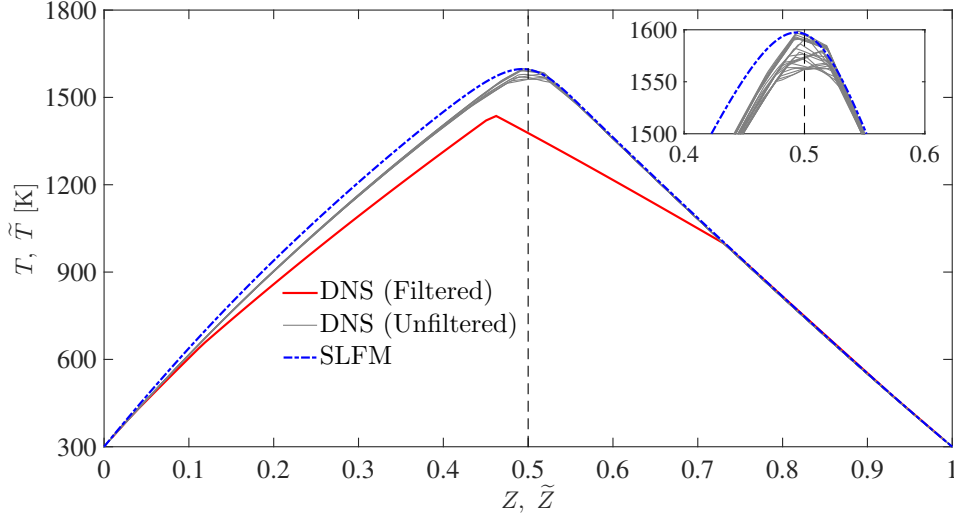


Figure 6.2: Instantaneous one-dimensional Favre-filtered (thickened solid line) and unfiltered (thin solid lines) temperature profiles in mixture-fraction space at $t = 0$. The dashed-dotted curve indicates the SLFM solution that has the same maximum temperature as the unfiltered profiles, and the dashed vertical line denotes the stoichiometric mixture-fraction $Z_{st} = 0.5$. The inset is provided to emphasize the discrepancies between the SLFM and unfiltered profiles. Note that the filtered distribution corresponds to the centerline flamelet that passes through the spatial origin, while the unfiltered profiles are extracted from multiple flamelets that are contained within the $\Delta \times \Delta \times \Delta = 2l_{Fl}^3$ filter-cell around the origin. Refer to Fig. 6.12(b) for an illustration of the different flamelets and filter-cell.

In general, the effects of explicit filtering of the DNS solutions are reflected by: (i) a loss of spatial information, which can be quantified with a turbulent kinetic energy spectrum (cf. Fig. 5.5) and qualitatively observed in the decrease in fine-scale structures; and (ii) a decrease in the maximum absolute scalar value, which is attributed to the smoothing of sharp profiles in the scalar field. As previously discussed, these filtering effects will pose problems in the LES of turbulent reacting flows because the Favre-filtered reaction-rates and turbulent flux terms in Eqs. (2.18) are then unclosed. The role of a combustion closure model is to describe the interaction between the lost subgrid information and the resolved scale so that the unclosed reaction terms can be accurately predicted.

## 6.2 Large-Eddy Simulations of TCDF

The LES results for the TCDF configuration introduced in Sec. 5.4.1 are presented in this section. This study will first focus on the case of filter-width $\Delta/l_{\text{Fl}} = 2$, analyzing qualitatively and quantitatively the performance of three combustion models, namely the proposed HOFM, classical steady FPV model, and no-closure laminar approximation, using the spanwise-averaged, filtered DNS results as the reference solutions. Then, the effects of different filter-width on the accuracies of the three models are evaluated in terms of the errors relative to the reference filtered DNS solutions. For this evaluation, three filter-widths of $\Delta/l_{\text{Fl}} = \{1, \ 2, \ 4\}$ are considered. For reference, these filter levels are denoted on the turbulent spectrum in Fig. 5.5 by a vertical solid and two dashed-dotted lines.

### 6.2.1 LES Results

In Fig. 6.3, the spanwise-averaged, filtered temperature profile for the two flamelet models exhibit qualitative agreement with the reference mean filtered DNS solutions, which has also been observed in the constrained LES study in Sec. 5.4.4. In contrary to the *a-priori* analysis, however, this agreement is not expected here due to the inclusion of turbulence SGS model errors and loss of subgrid information.

While one may argue based on the low turbulent Reynoldes number of the current setup that the turbulence-chemistry interactions are likely insignificant, the influence of the lost information due to filtering is definitely not negligible, resulting a significant underprediction of temperature by the laminar model. This observation is worthnoting because HOFM is in fact currently programmed in the reacting flow-solver using the code-structure of the laminar model as its basis. In other words, the role of HOFM in these LES can be interpreted as a closure to the laminar approximation. Hence, considering the improvement of HOFM results over the laminar approximation solutions, it is reasonable to deduce that HOFM is indeed properly closing the filtered reaction term, in accordance to the model derivation given in Sec. 5.3.

For the spanwise-averaged, filtered heat-release profile, which is shown in Fig. 6.4, only HOFM is seen to provide a reasonable description of the reference mean filtered DNS solutions in terms of the profile range in $x$ and its averaged values. In contrast, the steady FPV model exhibits a significantly overpredicted heat-release rate that is noticeably broader than the reference solutions. On the other hand, the laminar model shows an underpredicted heat-release rate profile that lacks spreading to the fuel-rich side (i.e. $+x$-direction), which is consistent with the underprediction in the Favre-filtered temperature field shown in the last row of Fig. 6.3.
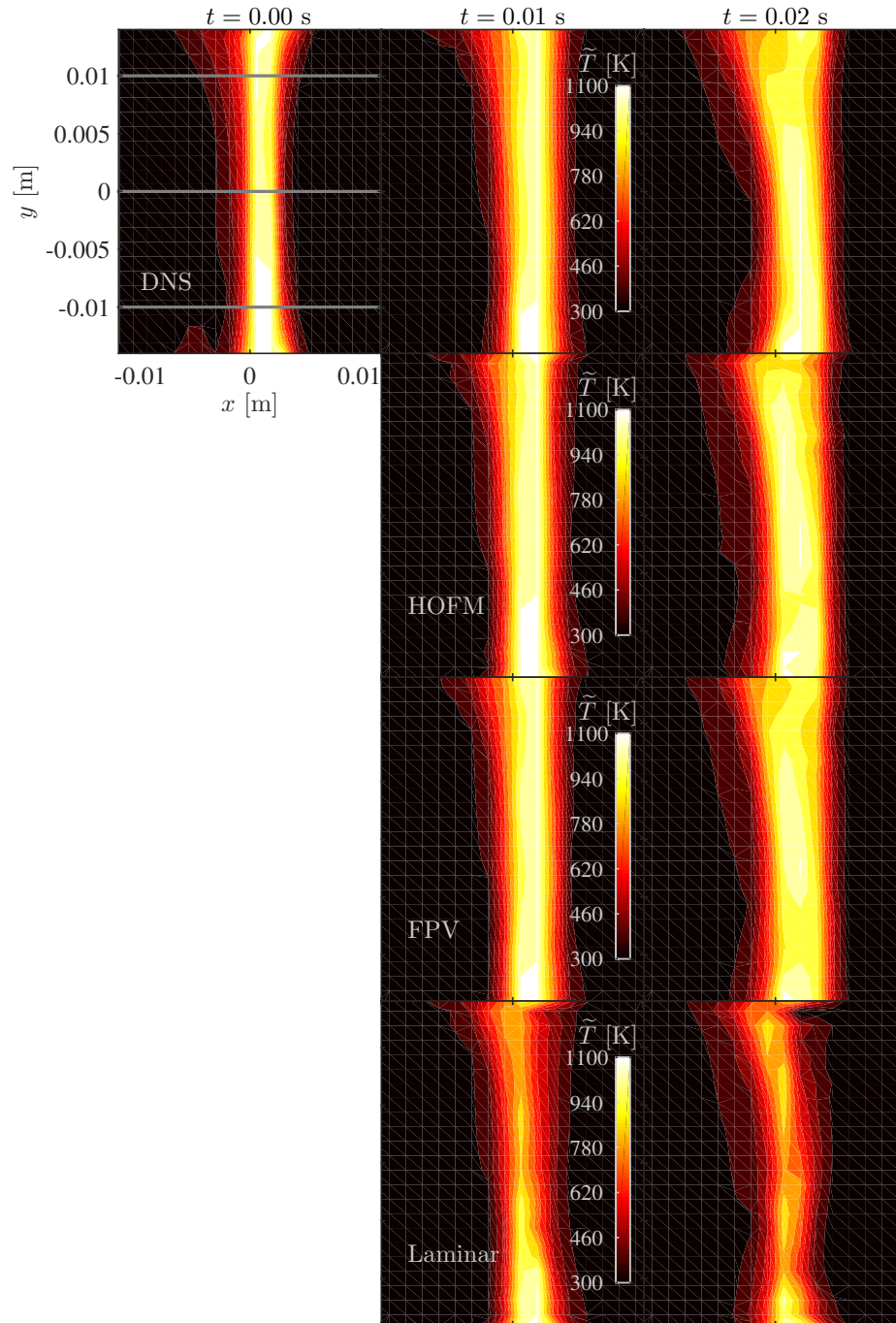
Figure 6.3: Spanwise-averaged, filtered temperature from DNS, HOFM, FPV, and laminar model (top to bottom) at $t = 0.01$ s (center) and $t = 0.02$ s (right). The filter-width is $\Delta/l_{\text{Fl}} = 2$. Only the filtered DNS profile is needed for $t = 0$ (left) because it is the initial condition for the LES. The three horizontal lines at the $t = 0$ plot indicate the three $y$-locations that were considered by Figs. 6.5–6.6.
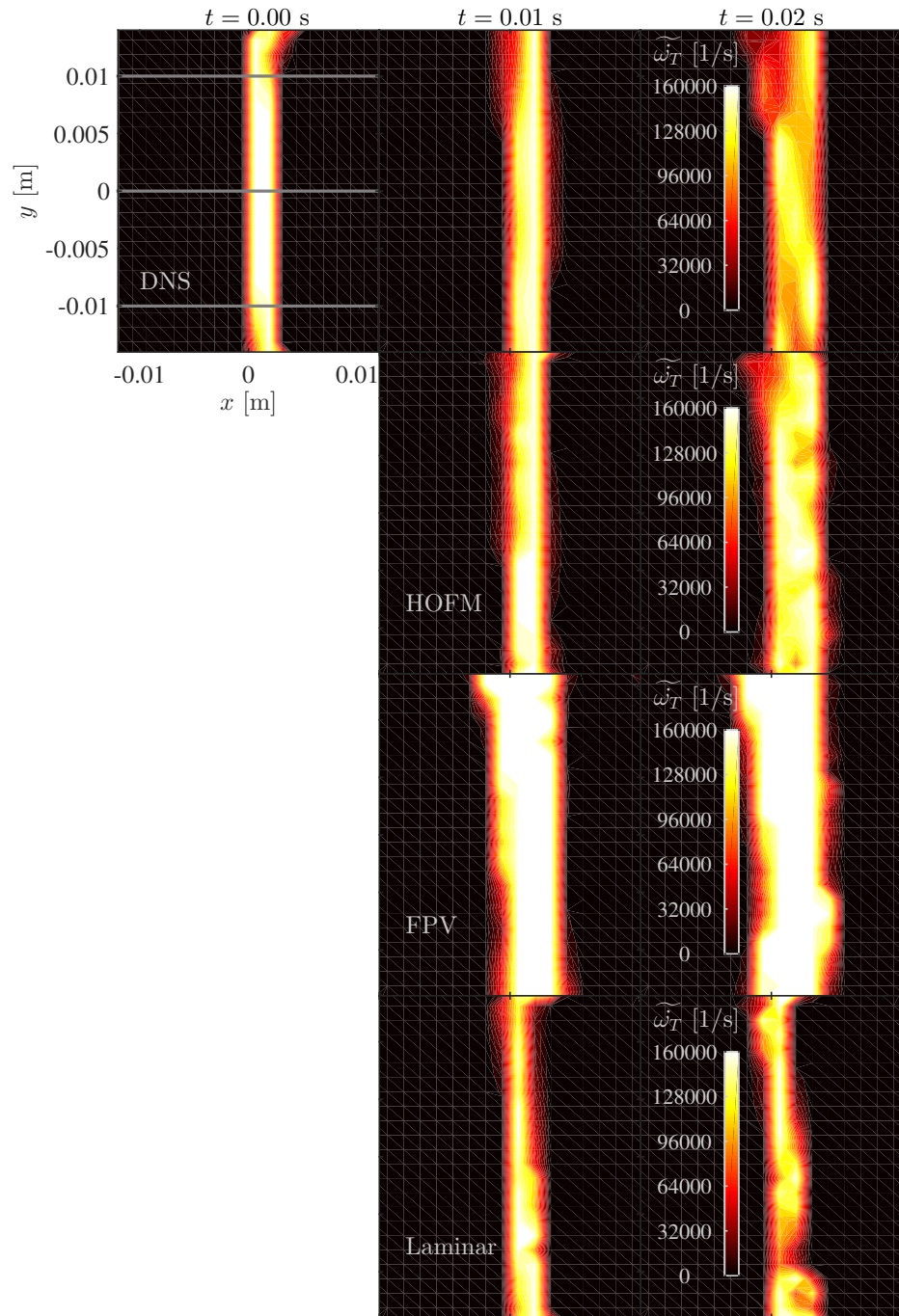
Figure 6.4: Spanwise-averaged, filtered heat-release rate from DNS, HOFM, FPV, and laminar model (top to bottom) at two instants. Refer to Fig. 6.3 for further details.

Quantitative comparisons with the reference DNS solutions are provided in terms of three streamwise profiles of $\widetilde{T}$ and $\widetilde{\omega}_T$ for $y = \{-0.01,\ 0,\ 0.01\}$ m at $t = 0.01$ s. The three $y$-locations are indicated by the horizontal lines shown in the $t = 0$ plot of Figs. 6.3–6.4. Note that the analysis for $t = 0.02$ s is not provided in the interest of brevity, since similar conclusions to the given case will be drawn.

From Fig. 6.5, the good agreement between the flamelet LES solutions and the reference DNS results remains obvious, while the underprediction in the Favre-filtered temperature by the laminar model is observed for all three locations. Also, the peak value of the laminar model profile displays a higher tendency to deviate from the stoichiometric mixture-fraction, which can be attributed to the model's underprediction in the stoichiometric $\widetilde{\omega}_T$ value seen in Fig. 6.6. Note that the ordinate of figure 6.6 has been shown in a logarithmic scale to accommodate the $\mathcal{O}(10)$ overprediction in the heat-release rate by the steady FPV model. In contrast, HOFM consistently demonstrates a good agreement with the reference filtered heat-release rates around the vicinity of the stoichiometric mixture-fraction, but overpredicts the term at both fuel-lean and fuel-rich regions. However, the inaccuracies at these regions are typically not severe since the corresponding flow is usually not sensitive to the reaction-rate, as demonstrated by the resolved temperature profiles.

Similar to the constrained LES study, correlation plots for the filtered temperature and heat-release rate are generated using scattered data that are derived from the point-to-point comparison of LES results against the mean filtered DNS solutions, which have been shown in Figs. 6.3–6.4. The corresponding correlation plots for the mean $\widetilde{T}$ and $\widetilde{\omega}_T$ are given in Fig. 6.7 and 6.8, respectively, where, as in Fig. 5.9, the abscissa and ordinate denote the reference DNS results and modeled solutions, respectively. Any error is reflected as a deviation from the perfect correlation line, which is denoted by the diagonal of the plot. This deviation is presented in Tab. 5.2 in terms of the slope of the linear best-fit line of each scatter dataset, where a value larger than unity indicates an overprediction of the evaluated quantity, and vice versa.

In consistent with the previous analyses, the filtered temperature profiles, shown in Fig. 6.7, are accurately captured in the LES with the two flamelet models, with all the slopes of the linear best-fit within 5% of unity. The underprediction in the filtered temperature are consistently observed for the laminar model results, for which the slope of the best-fit line deviates from unity by as much as 40%. For the filtered heat-release rate predictions, which are illustrated in Fig. 6.8, only the HOFM results show a reasonable agreement with the reference solutions, featuring a linear best-fit gradient that has only 1% error at $t = 0.01$ s and deteriorates to an overprediction of approximately 20%. Despite its accurate prediction of the filtered temperature, the FPV model is observed to provide a significant
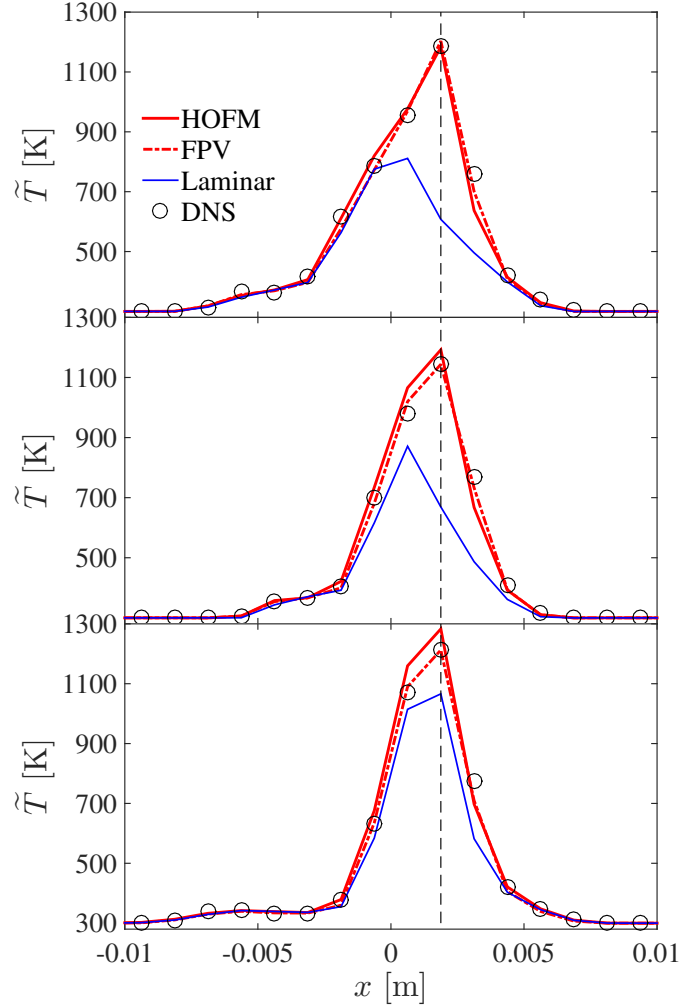
Figure 6.5: One-dimensional streamwise profiles of the spanwise-averaged, filtered temperature at $t = 0.01$ s from DNS ($\bigcirc$), HOFM (thickened —), FPV (thickened ---), and laminar model (thin —) at $y = 0.01$ m (top), $y = 0$ (middle), and $y = -0.01$ m (bottom). These locations are denoted by the three horizontal lines shown in the $t = 0$ plot of Fig. 6.3. The vertical dashed line indicates the location of the mean, filtered $Z_{\mathrm{st}} = 0.5$.

overprediction in the heat-release rate that approaches $\sim \mathcal{O}(10)$, which is an order higher than the reference value of unity. In contrast, the laminar model is seen to consistently underpredict the heat-release rate with more than 25% error.

Hence, we see in this section from both qualitative and quantitative analyses that, for the current TCDF configuration: (i) both the flamelet models are capable of capturing the Favre-filtered thermochemical scalar profiles; (ii) only HOFM provides a reasonable description of the filtered source terms, whereas FPV model is always overpredicting the reaction-rates; and (iii) a lack in the representation of subgrid information will lead to
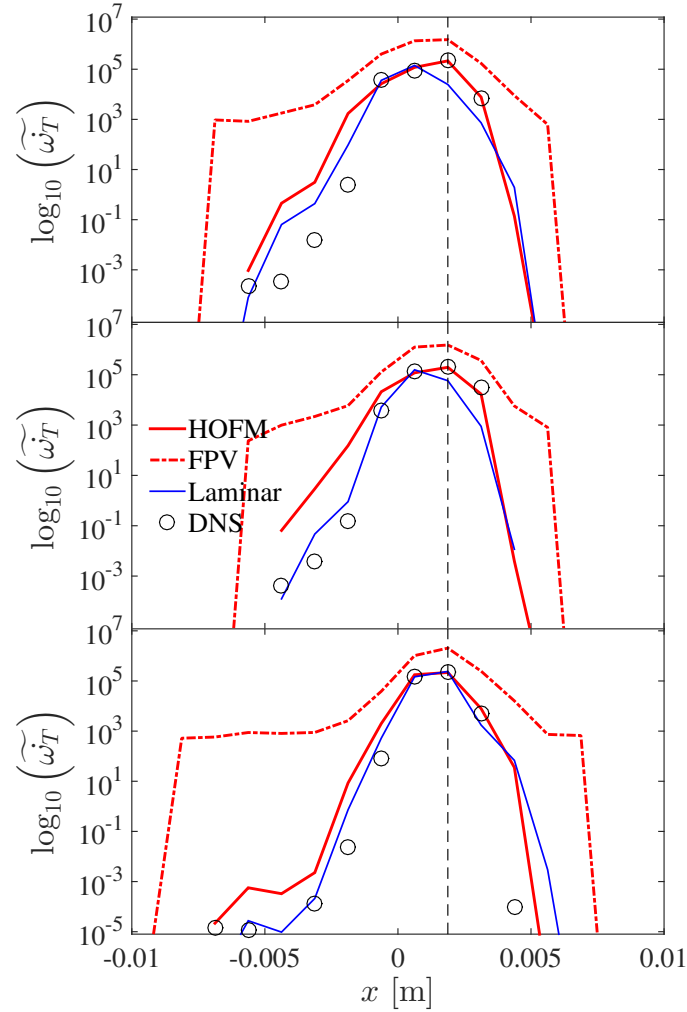
Figure 6.6: One-dimensional streamwise profiles of the spanwise-averaged, filtered heat-release rate at $t = 0.01$ s for three $y$-locations, which are denoted by the three horizontal lines shown in the $t = 0$ plot of Fig. 6.4. Refer to Fig. 6.5 for further details.

insufficient chemicalreactions, as inferred from the consistent underprediction in filtered temperature and heat-release by the laminar approximation model.

## 6.2.2 Filter-Width Dependence

In the interest of exploring the limits of the combustion models relative to the amount of subgrid information that is lost from filtering, the LES of the TCDF are performed at two other filter-widths, namely $\Delta/l_{Fl} = \{1, 4\}$, using the same three models as Sec. 6.2.1. Based on the turbulent energy spectrum in Fig. 5.5, the three filter-widths $\Delta/l_{Fl} = \{1, 2, 4\}$ will correspond to LES resolutions that are 4, 8, and 16 times, respectively, coarser than
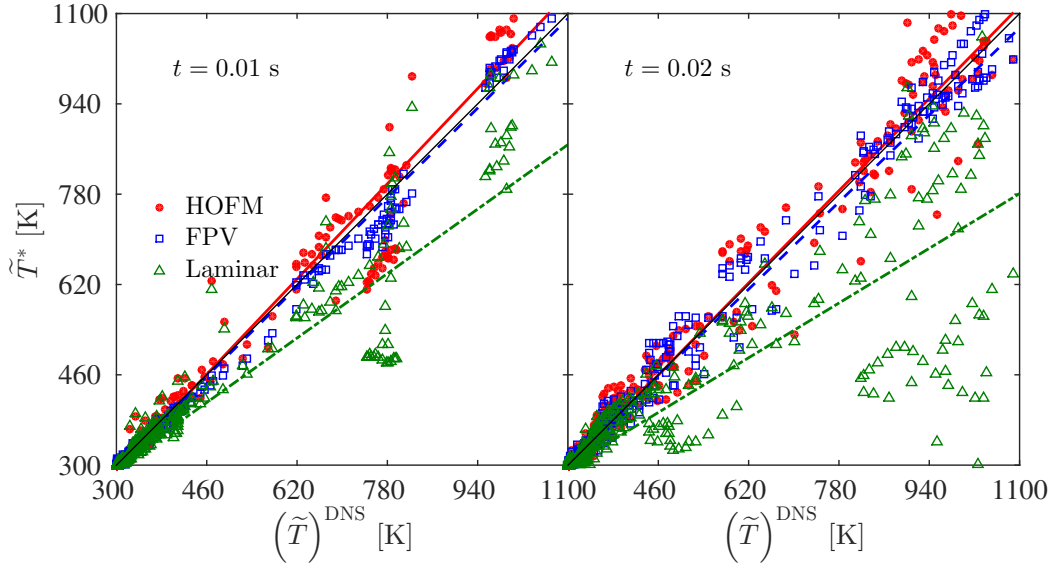
Figure 6.7: Correlation plot for the spanwise-averaged, filtered temperature of HOFM (●, —), FPV (□, --), and laminar (△, ---) model relative to that of DNS at $t = 0.01$ s and $t = 0.02$ s. The thickened lines are the respective linear best-fit of the scatters, while the thin line denotes a perfect correlation. The filter-width is $\Delta/l_{\mathrm{Fl}} = 2$.
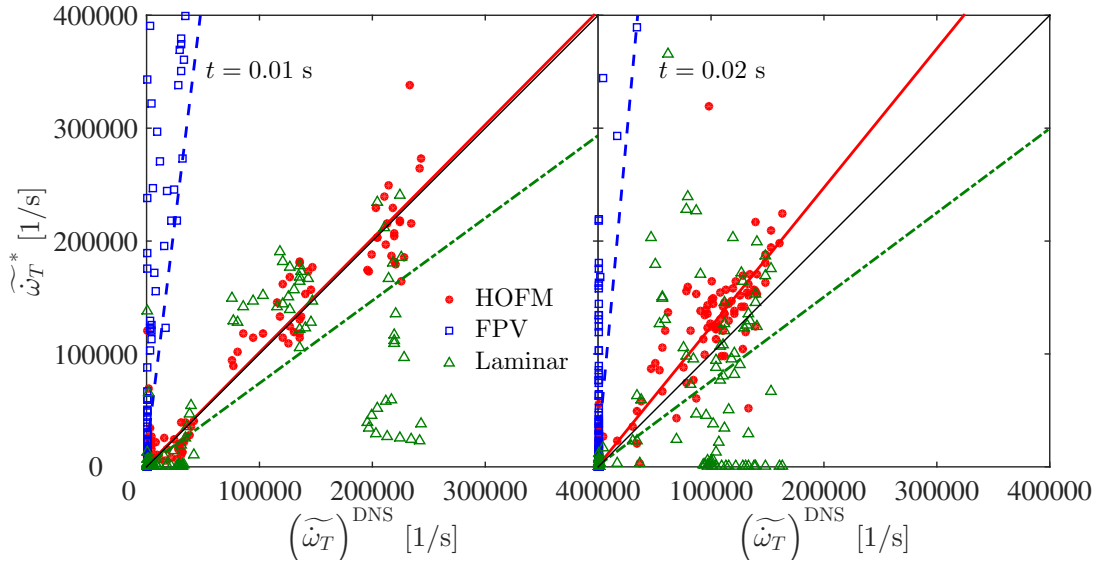


Figure 6.8: Correlation plot for the spanwise-averaged, filtered heat-release rate of HOFM (●, —), FPV (□, --), and laminar (△, ---) model relative to that of DNS at two instants. Refer to Fig. 6.7 for further details.

| Combustion Model | Linear Best-Fit Slope | |
| :---: | :---: | :---: |
| | $t = 0.01$ s | $t = 0.02$ s |
| Mean Filtered Temperature | | |
| HOFM | 1.05 | 1.02 |
| FPV | 0.99 | 0.96 |
| Laminar | 0.71 | 0.61 |
| Mean Filtered Heat-Release Rate | | |
| HOFM | 1.01 | 1.23 |
| FPV | 8.10 | 11.0 |
| Laminar | 0.73 | 0.74 |

Table 6.1: Comparison of the slope of the linear best-fit for the modeled results relative to the reference DNS solutions, which are illustrated in Figs. 6.7–6.8 by the thickened lines.

the reference DNS solutions discussed in Sec. 5.4.2. The study will be performed in terms of the time-varying relative error, which is defined as:

$$\frac{\langle (\cdot)^{\text{DNS}} - (\cdot)^* \,\big|\, t \rangle}{\left| \langle (\cdot)^{\text{DNS}} \,\big|\, t \rangle \right|} \,, \tag{6.1}$$

where $\langle \,|\, t \rangle$ refers to volume-averaging at a given time $t$ and the superscripts $(\,)^{\text{DNS}}$ and $(\,)^*$ denote the reference DNS and modeled results, respectively. Since the numerator of Eq. (6.1) is not an absolute value, a positive error will correspond to an underprediction of the evaluated quantity, and vice versa.

We will first investigate the model performance in representing the non-reacting components of the flow, which is shown in terms of the relative error of the volume-averaged, filtered mixture-fraction with time in Fig. 6.9. Interestingly, despite their differences in the predictions of the Favre-filtered temperature and heat-release rate, the three models demonstrate a comparably small error of approximately 2% in the resolved mixture-fraction field. This observation indicates the consistency in the non-reacting part of the flow-solver, which has been applied equally on all three combustion models. More importantly, this unanimous good agreement of the different combustion models suggests that the flow and chemistry in the current configuration are not strongly coupled, possibly attributed to the thin reaction thickness due to the use of a one-step hydrogen/air chemical mechanism [132]. Consequently, a large part of the domain will then be non-reacting and therefore not affected by the combustion model errors. Note that this observation applies regardless of filter-width, so only one set of the results, in this case that of $\Delta/l_{\text{Fl}} = 2$, is presented.

The relative error of the volume-averaged, filtered temperature with time is shown in Fig. 6.10. From the figure, the flamelet models are shown to predict the filtered tempera-

Figure 6.9: Relative error of the volume-averaged, filtered mixture-fraction of HOFM (●, —), FPV (□, --), and laminar (△, ---) model across the characteristic time period of $\Delta t = 0.02$ s. The filter-width is $\Delta/l_{\mathrm{Fl}} = 2$.

ture profile accurately up to a filter-width of $\Delta/l_{\mathrm{Fl}} = 2$, exhibiting relative errors that vary approximately within the range of $\pm 1\%$. For the cases of the two smaller filter-widths of $\Delta/l_{\mathrm{Fl}} = \{1,\ 2\}$, the laminar model always underpredicts the Favre-filtered temperature with a relative error that increases with time, indicating that the omission of subgrid contributions to the flame is inappropriate for the current configuration. In the largest filter-width case of $\Delta/l_{\mathrm{Fl}} = 4$ in figure 6.10, all the combustion models appear to perform comparably, suggesting that the application of a combustion model is not useful at a very coarse LES level (in this case, an LES grid consisting of only $16 \times 12 \times 8 = 1536$ cells).

Similar to the comparisons in the preceding section, the filtered heat-release results in the $\Delta/l_{\mathrm{Fl}} = \{1,\ 2\}$ cases of Fig. 6.11 show that only HOFM predicts the source term reasonably, with a relative error of ranging approximately from -10% to -30%. Regardless of the filter-widths, the FPV model is always overpredicting the filtered heat-release rate by an approximate order of $\mathcal{O}(10)$. As a result, the FPV model results are presented at a reduced level of 10% in Fig. 6.11 so that the comparison can be performed on a same plot. In contrast to the FPV model, the laminar model is consistently underpredicting the filtered heat-release term, substantiating the aforementioned claim that the SGS contributions to chemical reactions are not negligible. At the coarsest LES level of $\Delta/l_{\mathrm{Fl}} = 4$, the HOFM and laminar model perform similarly, while the FPV model continues to overpredict the filtered heat-release rate.
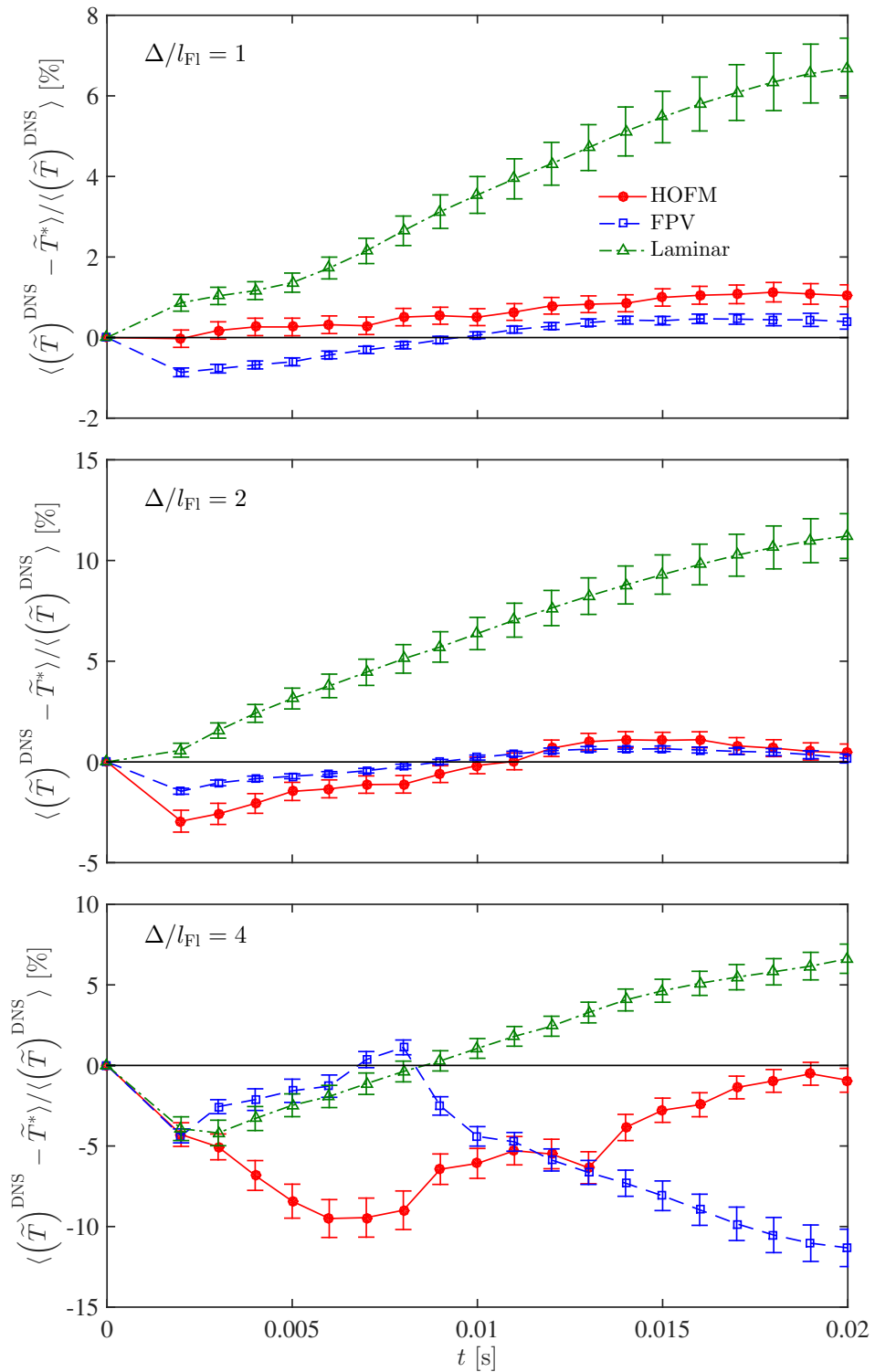
Figure 6.10: Relative error of the volume-averaged, filtered temperature of HOFM (●, —), FPV (□, --), and laminar (△, ---) model across the characteristic time period of $\Delta t = 0.02$ s. The filter-widths are $\Delta/l_{\mathrm{Fl}} = \{1,\ 2,\ 4\}$ from top to bottom, respectively.
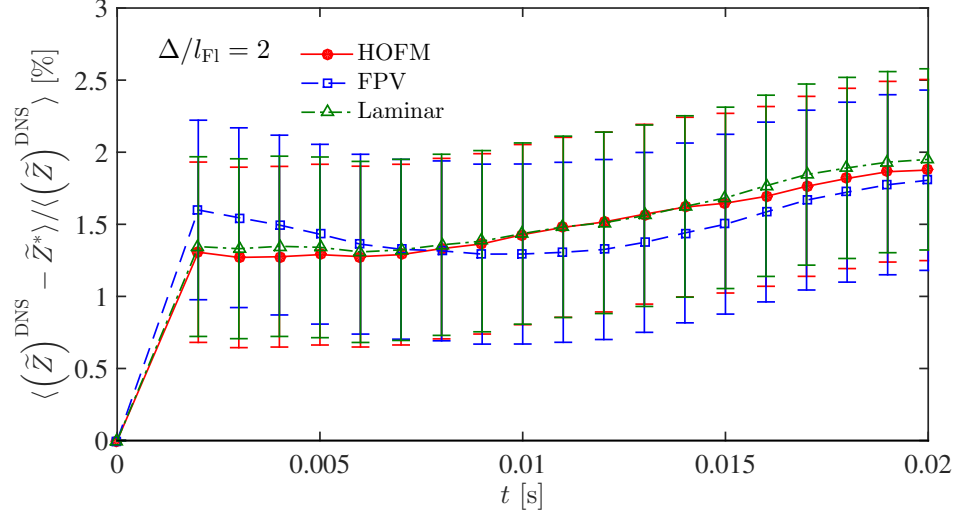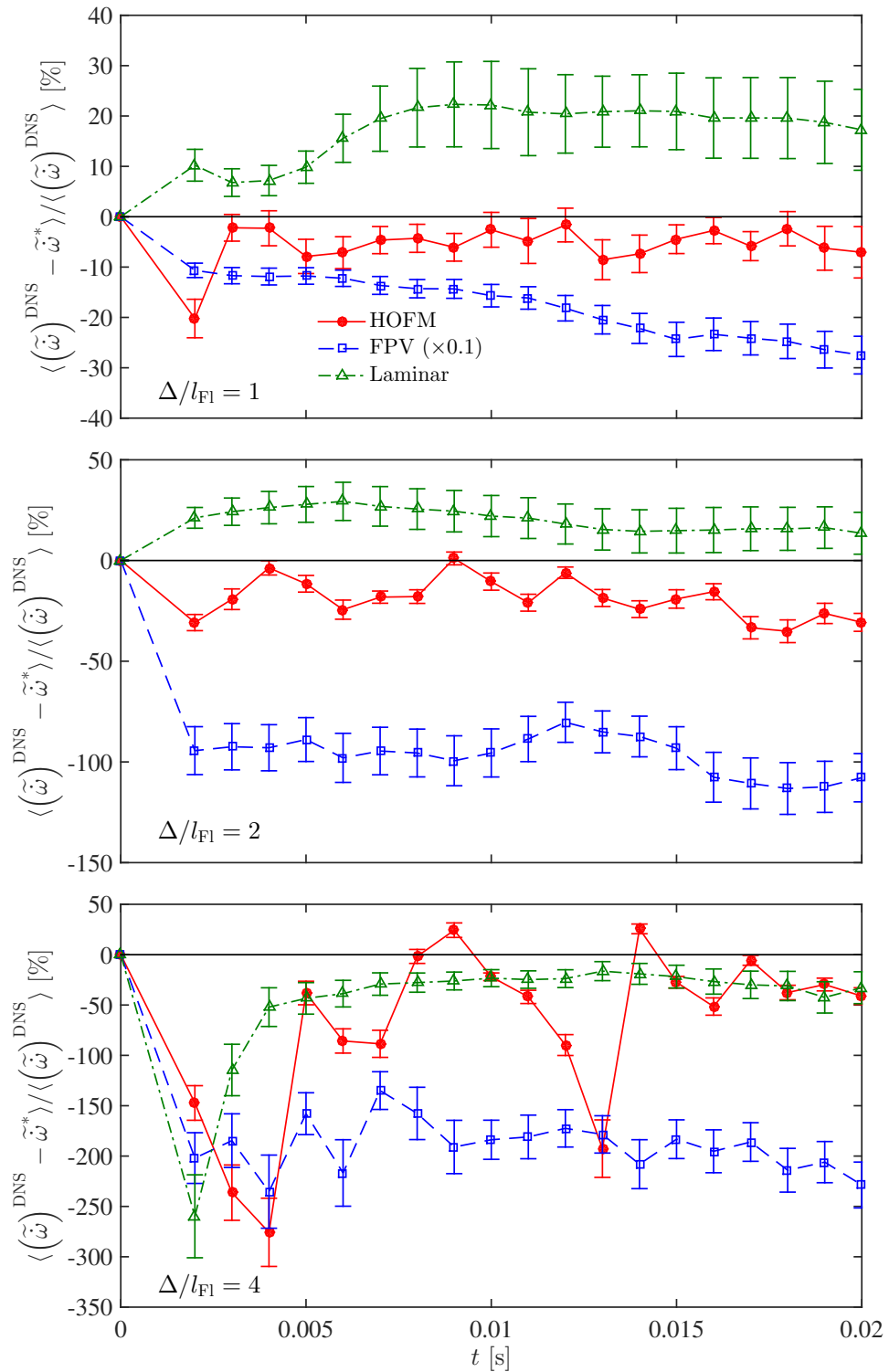
Figure 6.11: Relative error of the volume-averaged, filtered heat-release rate of HOFM (●, —), FPV (□, --), and laminar (△, -·-) model across the characteristic time period of $\Delta t = 0.02$ s. The filter-widths are $\Delta/l_{Fl} = \{1, 2, 4\}$ from top to bottom, respectively.

Given that the steady FPV model accurately predicts the Favre-filtered temperature, its overprediction in the reaction-rate can be explained by referring to the joint PDF of stoichiometric scalar-dissipation rate and temperature, as shown in Fig. 5.7, along with the S-shaped curve that represents the steady flamelet solutions. These steady flamelet solutions collectively constitute the lower-order manifold (cf. Sec.3.3) from which the FPV model obtains the information on the thermochemical states, including the heat-release rate.

In essence, the FPV model will identify a thermochemical states by a *horizontal projection* from a given $(\chi_{Z,\text{st}}, T_{\text{st}})$-pair to the nearest point on the S-shaped curve [35]. For the current configuration, this projection, which is indicated by the arrow in Fig. 5.7, will return thermochemical states that correspond to a higher strained condition and are closer to the flame-quenching point. Since the steady flamelet model asserts a balance between diffusion and reaction in the flamelet space [7, 73], the reaction-rate that is obtained from the higher $\chi_{Z,\text{st}}$ location will be stronger than the reaction-rate at the given lower $\chi_{Z,\text{st}}$ value.

Note that, while only unfiltered quantities are used in the above discussion, the explanations will apply to the filtered case too because the FPV solution lookup, as demonstrated by Fig. 5.7, will occur along the upper stable branch of the S-shaped curve. Consequently, the effects of filtering will only lead to a general decrease in the estimated heat-release rate, but the reaction-rate is still extracted from a significantly overpredicted region.

Using the same reasoning, the observation that the heat-release overprediction by the FPV model does not vanish with increasing resolution, or equivalently smaller filter-widths, is attributed to the same state-space projection towards thermochemical states that correspond to a higher $\chi_{Z,\text{st}}$-value. In fact, this error will be noticeable unless: (i) the vertical deviation from the S-shaped curve is asymptotically small; or (ii) the thermochemical states outside of the S-shaped curve are accounted for, for instance using the unsteady flamelet model [36]. Recognizing this potential source of error in the FPV model, the need for a combustion model to converge to the DNS limit is now apparent. By utilizing the steady flamelet formulation, an implicit assumption is that the unfiltered temperature and species equations (2.14c)–(2.14d) can be described by the steady flamelet formulations. However, as have been demonstrated above, this assumption may not always be valid, thus reinstating the necessity for a more general flamelet model that accommodates the transient and multi-dimensional diffusion effects on a flamelet.

## 6.3 Centerline Flamelet Study

The analysis of the HOFM results in Sec. 6.2 indicates that HOFM is a feasible closure for turbulent combustion simulations. To ensure that this finding is not fortuitous, a further

study on the centerline flamelet that supports HOFM's feasibility is presented in the following. The centerline flamelet is illustrated in by symbols that are colored by temperature in Fig. 6.12 and is extracted from the filtered DNS mixture-fraction field at $t = 0$. For reference, the filter-cell surrounding the spatial origin, unfiltered flame-sheet, and unfiltered flamelets are also shown in Fig. 6.12 by the cube, isosurface, and colored solid lines, respectively. The corresponding temperature profiles of the centerline flamelet and unfiltered flamelets are given by the thickened line and thin lines in Fig. 6.2, respectively.



(a) Global view.



(b) Close-up view.
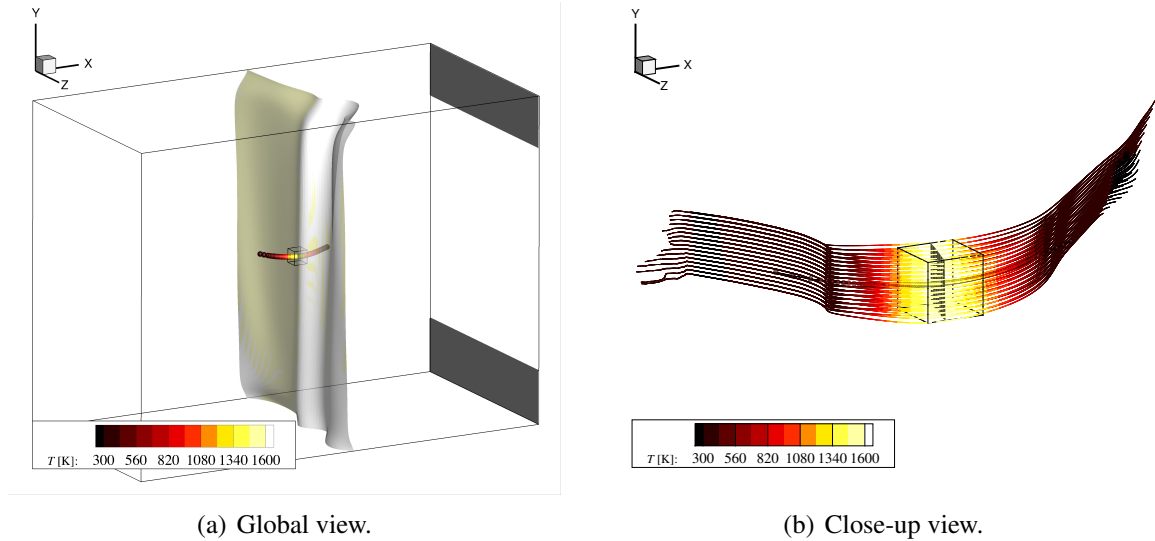
Figure 6.12: Global (left) and close-up (right) view of the centerline flamelet at $t = 0$. In both illustrations, the centerline flamelet is denoted by symbols that are colored by temperature, and is extracted from the filtered mixture-fraction field of $\Delta/l_{\mathrm{Fl}} = 2$ using the spatial origin as its initial tracing location. The flame-sheet in Fig. 6.12(a) is the unfiltered stoichiometric mixture-fraction iso-surface that has been shown in Fig. 5.4, and the solid lines in Fig. 6.12(b), also colored by temperature, represent the unfiltered flamelets that pass through the filter-cell in which the spatial origin is contained. The filter-cell is described by the cube in both subplots.

Following on from the model development in Sec. 5.3, HOFM will essentially use the resolved flamelet information, such as the filtered temperature profile in Fig. 6.2, to reconstruct representative conditional profiles that can be used to compute the representative conditional source-term. As discussed, the reconstruction is performed with the CSE methodology, and the calculation of the conditional source-term is based on the CMC concept. In the current configuration, the conditional temperature, for example, will be given by the conditional mean of the unfiltered temperature distributions in figure 6.2, which is also the average of these flamelet profiles.

Since the unfiltered flamelet profiles are discernibly similar to one another in Fig. 6.2,

the consideration of the CMC formulation in the modeling of the conditional source-term will be appropriate. However, this similarity in the unfiltered profiles may not be relevant to higher turbulent Reynolds number regimes, in which the CMC concept can only be regarded as a leading-order approximation of the true conditional source-term. While higher-order CMC method [135] has been investigated, this approach is not pursued in the current study, but will be considered in future works.

The flamelet budget of $\widetilde{Y}_{H_2O}$ along the centerline flamelet is shown in Fig. 6.13, where the $\widetilde{\mathcal{J}}_k$-notations are defined by:

$$\frac{\partial \widetilde{Y_\alpha}}{\partial \widetilde{\tau}} = \frac{\partial \widetilde{Y_\alpha}}{\partial t} + (\widetilde{u_{G,i}})^{\text{Res}} \frac{\partial \widetilde{Y_\alpha}}{\partial x_i} = \underbrace{\frac{(\widetilde{\chi_Z})^{\text{Res}}}{2} \frac{\partial^2 \widetilde{Y_\alpha}}{\partial \widetilde{Z}^2}}_{\widetilde{\mathcal{J}_1^Z}} + \underbrace{\widetilde{\dot{\omega}_\alpha}}_{\widetilde{\mathcal{J}_2^2}} + \underbrace{\frac{1}{\overline{\rho}} \frac{\partial}{\partial x_i} \left[ \overline{\rho} \widetilde{D} \frac{\partial \widetilde{Y_\alpha^\perp}}{\partial x_i} \right]}_{\widetilde{\mathcal{J}_3^\perp}}$$

$$+ \frac{1}{\overline{\rho}} \frac{\partial}{\partial x_i} \left[ \overline{\rho} \left( -\widetilde{(u_i Y_\alpha)''} + \widetilde{\left( D \frac{\partial Y_\alpha}{\partial x_i} \right)''} \right) \right] . \tag{5.16}$$

In addition, the turbulent flux terms, which formally will be present, are found to be small and hence omitted in this discussion.

From the budget analysis, we can discern that the multi-dimensional diffusion [91], which is introduced in Sec. 4.3 and given by the $\widetilde{\mathcal{J}_3^\perp}$ profile, is indeed smaller than the classical flamelet diffusion ($\widetilde{\mathcal{J}_1^Z}$) and reaction ($\widetilde{\mathcal{J}_2^Z}$) terms, but not to a negligible level. More importantly, the sum of the balance of these flamelet terms, which constitute the $\partial/\partial\widetilde{\tau}$-profile (positive thin solid line), and the resolved Gibson's transport contribution (negative thin solid line) is seen to agree well with the Eulerian time-derivative $\partial/\partial t$-profile, which is denoted in Fig. 6.13 by open symbols. Since the $\partial/\partial t$-term is first calculated in the three-dimensional space, via the sum of the RHS of Eq. (5.9), and then interpolated onto the centerline flamelet, this agreement shows that the Eulerian transport equations are indeed equivalent to their corresponding flamelet equations, provided that all the relevant flamelet contributions are accounted for. Note that this equivalence is general, even though only the results of the centerline flamelet at $t = 0$ have been discussed, because the same observations can be found at other instants and for other flamelets.

Recognizing the equivalence of the Eulerian transport and flamelet equations, the combustion closure incorporated in HOFM can now be explained:

- By utilizing the filtered flamelet profiles, the turbulent flamelet equations (5.16) are implicitly considered by HOFM.
- As demonstrated by the filtered and unfiltered temperature profiles in Fig. 6.2, the fil-
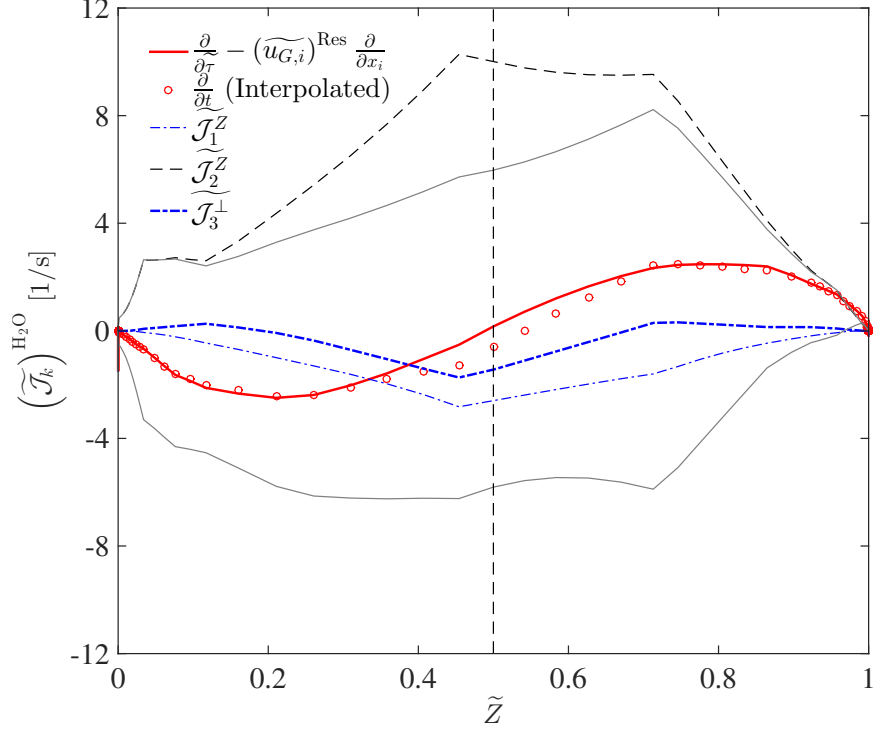
Figure 6.13: Flamelet budgets of $\widetilde{Y}_{H_2O}$ along the evaluated centerline flamelet. The $\widetilde{\mathcal{J}_1^Z}$- (thin ---) and $\widetilde{\mathcal{J}_2^Z}$-terms (thin --) are the flame-aligned terms that provide the classical diffusion-reaction flamelet balance, and the $\widetilde{\mathcal{J}_3^\perp}$-term (thickened ---) is the multidimensional diffusion [91]. The flamelet transient term (positive thin solid line) with the addition of resolved Gibson's transport contribution (negative thin solid line) is denoted by the thickened solid line (—). The Eulerian time-derivative profile (○) is computed in three-dimensional space and interpolated onto the centerline flamelet. The vertical dashed line indicates the stoichiometric mixture-fraction $Z_{st} = 0.5$.

tered flamelet profiles contain SGS information, which can be described by representative conditional distributions. These conditional distributions can be reconstructed using the CSE concepts and, based on CMC, employed to compute the conditional source-term, thus providing HOFM with the necessary combustion closure.

- By advancing the Eulerian transport equations (5.9) in time using filtered reaction-rates that are estimated from the conditional source-term, HOFM is effectively solving the turbulent flamelet equations, but in the Eulerian coordinates instead of the flamelet space.

Based on the good agreement between HOFM results and filtered DNS solutions observed in Sec. (6.2), the HOFM combustion closure is deemed successful for the TCDF configuration, thus providing empirical supports to the claims made above.

# CHAPTER 7

# Conclusions and Directions for Future Work

Forecast of energy outlooks has shown that combustion of fossil fuel will remain as the dominant source of power generation for the years to come, thus necessitating a fast development of combustion devices that are characterized by high combustion efficiency, low pollutant emissions, and flexibility to fuel sources. Large-eddy simulations have shown great potential in meeting this need by complementing physical experiments with accurate predictions of turbulent reacting flows. Non-premixed combustion is a common injection strategy that is employed in aircraft turbine engines and industrial burners because of its efficiency and stability. The flamelet model, which is frequently used for the prediction of non-premixed combustion, was developed by Peters [7, 78], and extended by Pierce & Moin [10] for LES applications. While reacting simulations using the flamelet model have demonstrated outstanding results [10, 84, 136, 137], in some complex configurations the model was found to be underperforming. The objective of this research was to identify the limitations of current flamelet-type combustion models, and develop a flamelet-type model that can overcome these shortcomings.

In order to do so, diagnostic tools were designed in Chap. 4 for the specific purpose of flamelet assumption assessments. These tools were applied in two *a-priori* studies using DNS of a reacting jet-in-crossflow and turbulent lifted jet flame configurations. Results on the applicabiltiy of the flamelet formulation, flame structure in terms of flamelet topologies, and mixture-fraction conditioned data were reported. A flamelet regime diagram that is useful for the direct assessment of the flamelet formulation in numerical simulations was introduced as a potential tool to complement the established techniques of this work. Our analyses showed that the commonly neglected unsteady and higher-order flamelet effects are significant, especially when the reacting flow is transient and characterized by complex turbulent and vortical structures.

The focus of Chap. 5 was on developing the higher-order flamelet model that can account for the unsteady and higher-order flamelet effects. For this, the turbulent flamelet equations, which serve as the counterpart of Peters' laminar flamelet equations in the LES

regime, were derived and form the basis of the proposed model. In order to implement the model, instantaneous filtered flamelets and their quasi one-dimensional thermochemical properties have to be extracted during the flow simulations. The utilization of these flamelet information requires various closures, including the conditional source term estimation method, presumed FDF approach, and spatial-interpolation scheme. By applying this model in a constrained LES of a turbulent counterflow diffusion flame, we have demonstrated that the model concepts are applicable. The constrained LES is a combustion model assessment method that was introduced to eliminate the errors due to the turbulence SGS models by using the solutions of the accompanying DNS, and has the advantage over conventional validation technique in capturing temporal effects in the model implementation.

Finally, in Chap. 6, we applied the proposed model in actual LES of the same turbulent counterflow diffusion flame configuration that was investigated in the constrained LES. The results by the proposed model were shown to perform better than two other combustion closures, namely the steady FPV model and laminar approximation. The successful application of the proposed model was substantiated with a separate numerical investigation of the characteristics of filtered flamelets in the evaluated configuration, showing that the improvement was indeed due to the expected behaviors of the current model.

A higher-order flamelet model was developed and applied, demonstrating the potential to provide a more general description of turbulence-combustion interactions than the classical flamelet models. However, in order to utilize the model in more complex configurations, more work that fully explores the potential and limitations of the current model will be necessary. Some important model extensions and future research topics that are related to this work are discussed below:

- **Chemical reduction:** The proposed model currently requires that all species of the relevant chemical mechanisms be transported. While this approach may be manageable for small mechanisms such as the hydrogen-air system, it will incur prohibitive cost in the consideration of more complex chemical mechanisms such as those describing kerosene (reactions and species on order of $\mathcal{O}(10^3)$ and $\mathcal{O}(10^2)$, respectively). One method to rectify this issue is to employ a reduced reaction mechanism procedure so that the problem size can remain tractable.

- **Fundamental flamelet formulation assessment:** With the flamelet diagnostic tools that were introduced in this work, numerical studies of the flamelet formulation can be conducted more consistently and effectively and should be considered. Insights from these investigations will be useful for the extension of current flamelet-type models, of which one of the lacking areas is in accounting for the compressibility effects in supersonic reacting flows. Interesting academic inquiries, such as when

the flamelet regime is (in)valid, how does turbulence destroy a flamelet, and how flamelets respond when passing a shock, can be also be approached, facilitating the theoretical understanding of combustion in general.

- **Higher-order flamelet terms modeling:** Although the combustion closure incorporated in the current model will, by design, account for the omitted flamelet effects, the approach comes with a relatively high cost. Hence, the investigation in models that can accommodate the omitted flamelet effects will be worthwhile, particularly if the models allow for an *a-priori* description of the higher-order flamelet effects. In this case, the cost-effective lookup technique that is common to the classical flamelet models can be retained, but with increased fidelity from the modeling of higher-order effects.

- **Higher-order conditional moment closure:** One potential shortcoming of the current model is in the utilization of the first-order conditional moment closure, which is valid only when the variations in the conditional profile are moderate. Since this assumption does not apply in highly turbulent flows, the extension to a higher-order conditional moment closure needs to be considered. Alternatively, the current model can be incorporated with the capabilities to identify regions where the first-order conditional moment closure is locally satisfied.

- **PDF modeling:** The current model uses the presumed PDF approach to represent the mixture-fraction subgrid statistics. However, this approach is not guaranteed to deliver in all configurations, for instance in the presence strongly sheared flows. Hence, the importance of more accurate PDF description should be investigated. One possible technique is to employ the DQMOM strategy, which is an Eulerian transported PDF technique that has the potential to transport FDF practically in LES. Another approach that can be considered is the statistically most-likely distribution, which has demonstrated the capability to improve the FDF description of both non-reacting and reacting scalars.

- **Solver optimization:** In the current high-performance computing framework, the usual partitioning of work is through a decomposition of the computational domain. This approach is, however, incompatible with the current model since both flamelets and reaction-zone are local structures, resulting in substantial idle time in the processes that are far away from the reacting region. Therefore, a distribution of workload to these idling processes should be considered so that the overall solver efficiency can be improved. In addition, the current model will benefit from the incorporation of mathematical libraries that are optimized for some of its routine operations, for example spatial-interpolation in a parallel framework and matrix inversion.

# APPENDIX A

# Higher-Order Flamelet Terms

In the derivation of the flamelet equations in Sec. 3.1 and subsequent discussions in earlier sections, the flamelet terms that have complicated expanded forms were kept compact. Incidentally, some of these convoluted terms are also the flamelet components that are conventionally regarded as higher-order effects, and hence neglected. While keeping the complex terms short has been useful for delivering one of the key findings of this research that the commonly omitted flamelet terms may require consideration, the physical interpretations of these effects will require that they be expanded. In this section, all the implicit forms of the flamelet terms in Eqs. (3.6) will be given, constituting the fully expanded form of the laminar flamelet equations. To facilitate the following discussions, the temperature and species flamelet equations in Sec. 3.1 are repeated here:

$$
\frac{\partial T}{\partial \tau} = \frac{\chi_Z}{2} \frac{\partial^2 T}{\partial Z^2} - \sum_\alpha \frac{1}{c_p} h_\alpha \dot{\omega}_\alpha
$$

$$
+ \frac{\chi_Z}{2c_p} \left( \frac{\partial c_p}{\partial Z} + \sum_\alpha \left[ \frac{c_{p,\alpha}}{\mathrm{Le}_\alpha} \left( \frac{\partial Y_\alpha}{\partial Z} + \frac{Y_\alpha}{W} \frac{\partial W}{\partial Z} \right) \right] \right) \frac{\partial T}{\partial Z}
$$

$$
- \frac{\partial Z}{\partial x_i} \left( \frac{\partial v_{C,i}}{\partial Z} + \frac{\partial \rho \varepsilon_i}{\partial Z} \right) \frac{\partial T}{\partial Z} + \mathrm{HOT}_T \ , \tag{3.6a}
$$

$$
\frac{\partial Y_\alpha}{\partial \tau} = \frac{\chi_Z}{2\mathrm{Le}_\alpha} \left( \frac{\partial^2 Y_\alpha}{\partial Z^2} + \frac{Y_\alpha}{W} \frac{\partial^2 W}{\partial Z^2} \right) + \dot{\omega}_\alpha
$$

$$
+ \frac{1 - \mathrm{Le}_\alpha}{4\rho \mathrm{Le}_\alpha} \left( \frac{\partial \rho \chi_Z}{\partial Z} + \frac{\chi_Z}{D_Z} \frac{\partial \rho D_Z}{\partial Z} - \frac{2\rho \chi_Z}{\mathrm{Le}_\alpha (1 - \mathrm{Le}_\alpha)} \frac{\partial \mathrm{Le}_\alpha}{\partial Z} \right) \frac{\partial Y_\alpha}{\partial Z}
$$

$$
+ \frac{1}{4\rho \mathrm{Le}_\alpha} \left( \frac{\partial}{\partial Z} \left[ \frac{\rho \chi_Z Y_\alpha}{W} \right] + \frac{\chi_Z}{D_Z} \frac{\partial}{\partial Z} \left[ \frac{\rho D_Z Y_\alpha}{W} \right] - \frac{2\rho \chi_Z Y_\alpha}{\mathrm{Le}_\alpha W} \frac{\partial \mathrm{Le}_\alpha}{\partial Z} \right) \frac{\partial W}{\partial Z}
$$

$$
- \frac{1}{\rho} \frac{\partial Z}{\partial x_i} \left( \frac{\partial \rho Y_\alpha v_{C,i}}{\partial Z} + \frac{\partial \rho \varepsilon_i}{\partial Z} \frac{\partial Y_\alpha}{\partial Z} \right)
$$

$$
- \frac{1}{\mathrm{Le}_\alpha} \kappa_Z \sqrt{\frac{D_Z \chi_Z}{2}} \left( (\mathrm{Le}_\alpha - 1) \frac{\partial Y_\alpha}{\partial Z} + \frac{Y_\alpha}{W} \frac{\partial W}{\partial Z} \right) + \mathrm{HOT}_\alpha \ . \tag{3.6b}
$$

## A.1 Fully Expanded Laminar Flamelet Equations

We will first focus on the terms common to both the equations, namely the $v_{C,i}$- and $\varepsilon_i$- terms. For the correction velocity term, which is given by:

$$v_{C,i} = \sum_\alpha \frac{Y_\alpha D_\alpha}{X_\alpha} \frac{\partial X_\alpha}{\partial x_i} \ , \tag{2.6}$$

the expanded form will be:

$$
\begin{aligned}
v_{C,i} &= \sum_\alpha D_\alpha \left( \frac{\partial Y_\alpha}{\partial x_i} + \frac{Y_\alpha}{W} \frac{\partial W}{\partial x_i} \right) \\
&= \sum_\alpha \frac{D_Z}{\mathrm{Le}_\alpha} \left( \frac{\partial Y_\alpha}{\partial Z} + \frac{Y_\alpha}{W} \frac{\partial W}{\partial Z} \right) \frac{\partial Z}{\partial x_i} + \sum_\alpha \frac{D_Z}{\mathrm{Le}_\alpha} \left( \frac{\partial Y_\alpha}{\partial Z^\perp} + \frac{Y_\alpha}{W} \frac{\partial W}{\partial Z^\perp} \right) \frac{\partial Z^\perp}{\partial x_i} \ .
\end{aligned} \tag{A.1}
$$

As explained in Sec.5.1, the $Z^\perp$ term in Eq. (A.1) is a local quantity constrained by:

$$\frac{\partial Z}{\partial x_i} \frac{\partial Z^\perp}{\partial x_i} = \|\nabla Z\| \, \|\nabla Z^\perp\| \, \widehat{n}_{Z,i} \widehat{n}_{Z^\perp,i} = 0 \ . \tag{5.5}$$

The diffusion-differential parameter, which is given by:

$$\varepsilon_i = \frac{-1}{\mathcal{Z}_F - \mathcal{Z}_O} \sum_\beta \sum_\alpha \left[ \gamma_\beta \frac{n_{\alpha\beta} W_\beta}{W_\alpha} Y_\alpha v_{\alpha,i} \right] - D_Z \frac{\partial Z}{\partial x_i} \ , \tag{3.4}$$

will be expanded as:

$$
\begin{aligned}
\varepsilon_i &= \frac{1}{\mathcal{Z}_F - \mathcal{Z}_O} \sum_\beta \sum_\alpha \left[ \gamma_\beta \frac{n_{\alpha\beta} W_\beta}{W_\alpha} D_\alpha \left( \frac{\partial Y_\alpha}{\partial x_i} + \frac{Y_\alpha}{W} \frac{\partial W}{\partial x_i} \right) \right] \\
&\quad - (Z_B + \mathcal{Z}_O) \sum_{\alpha'} D'_\alpha \left( \frac{\partial Y'_\alpha}{\partial x_i} + \frac{Y'_\alpha}{W} \frac{\partial W}{\partial x_i} \right) - D_Z \frac{\partial Z}{\partial x_i} \\
&= \frac{1}{\mathcal{Z}_F - \mathcal{Z}_O} \sum_\beta \sum_\alpha \left[ \gamma_\beta \frac{n_{\alpha\beta} W_\beta}{W_\alpha} \frac{D_Z}{\mathrm{Le}_\alpha} \left( \frac{\partial Y_\alpha}{\partial Z} + \frac{Y_\alpha}{W} \frac{\partial W}{\partial Z} \right) \right] \frac{\partial Z}{\partial x_i} \\
&\quad - (Z_B + \mathcal{Z}_O) \sum_{\alpha'} \frac{D_Z}{\mathrm{Le}'_\alpha} \left( \frac{\partial Y'_\alpha}{\partial Z} + \frac{Y'_\alpha}{W} \frac{\partial W}{\partial Z} \right) \frac{\partial Z}{\partial x_i} - D_Z \frac{\partial Z}{\partial x_i} \\
&\quad + \frac{1}{\mathcal{Z}_F - \mathcal{Z}_O} \sum_\beta \sum_\alpha \left[ \gamma_\beta \frac{n_{\alpha\beta} W_\beta}{W_\alpha} \frac{D_Z}{\mathrm{Le}_\alpha} \left( \frac{\partial Y_\alpha}{\partial Z^\perp} + \frac{Y_\alpha}{W} \frac{\partial W}{\partial Z^\perp} \right) \right] \frac{\partial Z^\perp}{\partial x_i} \\
&\quad - (Z_B + \mathcal{Z}_O) \sum_{\alpha'} \frac{D_Z}{\mathrm{Le}'_\alpha} \left( \frac{\partial Y'_\alpha}{\partial Z^\perp} + \frac{Y'_\alpha}{W} \frac{\partial W}{\partial Z^\perp} \right) \frac{\partial Z^\perp}{\partial x_i} \ ,
\end{aligned} \tag{A.2}
$$

where the $Z_B$ term indicates a mixture-fraction according to Bilger's definition [75].

To facilitate the derivations, some useful relations are introduced:

$$\frac{\partial}{\partial Z}\left[\rho D_Z \frac{\partial Z}{\partial x_i}\right]\frac{\partial Z}{\partial x_i} = \frac{1}{4}\left(\frac{\partial \rho \chi_Z}{\partial Z} + \frac{\chi_Z}{D_Z}\frac{\partial \rho D_Z}{\partial Z}\right) , \tag{A.3}$$

$$\kappa_Z = \sqrt{\frac{2D_Z}{\chi_Z}}\frac{\partial}{\partial Z^\perp}\left[\frac{\partial Z^\perp}{\partial x_i}\right]\frac{\partial Z}{\partial x_i} . \tag{A.4}$$

Note that, from Eq. (A.4), the curvature effect of the mixture-fraction field can be interpreted as the change of $Z^\perp$-gradient along the $Z^\perp$-space.

Hence, the derivative of $\varepsilon_i$ is expanded as:

$$\frac{\partial \rho \varepsilon_i}{\partial x_i} = \frac{\partial \rho \varepsilon_i}{\partial Z}\frac{\partial Z}{\partial x_i} + \frac{\partial \rho \varepsilon_i}{\partial Z^\perp}\frac{\partial Z^\perp}{\partial x_i} , \tag{A.5}$$

where

$$\begin{aligned}
\frac{\partial \rho \varepsilon_i}{\partial Z}\frac{\partial Z}{\partial x_i} &= \frac{1}{\mathcal{Z}_F - \mathcal{Z}_O}\sum_\beta\sum_\alpha\left[\gamma_\beta\frac{n_{\alpha\beta}W_\beta}{W_\alpha}\left(\frac{\rho\chi_Z}{2\mathrm{Le}_\alpha}\left(\frac{\partial^2 Y_\alpha}{\partial Z^2} + \frac{Y_\alpha}{W}\frac{\partial^2 W}{\partial Z^2}\right)\right.\right. \\
&\quad + \frac{1}{4\mathrm{Le}_\alpha}\left(\frac{\partial \rho\chi_Z}{\partial Z} + \frac{\chi_Z}{D_Z}\frac{\partial \rho D_Z}{\partial Z} - \frac{2\rho\chi_Z}{\mathrm{Le}_\alpha(1-\mathrm{Le}_\alpha)}\frac{\partial \mathrm{Le}_\alpha}{\partial Z}\right)\frac{\partial Y_\alpha}{\partial Z} \\
&\quad \left.\left. + \frac{1}{4\mathrm{Le}_\alpha}\left(\frac{\partial}{\partial Z}\left[\frac{\rho\chi_Z Y_\alpha}{W}\right] + \frac{\chi_Z}{D_Z}\frac{\partial}{\partial Z}\left[\frac{\rho D_Z Y_\alpha}{W}\right] - \frac{2\rho\chi_Z Y_\alpha}{\mathrm{Le}_\alpha W}\frac{\partial \mathrm{Le}_\alpha}{\partial Z}\right)\frac{\partial W}{\partial Z}\right)\right] \\
&\quad - \frac{\rho\chi_Z}{2}\frac{\partial Z_B}{\partial Z}\sum_{\alpha'}\left[\frac{1}{\mathrm{Le}'_\alpha}\left(\frac{\partial Y_{\alpha'}}{\partial Z} + \frac{Y_{\alpha'}}{W}\frac{\partial W}{\partial Z}\right)\right] \\
&\quad - (Z_B - \mathcal{Z}_O)\sum_{\alpha'}\left[\left(\frac{\rho\chi_Z}{2\mathrm{Le}_{\alpha'}}\left(\frac{\partial^2 Y_{\alpha'}}{\partial Z^2} + \frac{Y_{\alpha'}}{W}\frac{\partial^2 W}{\partial Z^2}\right)\right.\right. \\
&\quad + \frac{1}{4\mathrm{Le}_{\alpha'}}\left(\frac{\partial \rho\chi_Z}{\partial Z} + \frac{\chi_Z}{D_Z}\frac{\partial \rho D_Z}{\partial Z} - \frac{2\rho\chi_Z}{\mathrm{Le}_{\alpha'}(1-\mathrm{Le}_{\alpha'})}\frac{\partial \mathrm{Le}_{\alpha'}}{\partial Z}\right)\frac{\partial Y_{\alpha'}}{\partial Z} \\
&\quad \left.\left. + \frac{1}{4\mathrm{Le}_{\alpha'}}\left(\frac{\partial}{\partial Z}\left[\frac{\rho\chi_Z Y_{\alpha'}}{W}\right] + \frac{\chi_Z}{D_Z}\frac{\partial}{\partial Z}\left[\frac{\rho D_Z Y_{\alpha'}}{W}\right] - \frac{2\rho\chi_Z Y_{\alpha'}}{\mathrm{Le}_{\alpha'}W}\frac{\partial \mathrm{Le}_{\alpha'}}{\partial Z}\right)\frac{\partial W}{\partial Z}\right)\right] \\
&\quad + \frac{1}{4}\left(\frac{\partial \rho\chi_Z}{\partial Z} + \frac{\chi_Z}{D_Z}\frac{\partial \rho D_Z}{\partial Z}\right) , \tag{A.6}
\end{aligned}$$

and

$$\frac{\partial \rho \varepsilon_i}{\partial Z^\perp} \frac{\partial Z^\perp}{\partial x_i} = \frac{1}{\mathcal{Z}_F - \mathcal{Z}_O} \sum_\beta \sum_\alpha \left[ \gamma_\beta \frac{n_{\alpha\beta} W_\beta}{W_\alpha} \left( \frac{\partial}{\partial x_i} \left[ \frac{\rho D_Z}{\mathrm{Le}_\alpha} \frac{\partial Z^\perp}{\partial x_i} \left( \frac{\partial Y_\alpha}{\partial Z^\perp} + \frac{Y_\alpha}{W} \frac{\partial W}{\partial Z^\perp} \right) \right] \right. \right.$$

$$\left. \left. - \frac{\rho}{\mathrm{Le}_\alpha} \kappa_Z \sqrt{\frac{D_Z \chi_Z}{2}} \left( \frac{\partial Y_\alpha}{\partial Z} + \frac{Y_\alpha}{W} \frac{\partial W}{\partial Z} \right) \right) \right]$$

$$- \rho D_Z \left\| \nabla Z^\perp \right\|^2 \frac{\partial Z_B}{\partial Z^\perp} \sum_{\alpha'} \left[ \frac{1}{\mathrm{Le}_{\alpha'}} \left( \frac{\partial Y_{\alpha'}}{\partial Z'} + \frac{Y_{\alpha'}}{W} \frac{\partial W}{\partial Z^\perp} \right) \right]$$

$$+ (Z_B - \mathcal{Z}_O) \sum_{\alpha'} \left[ \frac{\rho}{\mathrm{Le}_{\alpha'}} \kappa_Z \sqrt{\frac{D_Z \chi_Z}{2}} \left( \frac{\partial Y_{\alpha'}}{\partial Z} + \frac{Y_{\alpha'}}{W} \frac{\partial W}{\partial Z} \right) \right]$$

$$- \rho \kappa_Z \sqrt{\frac{\chi_Z D_Z}{2}} \ . \tag{A.7}$$

In Eq. (A.7), the expanded form of the primary species HOT-term has been given as:

$$\mathrm{HOT}_\alpha \sim \mathcal{O} \left( \frac{\partial}{\partial x_i} \left[ \frac{\rho D_Z}{\mathrm{Le}_\alpha} \frac{\partial Z^\perp}{\partial x_i} \left( \frac{\partial Y_\alpha}{\partial Z^\perp} + \frac{Y_\alpha}{W} \frac{\partial W}{\partial Z^\perp} \right) \right] \right) \ . \tag{A.8}$$

From Eq. (A.8), the notion that the higher-order term of the species flamelet equation is a multi-dimensional effect is now clear because the term is given by diffusion in the $Z^\perp$-direction, which is orthogonal to the flamelet space along $Z$. In fact, the differential operators corresponding to the $Y_\alpha$-part of Eq. (A.8) will represent the primary higher-order effects, thus apply also to the temperature flamelet equation:

$$\mathrm{HOT}_T \sim \mathcal{O} \left( \frac{\partial}{\partial x_i} \left[ \rho D_Z \frac{\partial Z^\perp}{\partial x_i} \frac{\partial T}{\partial Z^\perp} \right] \right) \ . \tag{A.9}$$

For temperature, there is a secondary multi-dimensional effect that is derived directly from the temperature gradient:

$$\frac{D_Z}{c_p} \left\| \nabla Z^\perp \right\|^2 \left( \frac{\partial c_p}{\partial Z^\perp} + \sum_\alpha \left[ \frac{c_{p,\alpha} - c_p}{\mathrm{Le}_\alpha} \left( \frac{\partial Y_\alpha}{\partial Z^\perp} + \frac{Y_\alpha}{W} \frac{\partial W}{\partial Z^\perp} \right) \right] \right) \frac{\partial T}{\partial Z^\perp} \ . \tag{A.10}$$

However, this secondary multi-dimensional effect is observed only in the correction velocity part of the species flamelet equation:

$$- \sum_{\alpha'} D_Z \left\| \nabla Z^\perp \right\|^2 \left[ \frac{1}{\mathrm{Le}_{\alpha'}} \left( \frac{\partial Y_{\alpha'}}{\partial Z^\perp} + \frac{Y_{\alpha'}}{W} \frac{\partial W}{\partial Z^\perp} \right) \right] \frac{\partial Y_\alpha}{\partial Z^\perp} \ . \tag{A.11}$$

Putting together all the terms, the fully expanded flamelet equations are given by:

$$
\frac{\partial T}{\partial \tau} = \frac{\chi_Z}{2} \frac{\partial^2 T}{\partial Z^2} - \sum_\alpha \frac{1}{c_p} h_\alpha \dot{\omega}_\alpha + \frac{\chi_Z}{2c_p} \left( \frac{\partial c_p}{\partial Z} + \sum_\alpha \left[ \frac{c_{p,\alpha}}{\mathrm{Le}_\alpha} \left( \frac{\partial Y_\alpha}{\partial Z} + \frac{Y_\alpha}{W} \frac{\partial W}{\partial Z} \right) \right] \right) \frac{\partial T}{\partial Z}
$$

$$
+ \frac{D_Z}{c_p} \left\| \nabla Z^\perp \right\|^2 \left( \frac{\partial c_p}{\partial Z^\perp} + \sum_\alpha \left[ \frac{c_{p,\alpha} - c_p}{\mathrm{Le}_\alpha} \left( \frac{\partial Y_\alpha}{\partial Z^\perp} + \frac{Y_\alpha}{W} \frac{\partial W}{\partial Z^\perp} \right) \right] \right) \frac{\partial T}{\partial Z^\perp}
$$

$$
- \frac{1}{\rho} \left( \frac{\partial \rho \varepsilon_i}{\partial Z} \frac{\partial Z}{\partial x_i} + \frac{\partial \rho \varepsilon_i}{\partial Z^\perp} \frac{\partial Z^\perp}{\partial x_i} \right) \frac{\partial T}{\partial Z} + \frac{\partial}{\partial x_i} \left[ \rho D_Z \frac{\partial Z^\perp}{\partial x_i} \frac{\partial T}{\partial Z^\perp} \right] , \tag{A.12a}
$$

$$
\frac{\partial Y_\alpha}{\partial \tau} = \frac{\chi_Z}{2\mathrm{Le}_\alpha} \left( \frac{\partial^2 Y_\alpha}{\partial Z^2} + \frac{Y_\alpha}{W} \frac{\partial^2 W}{\partial Z^2} \right) + \dot{\omega}_\alpha
$$

$$
+ \frac{1 - \mathrm{Le}_\alpha}{4\rho \mathrm{Le}_\alpha} \left( \frac{\partial \rho \chi_Z}{\partial Z} + \frac{\chi_Z}{D_Z} \frac{\partial \rho D_Z}{\partial Z} - \frac{2\rho \chi_Z}{\mathrm{Le}_\alpha (1 - \mathrm{Le}_\alpha)} \frac{\partial \mathrm{Le}_\alpha}{\partial Z} \right) \frac{\partial Y_\alpha}{\partial Z}
$$

$$
+ \frac{1}{4\rho \mathrm{Le}_\alpha} \left( \frac{\partial}{\partial Z} \left[ \frac{\rho \chi_Z Y_\alpha}{W} \right] + \frac{\chi_Z}{D_Z} \frac{\partial}{\partial Z} \left[ \frac{\rho D_Z Y_\alpha}{W} \right] - \frac{2\rho \chi_Z Y_\alpha}{\mathrm{Le}_\alpha W} \frac{\partial \mathrm{Le}_\alpha}{\partial Z} \right) \frac{\partial W}{\partial Z}
$$

$$
- \sum_{\alpha'} Y_\alpha \left[ \frac{\chi_Z}{2\mathrm{Le}_{\alpha'}} \left( \frac{\partial^2 Y_{\alpha'}}{\partial Z^2} + \frac{Y_{\alpha'}}{W} \frac{\partial^2 W}{\partial Z^2} \right) \right.
$$

$$
+ \frac{1}{4\rho \mathrm{Le}_{\alpha'}} \left( \frac{\partial \rho \chi_Z}{\partial Z} + \frac{\chi_Z}{D_Z} \frac{\partial \rho D_Z}{\partial Z} - \frac{2\rho \chi_Z}{\mathrm{Le}_{\alpha'} (1 - \mathrm{Le}_{\alpha'})} \frac{\partial \mathrm{Le}_{\alpha'}}{\partial Z} \right) \frac{\partial Y_{\alpha'}}{\partial Z}
$$

$$
+ \frac{1}{4\rho \mathrm{Le}_{\alpha'}} \left( \frac{\partial}{\partial Z} \left[ \frac{\rho \chi_Z Y_{\alpha'}}{W} \right] + \frac{\chi_Z}{D_Z} \frac{\partial}{\partial Z} \left[ \frac{\rho D_Z Y_{\alpha'}}{W} \right] - \frac{2\rho \chi_Z Y_{\alpha'}}{\mathrm{Le}_{\alpha'} W} \frac{\partial \mathrm{Le}_{\alpha'}}{\partial Z} \right) \frac{\partial W}{\partial Z}
$$

$$
\left. - \frac{1}{\mathrm{Le}_{\alpha'}} \kappa_Z \sqrt{\frac{D_Z \chi_Z}{2}} \left( \frac{\partial Y_{\alpha'}}{\partial Z} + \frac{Y_{\alpha'}}{W} \frac{\partial W}{\partial Z} \right) \right]
$$

$$
- \frac{Y_\alpha}{\rho} \frac{\partial}{\partial x_i} \left[ \rho D_Z \frac{\partial Z^\perp}{\partial x_i} \sum_{\alpha'} \left[ \mathrm{Le}_{\alpha'} \left( \frac{\partial Y_{\alpha'}}{\partial Z^\perp} + \frac{Y_{\alpha'}}{W} \frac{\partial W}{\partial Z^\perp} \right) \right] \right]
$$

$$
- \sum_{\alpha'} \frac{\chi_Z}{2} \frac{\partial Y_\alpha}{\partial Z} \left[ \left( \frac{\partial Y_{\alpha'}}{\partial Z} + \frac{Y_{\alpha'}}{W} \frac{\partial W}{\partial Z} \right) \right]
$$

$$
- \sum_{\alpha'} D_Z \left\| \nabla Z^\perp \right\|^2 \left[ \frac{1}{\mathrm{Le}_{\alpha'}} \left( \frac{\partial Y_{\alpha'}}{\partial Z^\perp} + \frac{Y_{\alpha'}}{W} \frac{\partial W}{\partial Z^\perp} \right) \right] \frac{\partial Y_\alpha}{\partial Z^\perp}
$$

$$
- \frac{1}{\rho} \left( \frac{\partial \rho \varepsilon_i}{\partial Z} \frac{\partial Z}{\partial x_i} + \frac{\partial \rho \varepsilon_i}{\partial Z^\perp} \frac{\partial Z^\perp}{\partial x_i} \right) \frac{\partial Y_\alpha}{\partial Z}
$$

$$
- \frac{1}{\mathrm{Le}_\alpha} \kappa_Z \sqrt{\frac{D_Z \chi_Z}{2}} \left( (\mathrm{Le}_\alpha - 1) \frac{\partial Y_\alpha}{\partial Z} + \frac{Y_\alpha}{W} \frac{\partial W}{\partial Z} \right)
$$

$$
+ \frac{\partial}{\partial x_i} \left[ \frac{\rho D_Z}{\mathrm{Le}_\alpha} \frac{\partial Z^\perp}{\partial x_i} \left( \frac{\partial Y_\alpha}{\partial Z^\perp} + \frac{Y_\alpha}{W} \frac{\partial W}{\partial Z^\perp} \right) \right] , \tag{A.12b}
$$

where the expansion of the $\varepsilon_i$-fluxes has been given in Eqs. (A.6)–(A.7).

# BIBLIOGRAPHY

[1] "Annual Energy Outlook 2015 with Projections to 2040," 2015, DOE/EIA-0554(2015), available at: www.eia.gov/forecasts/aeo.

[2] "United nations conference on climite change: COP21/CMP11," http://www.cop21.gouv.fr/en/, accessed: 12/24/2015.

[3] Chen, J. H., Choudhary, A., de Supinski, B., DeVries, M., Hawkes, E. R., Klasky, S., Liao, W. K., Ma, K. L., Mellor-Crummey, J., Podhorszki, N., Sankaran, R., Shende, S., and Yoo, C. S., "Terascale direct numerical simulations of turbulent combustion using S3D," *Comput. Sci. Disc.*, Vol. 2, No. 015001, 2009.

[4] Bilger, R. W., "The structure of diffusion flame," *Combust. Sci. Tech.*, Vol. 13, 1976, pp. 155–170.

[5] Sripakagorn, P., Mitarai, S., Kosály, G., and Pitsch, H., "Extinction and reignition in a diffusion flame: a direct numerical simulation study," *J. Fluid Mech.*, Vol. 518, 2004, pp. 231–259.

[6] William, F. A., *Combustion Theory*, Addison-Wesley Publishing Co., Inc., 2nd ed., 1985.

[7] Peters, N., "Laminar Diffusion Flamelet Models in Non-premixed Turbulent Combustion," *Prog. Energy Combust. Sci.*, Vol. 10, No. 3, 1984, pp. 319–339.

[8] Maas, U. and Pope, S. B., "Simplifying chemical kinetics: Intrinsic low-dimensional manifolds in composition space," *Combust. Flame*, Vol. 88, 1992, pp. 239–264.

[9] Peters, N., *Turbulent Combustion*, Cambridge University Press, 2000.

[10] Pierce, C. D. and Moin, P., "Progress-variable approach for large-eddy simulation of non-premixed turbulent combustion," *J. Fluid Mech.*, Vol. 504, 2004, pp. 73–97.

[11] Williams, F. A., "Descriptions of nonpremixed turbulent combustion," *44th AIAA Aerospace Sciences Meeting*, AIAA, Reno, NV, 2006, pp. 2006–1505.

[12] Pitsch, H., Cha, C. M., and Fedotov, S., "Flamelet modelling of non-premixed turbulent combustion with local extinction and re-ignition," *Comb. Theory Modelling*, Vol. 7, 2003, pp. 317–332.

[13] Klimenko, A. Y., "On the relation between the conditional moment closure and unsteady flamelets," *Comb. Theory Modelling*, Vol. 5, 2001, pp. 275–294.

[14] Sagaut, P., *Large Eddy Simulation for Incompressible Flows: An Introduction*, Springer Berlin Heidelberg, 3rd ed., 2006.

[15] Echekki, T. and Mastorakos, E., "Turbulent combustion: Concepts, governing equations and modeling strategies," *Turbulent Combustion Modeling*, edited by T. Echekki and E. Mastorakos, Vol. 95 of *Fluid Mechanics and its Applications*, Springer Netherlands, 1st ed., 2011, pp. 19–39.

[16] Pitsch, H., "Large-eddy simulation of turbulent combustion," *Ann. Rev. Fluid Mech.*, Vol. 38, 2006, pp. 453–482.

[17] Klimenko, A. Y. and Bilger, R. W., "Conditional moment closure for turbulent combustion," *Prog. Energy Combust. Sci.*, Vol. 25, 1999, pp. 595–687.

[18] Kerstein, A., "One-dimensional turbulence: A new approach to high-fidelity subgrid closure of turbulent flow simulations," *Comput. Phys. Commun.*, Vol. 138, No. 1, 2002, pp. 1–16.

[19] Pope, S. B., "PDF methods for turbulent reactive flows," *Prog. Energy Combust. Sci.*, Vol. 11, No. 2, 1985, pp. 119–192.

[20] Echekki, T. and Mastorakos, E., editors, *Turbulent combustion: Concepts, governing equations and modeling strategies*, Vol. 95 of *Fluid Mechanics and its Applications*, Springer Netherlands, 1st ed., 2011.

[21] Klimenko, A. Y., "Multicomponent diffusion of various admixtures in turbulent flow," *Fluid Dynamics*, Vol. 25, No. 3, 1990, pp. 327–334.

[22] Bilger, R. W., "Conditional moment closure for turbulent reacting flow," *Phys. Fluids*, Vol. 5, No. 2, 1993, pp. 436–444.

[23] Kim, S. H. and Pitsch, H., "Conditional filtering method for large-eddy simulation of turbulent nonpremixed combustion," *Phys. Fluids*, Vol. 17, No. 10, 2005, pp. 105103.

[24] Kim, S. H. and Pitsch, H., "Mixing characteristics and structure of a turbulent jet diffusion flame stabilized on a bluff-body," *Phys. Fluids*, Vol. 18, No. 7, 2006, pp. 075103.

[25] Bushe, W. K. and Steiner, H., "Conditional moment closure for large eddy simulation of nonpremixed turbulent reacting flows," *Phys. Fluids*, Vol. 11, No. 7, 1999, pp. 1896–1906.

[26] Labahn, J. W. and Devaud, C. B., "Large eddy simulations (LES) including conditional source-term estimation (CSE) applied to two Delft-jet-in-hot-coflow (DJHC) flames," *Combust. Flame*, Vol. 168, 2015, pp. 68–84.

[27] Bowman, C. T., Hanson, R. K., Davidson, D. F., Gardiner Jr., W. C., Lissianski, V., Smith, G. P., Golden, D. M., Frenklach, M., and Goldenberg, M., "GRI-Mech 2.11," 1995, available at: http://combustion.berkeley.edu/gri-mech/releases.html.

[28] Cook, A. W. and Riley, J. J., "Subgrid-scale modeling for turbulent reacting flows," *Combust. Flame*, Vol. 112, No. 4, 1998, pp. 593–606.

[29] de Bruyn Kops, S. M., Riley, J. J., Kosály, G., and Cook, A. W., "Investigation of modeling for non-premixed turbulent combustion," *Flow, Turb. Combust.*, Vol. 60, No. 1, 1998, pp. 105–122.

[30] Kempf, A., Flemming, F., and Janicka, J., "Investigation of lengthscales, scalar dissipation, and flame orientation in a piloted diffusion flames by LES," *Proc. Combust. Inst.*, Vol. 30, 2005, pp. 557–565.

[31] Stein, O., Kempf, A., and Janicka, J., "LES of the Sydney swirl flame series: An initial investigation of the fluid dynamics," *Combust. Sci. Tech.*, Vol. 179, No. 1–2, 2007, pp. 173–189.

[32] Stein, O. and Kempf, A., "LES of the Sydney swirl flame series: A study of vortex breakdown in isothermal and reacting flows," *Proc. Combust. Inst.*, Vol. 31, 2007, pp. 1755–1763.

[33] Pierce, C. D., *Progress-variable approach for large-eddy simulation of turbulent combustion*, Ph.D. thesis, Stanford University, 2001.

[34] Pitsch, H. and Steiner, H., "Large-eddy simulation of a turbulent piloted methane/air diffusion flame (Sandia flame D)," *Phys. Fluids*, Vol. 12, No. 10, 2000, pp. 2541–2554.

[35] Ihme, M., *Pollutant formation and noise emission in turbulent non-premixed flames*, Ph.D. thesis, Stanford University, 2007.

[36] Ihme, M. and See, Y. C., "Prediction of autoignition in a lifted methane/air flame using an unsteady flamelet/progress variable model," *Combust. Flame*, Vol. 157, 2010, pp. 1850–1862.

[37] Cabra, R., Chen, J.-Y., Dibble, R. W., Karpetis, A. N., and Barlow, R. S., "Lifted methane-air jet flames in a vitiated coflow," *Combust. Flame*, Vol. 143, No. 4, 2005, pp. 491–506.

[38] Kerstein, A. R., "Linear-eddy modeling of turbulent transport. Part 4. Structure of diffusion flames," *Combust. Sci. Tech.*, Vol. 81, No. 1–3, 1992, pp. 75–96.

[39] Kerstein, A. R., "Linear-eddy modeling of turbulent transport. Part 7. Finite-rate chemistry and multistream mixing," *J. Fluid Mech.*, Vol. 240, 1992, pp. 289–313.

[40] Echekki, T., Kerstein, A. R., and Sutherland, J. C., "The one-dimensional-turbulence model," *Turbulent Combustion Modeling*, edited by T. Echekki and E. Mastorakos, Vol. 95 of *Fluid Mechanics and its Applications*, Springer Netherlands, 1st ed., 2011, pp. 249–276.

[41] Cao, S. and Echekki, T., "A low-dimensional stochastic closure model for combustion large-eddy simulation," *J. Turbul.*, Vol. 9, 2008, pp. 1–35.

[42] Pope, S. B., "A Monte Carlo method for the PDF equations of turbulent reactive flow," *Combust. Sci. Tech.*, Vol. 25, 1981, pp. 159–174.

[43] Xu, J. and Pope, S. B., "PDF calculations of turbulent nonpremixed flames with local extinction," *Combust. Flame*, Vol. 123, 2000, pp. 281–307.

[44] Colucci, P. J., Jaberi, F. A., Givi, P., and Pope, S. B., "Filtered density function for large eddy simulation of turbulent reacting flows," *Phys. Fluids*, Vol. 10, No. 2, 1998, pp. 499–515.

[45] Raman, V., Pitsch, H., and Fox, R. O., "Hybrid large-eddy simulation/Lagrangian filtered-density-function approach for simulating turbulent combustion," *Combust. Flame*, Vol. 143, 2005, pp. 56–78.

[46] Raman, V. and Pitsch, H., "A consistent LES/filtered-density function formulation for the simulation of turbulent flames with detailed chemistry," *Proc. Combust. Inst.*, Vol. 31, 2007, pp. 1711–1719.

[47] Coffee, T. P. and Heimerl, J. M., "Transport algorithms for premixed, laminar steady-state flames," *Combust. Flame*, Vol. 43, No. 3, 1981, pp. 273–289.

[48] Ihme, M. and Pitsch, H., "Effects of heat release on turbulent jet flows," *5th International Conference on Turbulence and Shear Flow Phenomena*, Munich, Germany, 2011.

[49] Bergmann, V., Meier, W., Wolff, D., and Stricker, W., "Application of spontaneous Raman and Rayleigh scattering and 2D LIF for the characterization of a turbulent $CH_4/H_2/N_2$ jet diffusion flame," *Appl. Phys. B*, Vol. 66, No. 4, 1998, pp. 489–502.

[50] Meier, W., Barlow, R. S., Chen, Y. L., and Chen, J.-Y., "Raman/Rayleigh/LIF measurements in a turbulent $CH_4/H_2/N_2$ jet diffusion flame," *Combust. Flame*, Vol. 123, No. 3, 2000, pp. 326–343.

[51] Yeung, P. K. and Pope, S. B., "Differential diffusion of passive scalars in isotropic turbulence," *Phys. Fluids*, Vol. 5, No. 10, 1993, pp. 2467–2478.

[52] Nilsen, V. and Kosály, G., "Differential diffusion in turbulent reacting flows," *Combust. Flame*, Vol. 117, No. 3, 1999, pp. 493–513.

[53] Pitsch, H., "Unsteady Flamelet Modeling of Differential Diffusion in Turbulent Jet Diffusion Flames," *Combust. Flame*, Vol. 123, 2000, pp. 358–374.

[54] Shapiro, A. H., *The Dynamics and Thermodynamics of Compressible Fluid Flow*, The Ronald Press Co., 1953.

[55] Ingenito, A. and Bruno, C., "Physics and regimes of supersonic combustion," *AIAA J.*, Vol. 48, No. 3, 2010, pp. 515–525.

[56] Saghafian, A., Shunn, L., Philips, D. A., and Ham, F., "Large eddy simulations of the HIFiRE scramjet using a compressible flamelet/progress variable approach," *Proc. Combust. Inst.*, Vol. 35, 2015, pp. 2163–2172.

[57] Onsager, L., "Reciprocal relations in irreversible processes," *Phys. Rev.*, Vol. 38, 1931, pp. 405–426.

[58] White, F. M., *Viscous Fluid Flow*, McGraw-Hill, 3rd ed., 2006.

[59] Stokes, G. G., "On the theories of the internal friction of fluids in motion, and of the equilibrium and motion of the elastic solids," *Trans. Cambr. Phil. Soc.*, Vol. 8, 1845, pp. 287–319.

[60] Poinsot, T., Veynante, D., and Candel, S., "Quenching processes and premixed turbulent combustion diagrams," *J. Fluid Mech.*, Vol. 228, 1991, pp. 561–605.

[61] Coelho, P. J., "Numerical simulation of the interaction between turbulence and radiation in reactive flows," *Prog. Energy Combust. Sci.*, Vol. 33, 2007, pp. 311–383.

[62] Poinsot, T. and Veynante, D., *Theoretical and Numerical Combustion*, Authors, 3rd ed., 2012.

[63] Ghosal, S., "Mathematical and physical constraints on large-eddy simulation of turbulence," *AIAA J.*, Vol. 37, No. 4, 1999, pp. 425–433.

[64] Germano, M., Piomelli, U., Moin, P., and Cabot, W. H., "A dynamic subgrid-scale eddy viscosity model," *Phys. Fluids*, Vol. 3, No. 7, 1991, pp. 1760–1765.

[65] Lilly, D. K., "A proposed modification of Germano subgrid-scale closure method," *Phys. Fluids*, Vol. 4, No. 3, 1992, pp. 633–635.

[66] Meneveau, C., Lund, T. S., and Cabot, W. H., "A Lagrangian dynamic subgrid-scale model of turbulence," *J. Fluid Mech.*, Vol. 319, 1996, pp. 353–385.

[67] Smagorinsky, J., "General circulation experiments with the primitive equations: 1. The basic experiment," *Mon. Weather Rev.*, Vol. 91, 1963, pp. 99–164.

[68] Deardorff, J. W., "A numerical study of three-dimensional turbulent channel flow at large Reynolds numbers," *J. Fluid Mech.*, Vol. 41, No. 2, 1970, pp. 453–480.

[69] Mason, P. J. and Callen, N. S., "On the magnitude of the subgrid-scale eddy coefficient in large-eddy simulations of turbulent channel flow," *J. Fluid Mech.*, Vol. 162, 1986, pp. 439–462.

[70] Piomelli, U., Moin, P., and Ferziger, J. H., "Model consistency in large eddy simulation of turbulent channel flows," *Phys. Fluids*, Vol. 31, No. 7, 1988, pp. 1884–1891.

[71] Pope, S. B., "Ten questions concerning the large-eddy simulation of turbulent flows," *New J. Phys.*, Vol. 6, No. 35, 2004.

[72] Williams, F. A., "Recent advances in theoretical descriptions of turbulent diffusion flames," *Turbulent Mixing in Nonreactive and Reactive Flows*, edited by S. N. B. Murthy, Plenum Press, 1975, pp. 189–208.

[73] Peters, N., "Local quenching due to flame stretch and non-premixed turbulent combustion," *Combust. Sci. Tech.*, Vol. 30, 1983, pp. 1–17.

[74] Cuenot, B., "The flamelet model for non-premixed combustion," *Turbulent Combustion Modeling*, edited by T. Echekki and E. Mastorakos, Vol. 95 of *Fluid Mechanics and its Applications*, Springer Netherlands, 1st ed., 2011, pp. 43–61.

[75] Bilger, R. W., Stårner, S. H., and Kee, R. J., "On Reduced Mechanisms for Methane-Air Combustion in Nonpremixed Flames," *Combust. Flame*, Vol. 80, 1990, pp. 135–149.

[76] Sutherland, J. C., Smith, P. J., and Chen, J. H., "Quantification of differential diffusion in nonpremixed systems," *Comb. Theory Modelling*, Vol. 9, No. 2, 2005, pp. 365–383.

[77] Pitsch, H. and Peters, N., "A Consistent Flamelet Formulation for Non-Premixed Combustion Considering Differential Diffusion Effects," *Combust. Flame*, Vol. 114, 1998, pp. 26–40.

[78] Peters, N., "Laminar Flamelet Concept in Turbulent Combustion," *Proc. Combust. Inst.*, Vol. 21, No. 1, 1986, pp. 1231–1250.

[79] Pitsch, H., Chen, M., and Peters, N., "Unsteady Flamelet Modeling of Turbulent Hydrogen/Air Diffusion Flames," *Proc. Combust. Inst.*, Vol. 27, 1998, pp. 1057–1064.

[80] Haworth, D., Drake, M., Pope, S., and Blint, R., "The importance of time-dependent flame structure in stretched laminar flamelet models for turbulent jet diffusion flames," *Proc. Combust. Inst.*, Vol. 22, 1988, pp. 589–597.

[81] Pitsch, H., Barths, H., and Peters, N., "Three-dimensional modelling of $NO_x$ and soot formation in DI-diesel engines using detailed chemistry based on the interactive flamelet approach," *SAE Paper*, Vol. 962057, 1996, pp. 103–117.

[82] Barths, H., Hasse, C., Bikas, G., and Peters, N., "Simulation of combustion in direct injection diesel engines using a Eulerian particle flamelet model," *Proc. Combust. Inst.*, Vol. 28, 2000, pp. 1161–1168.

[83] Cuenot, B., Egolfopoulos, F., and Poinsot, T., "An unsteady laminar flamelet model for non-premixed combustion," *Comb. Theory Modelling*, Vol. 4, 2000, pp. 77–97.

[84] See, Y. C., *Analysis of hydrodynamic instabilities and combustion dynamics in turbulent reacting flows*, Ph.D. thesis, University of Michigan, 2014.

[85] Ihme, M., Cha, C. M., and Pitsch, H., "Prediction of local extinction and re-ignition effects in non-premixed turbulent combustion using a flamelet/progress variable approach," *Proc. Combust. Inst.*, Vol. 30, 2005, pp. 793–800.

[86] Ihme, M., Shunn, L., and Zhang, J., "Regularization of reaction progress variable for application to flamelet-based combustion models," *J. Comp. Phys.*, Vol. 231, 2012, pp. 7715–7721.

[87] Pope, S. B., "Computations of turbulent combustion: Progress and challenges," *Proc. Combust. Inst.*, Vol. 23, 1990, pp. 591–612.

[88] Coclite, A., Pascazio, G., De Palma, P., Cutrone, L., and Ihme, M., "An SMLD joint PDF model for turbulent non-premixed combustion using the flamelet progress-variable approach," *Flow, Turb. Combust.*, Vol. 95, No. 1, 2015, pp. 97–119.

[89] Pope, S. B., "Probability distributions of scalars in turbulent shear flow," *Turbulent Shear Flows*, Vol. 2, 1980, pp. 7–16.

[90] Chan, W. L., Kolla, H., Chen, J. H., and Ihme, M., "Assessment of model assumptions and budget terms of the unsteady flamelet equations for a turbulent reacting jet-in-cross-flow," *Combust. Flame*, Vol. 161, No. 10, 2014, pp. 2601–2613.

[91] Scholtissek, A., Chan, W. L., Xu, H., Hunger, F., Kolla, H., Chen, J. H., Ihme, M., and Hasse, C., "A multi-scale asymptotic scaling and regime analysis of flamelet equations including tangential diffusion effects for laminar and turbulent flames," *Combust. Flame*, Vol. 162, No. 4, 2015, pp. 1507–1529.

[92] Pratte, B. D. and Baines, W. D., "Profiles of the round turbulent jet in a cross-flow," *J. Hydraul. Eng.*, Vol. 92, 1967, pp. 53–64.

[93] Wyngaard, J. C. and Coté, O. R., "The budgets of turbulent kinetic energy and temperature variance in the atmospheric surface layer," *J. Atmos. Sci.*, Vol. 28, 1970, pp. 190–201.

[94] Grout, R. W., Gruber, A., Yoo, C. S., and Chen, J. H., "Direct numerical simulation of flame stabilization downstream of a transverse fuel jet in cross-flow," *Proc. Combust. Inst.*, Vol. 33, 2011, pp. 1629–1637.

[95] Grout, R. W., Gruber, A., Kolla, H., Bremer, P.-T., Bennett, J. C., Gyulassy, A., and Chen, J. H., "A direct numerical simulation study of turbulence and flame structure in transverse jets analysed in jet-trajectory based coordinates," *J. Fluid Mech.*, Vol. 706, 2012, pp. 351–383.

[96] Yoo, C. S., Sankaran, R., and Chen, J. H., "Three-dimensional direct numerical simulation of a turbulent lifted hydrogen jet flame in heated coflow: Flame stabilization and structure," *J. Fluid Mech.*, Vol. 640, 2009, pp. 453–481.

[97] Lu, T. F., Yoo, C. S., Chen, J. H., and Law, C. K., "Three-dimensional direct numerical simulation of a turbulent lifted hydrogen jet flame in heated coflow: A chemical explosive mode analysis," *J. Fluid Mech.*, Vol. 652, 2010, pp. 45–64.

[98] Fric, T. F. and Roshko, A., "Vortical structure in the wake of a transverse jet," *J. Fluid Mech.*, Vol. 279, 1994, pp. 1–47.

[99] Mahesh, K., "The interaction of jets with crossflow," *Ann. Rev. Fluid Mech.*, Vol. 45, 2013, pp. 379–407.

[100] Kolla, H., Grout, R. W., Gruber, A., and Chen, J. H., "Effect of injection angle on stabilization of a reacting turbulent hydrogen jet in cross-flow," *7th US National Technical Meeting of the Combustion Institute*, The Combustion Institute, Atlanta, GA, 2011.

[101] Steinberg, A. M., Sadanandan, R., Dem, C., Kutne, P., and Meier, W., "Structure and stabilization of hydrogen jet flames in cross-flows," *Proc. Combust. Inst.*, Vol. 34, 2013, pp. 1499–1507.

[102] Li, J., Zhao, Z., Kazakov, A., Chaos, M., Dryer, F. L., and Scire, Jr., J., "An Updated Comprehensive Kinetic Model of Hydrogen Combustion," *Int. J. Chem. Kinet.*, Vol. 36, No. 10, 2004, pp. 566–575.

[103] Kothnur, P. S. and Clemens, N. T., "Effects of unsteady strain rate on scalar dissipation structures in turbulent planar jets," *Phys. Fluids*, Vol. 17, No. 125104, 2005.

[104] Peters, N. and Williams, F. A., "Liftoff characteristics of turbulent jet diffusion flames," *AIAA J.*, Vol. 21, 1983, pp. 423–429.

[105] Kalghatgi, G. T., "Lift-off heights and visible lengths of vertical turbulent jet diffusion flames in still air," *Combust. Sci. Tech.*, Vol. 41, 1984, pp. 17–29.

[106] Buckmaster, J., "Edge flames," *Prog. Energy Combust. Sci.*, Vol. 28, 2002, pp. 435–475.

[107] Joedicke, A., Peters, N., and Mansour, M., "The stabilization mechanism and structure of turbulent hydrocarbon lifted flames," *Proc. Combust. Inst.*, Vol. 30, 2005, pp. 901–909.

[108] Su, L. K., Sun, O. S., and Mungal, M. G., "Experimental investigation of stabilization mechanisms in turbulent, lifted jet diffusion flames," *Combust. Flame*, Vol. 144, 2006, pp. 494–512.

[109] Gordon, R. L., Masri, A. R., and Mastorakos, E., "Simultaneous Rayleigh temperature, OH- and $CH_2O$-LIF imaging of methane jets in a vitiated coflow," *Combust. Flame*, Vol. 155, 2008, pp. 181–195.

[110] Tsuji, H., "Counterflow diffusion flames," *Prog. Energy Combust. Sci.*, Vol. 8, 1982, pp. 93–119.

[111] Seshadri, K. and Peters, N., "Asymptotic structure and extinction of methane-air diffusion flames," *Combust. Flame*, Vol. 73, 1988, pp. 23–44.

[112] Wang, L. and Peters, N., "The length-scale distribution function of the distance between extremal points in passive scalar turbulence," *J. Fluid Mech.*, Vol. 554, 2006, pp. 457–475.

[113] Nguyen, P., Vervisch, L., Subramanian, V., and Domingo, P., "Multidimensional flamelet-generated manifolds for partially premixed combustion," *Combust. Flame*, Vol. 157, 2010, pp. 43–61.

[114] Gibson, C. H., "Fine structure of scalar fields mixed by turbulence. I. Zero-gradient points and minimal gradient surfaces," *Phys. Fluids*, Vol. 11, 1968, pp. 2305–2315.

[115] Hansen, P. C., "Numerical tools for analysis and solution of Fredholm integral equations of the first kind," *Inverse Probl.*, Vol. 8, 1992, pp. 849–862.

[116] Tikhonov, A. N. and Arsenin, V. I., *Solutions of ill-posed problems*, V. H. Winston and Son, Inc., 1977.

[117] Grout, R. W., Bushe, W. K., and Blair, C., "Predicting the ignition delay of turbulent methane jets using Conditional Source-term Estimation," *Comb. Theory Modelling*, Vol. 11, No. 6, 2007, pp. 1009–1028.

[118] Labahn, J. W., Dovizio, D., and Devaud, C. B., "Numerical simulation of the Delft-Jet-in-Hot-Coflow (DJHC) flame using Conditional Source-term Estimation," *Proc. Combust. Inst.*, Vol. 35, 2015, pp. 3547–3555.

[119] Cook, A. W. and Riley, J. J., "A subgrid model for equilibrium chemistry in turbulent flows," *Phys. Fluids*, Vol. 6, No. 8, 1994, pp. 2868–2870.

[120] Jiménez, J., Linañ, A., Rogers, M. M., and Higuera, F. J., "A priori testing of subgrid modles for chemically reacting non-premixed turbulent shear flows," *J. Fluid Mech.*, Vol. 349, 1997, pp. 149–171.

[121] Wall, C., Boersma, B. J., and Moin, P., "An evaluation of the assumed beta probability density function subgrid-scale model for large eddy simulation of nonpremixed, turbulent combustion with heat release," *Phys. Fluids*, Vol. 12, No. 10, 2000, pp. 2522–2529.

[122] Tong, C., "Measurements of conserved scalar filtered density function in a turbulent jet," *Phys. Fluids*, Vol. 13, No. 10, 2001, pp. 2923–2937.

[123] Fox, R. O., *Computational Models for Turbulent Reacting Flows*, Cambridge University Press, 2003.

[124] Koo, H., Donde, P., and Raman, V., "A quadrature-based LES/transported probability density function approach for modeling supersonic combustion," *Proc. Combust. Inst.*, Vol. 33, 2011, pp. 2203–2210.

[125] Burrough, P. A. and McDonnell, R. A., *Principles of Geographical Information Systems*, Oxford University Press, 1998.

[126] Matheron, G., "Principles of geostatistics," *Econ. Geogr.*, Vol. 58, No. 8, 1963, pp. 1246–1266.

[127] Lu, G. Y. and Wong, D. W., "An adaptive inverse-distance weighting spatial interpolation technique," *Comput. Geosci.*, Vol. 34, 2008, pp. 1044–1055.

[128] Tobler, W., "A computer movie simulating urban growth in the Detroit region," *Econ. Geogr.*, Vol. 46, No. 2, 1970, pp. 234–240.

[129] Coppola, G., Coriton, B., and Gomez, A., "Highly turbulent counterflow flames: A laboratory scale benchmark for practical systems," *Combust. Flame*, Vol. 156, 2009, pp. 1834–1843.

[130] Coriton, B., Frank, J. H., Hsu, A. G., Smooke, M. D., and Gomez, A., "Effect of quenching of the oxidation layer in highly turbulent counterflow premixed flames," *Proc. Combust. Inst.*, Vol. 33, 2011, pp. 1647–1654.

[131] Coriton, B., Frank, J. H., and Gomez, A., "Effects of strain rate, turbulence, reactant stoichiometry and heat losses on the interaction of turbulent premixed flames with stoichiometric counterflowing combustion products," *Combust. Flame*, Vol. 160, 2013, pp. 2442–2456.

[132] Marinov, N. M., Westbrook, C. K., and Pitz, W. J., "Detailed and global chemical kinetics model for hydrogen," *8th International Symposium on Transport Properties*, San Francisco, CA, 1995.

[133] Jeong, J. and Hussain, F., "On the identification of a vortex," *J. Fluid Mech.*, Vol. 285, 1995, pp. 69–94.

[134] Dahm, W. J. A. and Buch, K. A., "Lognormality of the scalar dissipation pdf in turbulent flows," *Phys. Fluids A*, Vol. 1, No. 7, 1989, pp. 1290–1293.

[135] Kronenburg, A., Bilger, R. W., and Kent, J. H., "Second-order conditional moment closure for turbulent jet diffusion flames," *Proc. Combust. Inst.*, Vol. 27, 1998, pp. 1097–1104.

[136] Ihme, M. and Pitsch, H., "Modeling of radiation and nitric oxide formation in turbulent nonpremixed flames using a flamelet/progress variable formulation," *Phys. Fluids*, Vol. 20, No. 5, 2008, pp. 20.

[137] Raman, V. and Pitsch, H., "Large-eddy simulation of a bluff-body-stabilized nonpremixed flame using a recursive filter-refinement procedure," *Combust. Flame*, Vol. 142, 2005, pp. 329–347.